

April 2023

Multiple Access Techniques Enabling Diverse Wireless Services

Mehmet Mert Şahin
University of South Florida

Follow this and additional works at: <https://digitalcommons.usf.edu/etd>



Part of the [Electrical and Computer Engineering Commons](#)

Scholar Commons Citation

Şahin, Mehmet Mert, "Multiple Access Techniques Enabling Diverse Wireless Services" (2023). *USF Tampa Graduate Theses and Dissertations*.
<https://digitalcommons.usf.edu/etd/9924>

This Dissertation is brought to you for free and open access by the USF Graduate Theses and Dissertations at Digital Commons @ University of South Florida. It has been accepted for inclusion in USF Tampa Graduate Theses and Dissertations by an authorized administrator of Digital Commons @ University of South Florida. For more information, please contact digitalcommons@usf.edu.

Multiple Access Techniques Enabling Diverse Wireless Services

by

Mehmet Mert Şahin

A dissertation submitted in partial fulfillment
of the requirements for the degree of
Doctor of Philosophy
Department of Electrical Engineering
College of Engineering
University of South Florida

Co-Major Professor: Hüseyin Arslan, Ph.D.
Co-Major Professor: Gökhan Mumcu, Ph.D.
Kwang-Cheng Chen, Ph.D.
Ismail Uysal, Ph.D.
Dmitry B. Goldgof, Ph.D.
Javad Abdoli, Ph.D.

Date of Approval:
April 4, 2023

Keywords: 6G, non-orthogonal multiple access, interference, rate-splitting

Copyright © 2023, Mehmet Mert Şahin

Dedication

To my family.

Acknowledgments

First of all, I sincerely appreciate my advisor, Dr. Hüseyin Arslan, for providing me the opportunity and the means to achieve this level, and having the patience to allow me to develop my skills at the time when my progress slowed down. Since the beginning, I saw him as a role model. As time goes on, I realized that I've made the right decision to be a student of him. He always find a way to approach me constructively. His guidance, encouragement, efforts and advice made this dissertation possible. I am really grateful for his exceptional endeavor in cultivating my professional skills. It is an honor for me to be a student of him.

Next, special thanks to my other advisor Dr. Gökhan Mumcu for academic and financial supports. It is always valuable to take his guides and feel his supports at every time. It was always informative and enjoyable to talk to him about every aspects of the life.

I would also like to thank Dr. Kwang-Cheng Chen, Dr. Bruno Clerckx, Dr. Ertugrul Basar, Dr. Onur Dizdar, Dr. Young-Han Nam, Logeshwaran Vijayan, Dr. Ismail Uysal, Dr. Dmitry Goldgof, and Dr. Javad Abdoli for their support and guidance throughout my graduate studies. Their broad experience enriched my background significantly, and invaluable encouragement has led to completion of this dissertation. Without a doubt, I am fortunate to meet and collaborate with them.

It has been a great privilege to be a member of the Wireless Communications and Signal Processing (WCSP) group. I owe a lot to my colleagues and dear friends in this group. I would like to thank Dr. Murat Karabacak, Dr. Ali Fatih Demir, Dr. Berker Peköz, Dr. Mohammed Hafez, Thomas Ranstrom, Mehmet Yazgan and Sinasi Cetinkaya for informative discussion and their guidance. They always made me feel comfortable and confident throughout this long journey. Moreover, I would like to thank my colleagues, Dr. Furqan Ahmed, Dr. Ahmet Yazar, Dr. Seda Tusha, Ebubekir Memisoglu, Abuu Bakari Kihero,

Halise Turkmen, Musab Alayusra, Armed Tusha, Salah Eddine Zegrar, Sohaib Solaija, Enes Duranay, Bilal Janjua, Ahmed Naeem, Saira Rafique, Ahmet Sacit Sumer from Communications, Signal Processing, and Networking Center at Istanbul Medipol University for their collaborations and technical discussions. Special thanks to Emre Arslan, Ilter Erol Gurol, and Ali Tugberk Dogukan for their collaborations.

Special thanks to my officemates, Dr. Merve Kacar, Anil Imren and Furkan Mumcu, Santhi Swaroop Madeti, Vishvajitsinh Kosamiya, Ruohe Liu, for the enjoyable time and fruitful discussions. Last but not least, I am very honored to know Omar Jibreel and Ugur Guneroglu who convert the town Tampa to a friendly place.

Warm greetings to all my friends, from my childhood up to Bilkent University where I got my B.S. degree, but Mert Bozkurt, Muratcan Balik, and Muhammed Harun Kilic are in the first place. It is invaluable to know that there will be a group of people to motivate and support me in every time.

A desired respect and thanks for my parents, Dr. Nurhan Sahin and Dr. Kazim Sahin, for supporting me since the beginning and even sacrificing their future to raise me and my brother with good ethics and scientific background. None of this would have been possible without their unconditional love and support throughout my life. I also would like to express my gratitude to my dear brother, Dr. Taha Koray Sahin, for always feeling his presence no matter wherever he is.

My deepest gratitude goes to my wife, Beyza Nur Ercoskun Sahin, for all of her sacrifice, support, and patience during my study. Many thanks to Ayse and Ali Ercoskun, for providing prayers for my tough journey.

Table of Contents

List of Tables	iv
List of Figures	v
Abstract	viii
Chapter 1: Introduction	1
1.1 Scope of Dissertation	2
1.2 Contributions	2
1.2.1 Waveform Domain NOMA	2
1.2.2 Multicarrier Rate-Splitting Multiple Access	3
1.2.3 Waveform Coexistence for DFRC Systems	4
1.2.4 Control of Electromagnetic Radiation	4
1.3 Dissertation Outline	6
Chapter 2: Next Generation Multiple Access	7
2.1 Background and Related Works	7
2.2 Power-Domain NOMA	8
2.3 Code-Domain NOMA	11
2.4 Waveform Domain NOMA	13
2.4.1 Waveform Selection	14
2.4.2 Reconstruction of the Waveform	15
2.4.3 System Model for the Proposed Waveform Domain NOMA Scheme in Uplink Transmission	16
2.4.3.1 OFDM Based Conventional PD-NOMA in Up- link Transmission	17
2.4.3.2 Proposed Waveform Domain NOMA Scheme for Uplink Transmission	19
2.4.4 LLR Calculations for the Proposed Uplink Transmission	19
2.4.4.1 LLR Calculations for OFDM Based Conventional NOMA in Uplink Transmission	20
2.4.4.2 LLR Calculations for the Proposed Waveform Domain NOMA in Uplink Transmission	20
2.4.5 System Model for the Proposed Waveform Domain NOMA Scheme in Downlink Transmission	21
2.4.5.1 OFDM Based Conventional PD-NOMA in Down- link Transmission	22

2.4.5.2	Proposed Waveform Domain NOMA Scheme for Downlink Transmission	23
2.4.6	LLR Calculations for the Proposed Downlink Transmission	26
2.4.6.1	LLR Calculations for OFDM Based Conventional NOMA in Downlink Transmission	26
2.4.6.2	LLR Calculations for the Proposed Waveform Domain NOMA in Downlink Transmission	27
2.4.7	Simulation Results	28
2.4.7.1	Numerical Evaluation for Waveform Domain NOMA in Uplink System	29
2.4.7.2	Numerical Evaluation for Waveform Domain NOMA in Downlink System	31
Chapter 3:	Rate-Splitting Multiple Accessing	34
3.1	Introduction	34
3.2	System Model	36
3.2.1	OFDM Transmission for K Users	36
3.2.2	Channel Model	37
3.3	Proposed OFDM-RSMA Scheme	38
3.4	OFDM-NOMA Transmission	42
3.5	Simulation Results	43
Chapter 4:	Dual-Functional Radar and Communication Systems	47
4.1	Need for Integration of Radar-Sensing and Communication	48
4.2	NOMA-based Joint Sensing and Communication	49
4.2.1	System Model	49
4.2.2	Transmission Design	49
4.2.3	Channel Effect	53
4.2.4	Multi-functional Reception	54
4.2.4.1	Bi-static Radar Functionality	55
4.2.4.2	Communication Functionality	56
4.2.5	Numerical Evaluation of the Proposed NOMA Scheme	58
4.3	OFDM-IM for DFRC Systems	62
4.3.1	System Model	65
4.3.1.1	Transmitter Design	65
4.3.1.2	Channel Model	67
4.3.2	Bi-static Radar and Channel Estimation	69
4.3.2.1	Null Subcarrier Estimation	70
4.3.2.2	De-chirping	70
4.3.2.3	Delay and Doppler Shift Estimation	71
4.3.2.4	Complex Attenuation Estimation	71
4.3.3	Communication Functionality and Decoding Algorithms	72
4.3.3.1	Null Subcarrier Estimation Based Decoding	72
4.3.3.2	Maximum-likelihood Based Decoding	73
4.3.3.3	Soft Decoding with Channel Decoder	73

4.3.3.4 Complexity Analysis	75
4.3.4 Simulation Results	75
Chapter 5: Control of Electromagnetic Radiation on Coexisting Smart Radio	
Environment	82
5.1 Introduction	82
5.1.1 Vision for 6G	82
5.1.2 Shifting from Cognitive Radio to Smart Radio Environment	83
5.1.3 Contribution	86
5.2 Multiple RIS to Extend the Coverage of Secondary Systems	88
5.2.1 State of the Art	88
5.2.2 System Model	89
5.2.3 Problem Formulation for Coverage Extension	92
5.2.4 Numerical Results	94
5.3 Repositionable Dynamic RIS Deployment	95
5.3.1 State of the Art	95
5.3.2 Methodology	98
5.3.3 Problem Formulation to Control Channel Clusters	99
5.3.4 Numerical Results	100
5.4 Creation of Radiation Rejection Zone via ABCs	101
5.4.1 State of the Art	101
5.4.2 Methodology	102
5.4.3 Problem Formulation for Nulling the Zones	104
5.4.4 Numerical Results	105
5.5 Radiation Control with Repositionable Dynamic RIS and ABCs	106
5.6 Machine Learning to Form Spectrum Map	110
5.6.1 State of Art	110
5.6.2 Spectrum Sensors Applying Backscatter Communications	111
5.6.3 Support Vector Machine to Classify Spectrum Map	112
5.6.4 Numerical Results	114
5.7 Future Research Direction and Challanges	116
5.7.1 Application Centric Coexisting Smart Radio	116
5.7.2 Real Time Test-bed	116
5.7.3 Realistic and Sophisticated RIS and ABC	117
5.7.4 Performance Limits of RIS and ABC Assisted Networks	117
5.7.5 Federated Learning to Manage Spectrum Map	117
5.7.6 Total Energy Consumption and Cost of RIS and ABC	118
Chapter 6: Conclusion	119
References	121
Appendix A: Copyright Permissions	144
About the Author	End Page

List of Tables

Table 2.1	Fundamental Points on the Waveform Design	14
Table 4.1	Simulation Parameters for NOMA Based DFRC System	58
Table 4.2	Simulation Parameters for OFDM-IM Based DFRC Analysis	76
Table 5.1	Simulation Parameters for Coverage Extension	95

List of Figures

Figure 2.1	System model for power-domain non-orthogonal multiple accessing.	9
Figure 2.2	The timeline of NOMA studies in 3GPP standardization.	10
Figure 2.3	Sparse coding multiple accessing (SCMA) system model.	12
Figure 2.4	Comparison of reconstruction schemes for different MSE (σ_e^2) in channel estimation.	17
Figure 2.5	Two users uplink NOMA scheme with OFDM-IM+OFDM.	18
Figure 2.6	Two users downlink NOMA scheme with OFDM-IM+OFDM.	22
Figure 2.7	Coding and modulating of user 1 (OFDM-IM) and user 2 (OFDM) signals.	24
Figure 2.8	Demodulating and decoding of the superimposed received signal with LDPC codes aided soft reconstruction and cancellation.	24
Figure 2.9	User 1 BLER for uncoded uplink NOMA schemes in AWGN.	28
Figure 2.10	User 2 BLER for uncoded uplink NOMA schemes in AWGN.	29
Figure 2.11	User 1 BLER for coded uplink NOMA schemes in AWGN.	29
Figure 2.12	User 2 BLER for coded uplink NOMA schemes in AWGN.	30
Figure 2.13	Comparison of conventional and proposed uplink NOMA schemes in frequency selective channel with tap number is 10.	31
Figure 2.14	BLER of user 1 of the downlink NOMA schemes in frequency selective channel.	32
Figure 2.15	BLER of user 2 of the downlink NOMA schemes in frequency selective channel.	33
Figure 3.1	Conventional OFDMA with two users showing channel power of users (dashed line) and power allocation (solid box).	37
Figure 3.2	OFDM-NOMA with two users showing channel power of users (dashed line) and power allocation (solid box).	37

Figure 3.3	OFDM-RSMA with two users showing channel power of users (dashed line) and power allocation (solid box).	38
Figure 3.4	Proposed OFDM-RSMA scheme.	39
Figure 3.5	Performance comparison of OFDMA, OFDM-NOMA, OFDM-RSMA and one user OFDM under flat fading channel.	44
Figure 3.6	Sum-rate comparison of OFDMA, OFDM-NOMA, and OFDM-RSMA under the frequency selective and doubly selective channels.	45
Figure 4.1	Vehicular to vehicular (V2V) system model needing both radar-sensing and communication functionality.	50
Figure 4.2	Generalized framework for joint radar-sensing and communication.	51
Figure 4.3	Transmission and reception operations of the proposed NOMA scheme for joint radar-sensing and communication.	51
Figure 4.4	Time-power representation of proposed NOMA frame for DFRC.	52
Figure 4.5	Time-frequency representation of proposed NOMA frame for DFRC.	53
Figure 4.6	Radar-sensing performance of the proposed NOMA scheme at 10 dB SNR.	59
Figure 4.7	Radar-sensing performance of the conventional OFDM scheme with comb-type pilot structure at 10 dB SNR.	60
Figure 4.8	MSE of proposed method at 20 dB.	61
Figure 4.9	BER performance of proposed method at 20 dB.	62
Figure 4.10	Transmitter structure for the m^{th} OFDM symbol of the proposed DFRC system.	64
Figure 4.11	Look-up table for two active subcarriers out of four subcarriers in a subblock.	65
Figure 4.12	Transmitted OFDM-IM JCR frame.	65
Figure 4.13	Decoding process for an OFDM-IM frame of the proposed DFRC system.	69
Figure 4.14	Sensing performance of the conventional OFDM with comb-pilots.	74
Figure 4.15	Sensing performance of the proposed OFDM-IM based DFRC system.	75
Figure 4.16	MSE vs SNR analysis under three targets	77
Figure 4.17	BER vs SNR analysis under three targets.	78

Figure 4.18	MSE vs SNR analysis under four targets.	79
Figure 4.19	BER vs SNR analysis under four targets.	80
Figure 5.1	Shaping the electromagnetic energy using repositionable dynamic RISs and ABC nodes.	84
Figure 5.2	System structure including multiple RISs for coverage extension, multiple coordinated ABCs for radiation rejection.	89
Figure 5.3	Demonstration of coverage extension when only BS is used to extend where the color map is scaled in dB.	96
Figure 5.4	Demonstration for the power distribution regarding shadowing and path-loss effects.	97
Figure 5.5	Demonstration of coverage extension with two RISs compared where the color map is scaled in dB.	98
Figure 5.6	Numerical evaluation of capacity of the proposed system showing the advantage of repositionable dynamic RIS.	101
Figure 5.7	Demonstration of zone protection only with BS beamforming antennas are optimized where the color map is scaled in dB.	105
Figure 5.8	Demonstration of zone protection of proposed system architecture with multiple ABCs where the color map is scaled in dB.	105
Figure 5.9	Convergence performance of the proposed method and its comparison with the case where RISs and ABCs are absent.	107
Figure 5.10	Demonstration of radiation control with only BS beamforming where the color map is scaled in dB.	108
Figure 5.11	Demonstration of radiation control with repositionable dynamic RISs and multiple ABCs where the color map is scaled in dB.	109
Figure 5.12	Spectrum activity sensor generates low-rate data that is transmitted via backscatter communication to DFC so that edge AI can forecasts spectrum activities to dynamically adjust RISs.	111
Figure 5.13	Reconstruction of spectrum.	115

Abstract

The growing interest in diverse wireless applications such as virtual reality (VR), digital twin, ultra-massive broadband communication (u-MBB) has led the cellular industry to look for new multiple accessing schemes and new signal processing techniques for utilization of next-generation wireless technologies. Throughout the PhD duration, different studies are performed in regards to dual-functional and interference robust multiple accessing and control of electromagnetic radiation for cognitive radio systems. Firstly, a novel concept on non-orthogonal multiple access (NOMA), which is the coexistence of different waveform structures in the same resource elements is proposed. Secondly, a novel JCR waveform is proposed to serve both communication and radar applications with the same resources. Thirdly, rate-splitting (RS) in OFDM waveform is investigated. It is shown that even in single-input single-output (SISO) BC scenario, the proposed OFDM-RSMA outperforms OFDM-NOMA and OFDMA in diverse channel conditions. Finally, the formation of smart radio environment is introduced considering efficient utilization of radio spectrum in any given geographical area, which can be also viewed as a generalization of cognitive radio technology.

Chapter 1: Introduction

Over the last two decades, the traffic in mobile broadband (MBB) networks has increased 50-70% each year all around the world [1]. Immense traffic growth results in the need for the capacity growth to maintain the quality of service. To cater for this huge traffic growth, mobile networks must provide corresponding capacity growth. Evolving a network requires increased capacity over the time within available spectrum to maintain high service quality. Compared to current wireless networks like 5G, Wi-Fi, and WLAN, next-generation wireless networks are expected to achieve significantly higher capacity, extremely low latency, ultra-high reliability, as well as massive and ubiquitous connectivity in order to meet diverse innovative applications such as virtual reality (VR), augmented reality (AR), holographic communication, digital replica and non-terrestrial networks (NTN) networks [2].

In contrast to 5G and earlier generations, the next generation of wireless systems requires environmental awareness to leverage adjustable radio parameters into communication. Therefore, radar-sensing systems will be integrated into the wireless networks to cope with specific applications and use cases such as autonomous vehicles and environment-aware access points. Also, it is expected that this new paradigm supports flexible and seamless connectivity [3]. A key-enabler of high-mobility networks is the ability of a node to track its dynamically changing environment continuously and react accordingly. Although state sensing and communication have been designed separately in the past; power, spectral efficiency, hardware costs encourage the integration of these two functions, such that they are operated by sharing the same frequency band and hardware [4].

Beside increasing data-rate tremendously, the use of higher frequency ranges, wider bandwidths, and massive antenna arrays leads to enhanced sensing solutions with very fine range,

Doppler and angular resolutions, as well as localization to a cm-level degree of accuracy. Moreover, new materials, device types, and reconfigurable intelligent surface (RIS) will allow network operators to reshape and control the electromagnetic response of the environment. At the same time, machine learning and artificial intelligence will leverage the unprecedented availability of data and computing resources to tackle the biggest and hardest problems in both wireless communication and radar-sensing systems. Therefore, the convergence of these two applications will continue to create new research areas and innovations.

1.1 Scope of Dissertation

The scope of the dissertation is to design novel multiple accessing and waveform schemes to enable massive connectivity, dual-functionality including radar-sensing and communication, interference resilient transmission for next-generation wireless systems. Initially, the chapters provide system model and background research and then, include performance results of the proposed architecture and comparisons with the conventional methods studied in the literature.

1.2 Contributions

Here, the contributions of studies performed throughout the PhD is briefly explained.

1.2.1 Waveform Domain NOMA

This study proposes a novel non-orthogonal multiple access (NOMA) scheme called waveform-domain NOMA with transceiver design utilizing low density parity coding (LDPC) codes aided soft interference cancellation to improve block error rate (BLER) performance through all received power level variations of users. The contributions of this study can be listed as follows:

- A novel power-balanced downlink NOMA transceiver design consisting of two different waveforms orthogonal frequency division multiplexing (OFDM) and OFDM-index modulation (OFDM-IM) is proposed.
- The log-likelihood ratio (LLR) calculations are evaluated depending on the waveform type that is decoded first.
- The reconstruction of the firstly decoded user's waveform is investigated with two different techniques in terms of error vector magnitude (EVM) as well as considering channel estimation errors.

It is shown that the proposed waveform-domain NOMA scheme outperforms the conventional power-domain NOMA scheme in terms of BLER performance in the power-balanced scenarios. Moreover, waveform-domain NOMA provides flexibility among users regarding their demands.

1.2.2 Multicarrier Rate-Splitting Multiple Access

Rate-splitting multiple access (RSMA) is a multiple access technique generalizing conventional techniques, such as, space-division multiple access (SDMA), NOMA, and physical layer multi-casting, which aims to address multi-user interference (MUI) in multiple-input multiple-output (MIMO) systems. In this study, we leverage the interference management capabilities of RSMA to tackle the issue of inter-carrier interference (ICI) in OFDM waveform. The main contributions of the study are as follows:

- The analogy between RSMA in multiple-input single-output (MISO)-broadcast channel (BC) and RSMA in single-input single-output (SISO) under OFDM waveform is constructed showing that multi-numerology OFDM technique can be exploited to overcome the ICI.
- The drawback of OFDM-NOMA scheme is explained that hinders to utilize frequency selectivity of the channel due to block decoding structure of OFDM waveform.

- Rate-splitting is studied on the OFDM waveform to combat the effects of different channel conditions including frequency selectivity and time selectivity. Subcarrier and power allocation to maximize the sum-rate is formulated in OFDM-RSMA.

1.2.3 Waveform Coexistence for DFRC Systems

The demand for dual-functional wireless systems is on the rise as certain resources become more congested and scarce. joint communication and radar (JCR) is a promising technology that is becoming very critical and growing in popularity, where communication and radar applications are serviced simultaneously sharing the same hardware/software and the frequency band resources. JCR and its alternatives need to be cleverly integrated into certain waveforms such as OFDM to function properly without a degradation in the performance. Following contributions are done in the field of merging radar-sensing and communication systems:

- Joint radar-sensing and communication is studied in the view of waveform coexistence on the same resources.
- The superiority of the proposed NOMA scheme for joint radar-sensing and communication is demonstrated in terms of ambiguity in radar-sensing functionality, channel estimation mean-squared-error (MSE) and bit-error-rate (BER) performance by comparing with the existing OFDM JRC system which is derived from conventional comb-type pilot based OFDM.
- A novel JCR waveform scheme is proposed using the OFDM-IM structure and Golay complementary sequences (GCS) as radar symbols.

1.2.4 Control of Electromagnetic Radiation

A smart and reconfigurable radio technology is demonstrated where the superiority of mutual usage of RIS and ambient backscatter communication (ABC) in terms of shaping the

electromagnetic energy in coexisting radio systems is presented. First, the use of multiple RISs is studied to enhance the capacity of secondary use inside the specific area by shaping the electromagnetic energy in the spatial domain. Secondly, a new degree of freedom with repositionable dynamic RIS is introduced. Controlling the time varied shadowing effects by re-positioning the RIS, it is shown that 15% more capacity can be achieved. Finally, the use of multiple coordinated ABCs to protect the region of primary use against the radiation due the secondary uses is investigated. The main contributions of the study can be summarized as follows:

- The smart radio environment system is proposed utilizing novel technologies such as repositionable RIS and coordinated ABC to control spatial electromagnetic radiation by creating radiation rejection and coverage extension zones.
- For the first time in the literature, it is introduced that the repositionable RISs are utilized to extend the coverage of co-existing secondary systems and coarse radiation rejection for primary systems by having much more control on the exploitation of channel clusters as well as shadowing effects that may causes high power fluctuations in a short time frame. In numerical evaluations, introducing multiple static coordinated RIS, it is demonstrated that at least 5 dB increase can be obtained in the power of secondary system along the specific region.
- It is also novelly studied that a group of coordinated ABC nodes are proposed to create man-made deep fades which greatly reduce the interference from secondary use into the radiation rejection zone hosting primary passive and active uses. Simulation results demonstrates that the use of coordinated multiple ABC nodes provides nearly 10 dB interference rejection in the vicinity of primary user.
- The coexistence of all proposed concepts is studied with joint optimization of coverage extension area and radiation rejection zone using both repositionable RIS and coordinated ABCs.

1.3 Dissertation Outline

Chapter 1 provides brief introduction about the studies performed during Ph.D. term. Chapter 2 presents the need for next-generation multiple accessing schemes. The studies that are proposed as a remedy for conventional non-orthogonal multiple accessing and orthogonal multiple accessing are introduced. The novel waveform-domain NOMA concept is presented and compared with the conventional power-domain NOMA scheme. The numerical results demonstrate that the proposed waveform-domain NOMA scheme is capable of overcoming the problems of power-domain NOMA in power-balanced scenarios. In Chapter 3, a novel concept which is called OFDM-RSMA is introduced. A promising concept, dual-functional radar and communication, which merges two highly studied concepts are introduced in Chapter 4. Novel waveform and wireless systems structures are explained. In Chapter 5, control of electromagnetic radiation on coexisting smart radio environment is introduced where two novel technologies, reconfigurable intelligent surfaces and ambient backscatter communications are utilized supported with machine learning. Finally, Chapter 6 concludes the dissertation with possible future research directions.

Chapter 2: Next Generation Multiple Access

This chapter¹ initially introduces the importance of novel multiple accessing designs that need to overcome current solutions. Then, waveform-domain NOMA concept introduced by authors are explained.

Over the last two decades, the traffic in MBB networks has increased 50-70% each year all around the world [1]. Immense traffic growth results in the need for the capacity growth to maintain the quality of service. Compared to current wireless networks like 5G, Wi-Fi, and WLAN, next-generation wireless networks are expected to achieve significantly higher capacity, extremely low latency, ultra-high reliability, as well as massive and ubiquitous connectivity in order to meet diverse innovative applications such as VR, AR, holographic communication, digital replica and NTN networks [8, 2]. Moreover, the evolution toward next-generation wireless networks requires a paradigm shift from the communication-oriented design to a multi-functional design, including communication, sensing, imaging, computing, and highly accurate positioning capabilities with mobility. To meet these requirements of diverse applications, advanced multiple accessing schemes are expected to be studied that are capable of supporting massive numbers of users in a more efficient manner in terms of resource and computational complexity [9].

2.1 Background and Related Works

It has been shown that orthogonal transmission is vulnerable to the interferences that destroy the orthogonality of the signalling scheme which are named differently such as inter-symbol interference (ISI), ICI, MUI, and adjacent channel interference (ACI) [10, 11, 12]. At

¹First three sections of this chapter are published in [5] and [6], fourth section is published in [7]. Permissions are included in Appendix A.

the same time, it can only support limited number of users in a given orthogonal resources [13]. Supported with theoretical foundations [14], non-orthogonal transmission have been taking interest from academia and industry for many years to meet the demand on explosively growing number of users/devices in next generation wireless networks (NGMA). Since 2G mobile systems, different non-orthogonal transmission schemes are studied to circumvent the limitations encountered in the orthogonal transmission [15, 16]. Non-orthogonal spreading sequences are utilized in the techniques of IS-95, wideband code division multiple access (CDMA) (WCDMA), and CDMA2000 which are the core technologies of 2G and 3G. Moreover, multi-user superposition transmission (MUST) has been considered as a candidate multiple accessing scheme in 4G LTE-A systems where messages of cell-edge and cell-interior users are proposed to be superimposed on the same resource element [17]. MUST scenario guarantees the decodability of messages exploiting substantial power difference between users. A non-orthogonal strategy that has gained popularity in 5G is called NOMA, having two widely studied forms, power-domain NOMA (PD-NOMA) and code-domain NOMA (CD-NOMA) [18].

2.2 Power-Domain NOMA

PD-NOMA depicted in Figure 2.1 serves multiple users in the same time-frequency resource block, and separates them in the power domain using superposition coding (SC) and successive interference cancellation (SIC) techniques [19]. PD-NOMA allows superposition of users' messages for transmission, and the MUI ensuing from this non-orthogonal transmission is decoded and removed via SIC at the receiver. In single-antenna systems, e.g. SISO BCs, PD-NOMA has been shown to achieve higher spectral efficiency (SE) than orthogonal multiple access (OMA) and simultaneously serve higher number of users at an additional cost of increased transceiver complexity [20, 21].

Power-domain NOMA can yield much better spectral efficiency compared to OMA unless channel gains of users are not similar [22]. To date, the literature on power-domain NOMA

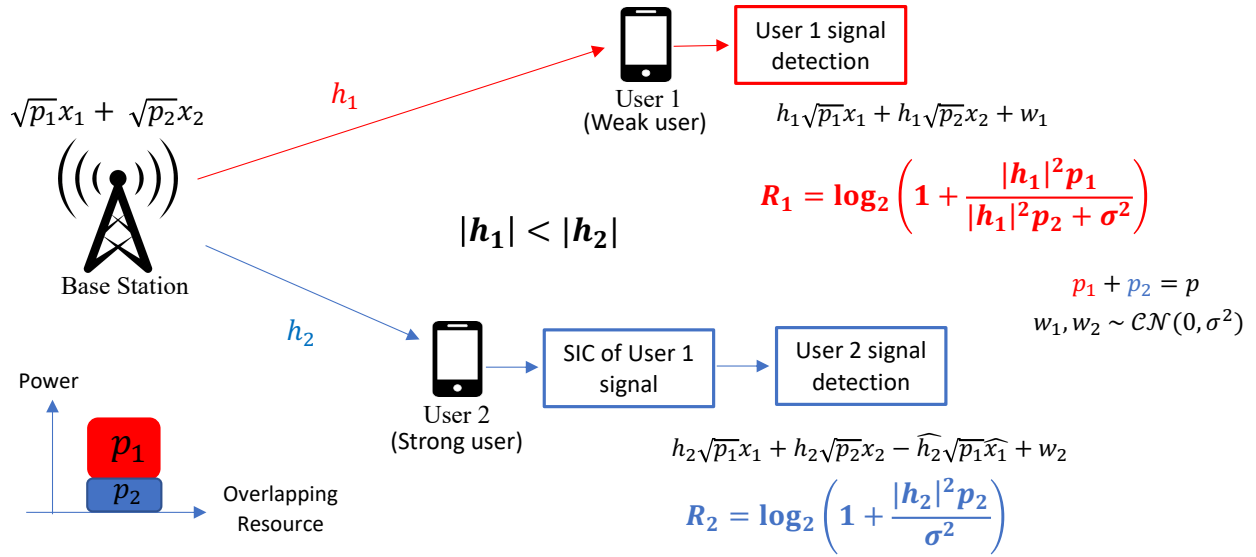


Figure 2.1: System model for power-domain non-orthogonal multiple accessing.

has based its work on perfect SIC process [21], i.e., there is no residual error during the detection, reconstruction, and subtraction of the decoded user's waveform from the superimposed received signal. However, this assumption is infeasible because the signal of the firstly decoded user should be estimated perfectly at the receiver [23]. Additionally, although the impact of channel estimation accuracy on the performance of BLER is negligible for downlink NOMA [24], it should be considered for uplink NOMA regarding the reconstruction of firstly decoded user's waveform. On the other hand, the transmit power of users is arranged in a way that the users' power received at the base station (BS) is significantly different in order to enhance the overall system throughput in power-domain NOMA [25]. Since users transmitting at a similar power level may also be grouped in the case of high connectivity, various researches have been conducted to find new NOMA schemes that operate in power-balanced scenarios [26].

The idea of serving multiple users in the same wireless resources, including frequency, time, code, and space, has become an appealing research area over almost thirty years. Efforts to investigate new types of multiple access techniques under the constraint of scarce resources are named as multi-user detection and NOMA for decades. The main motivation

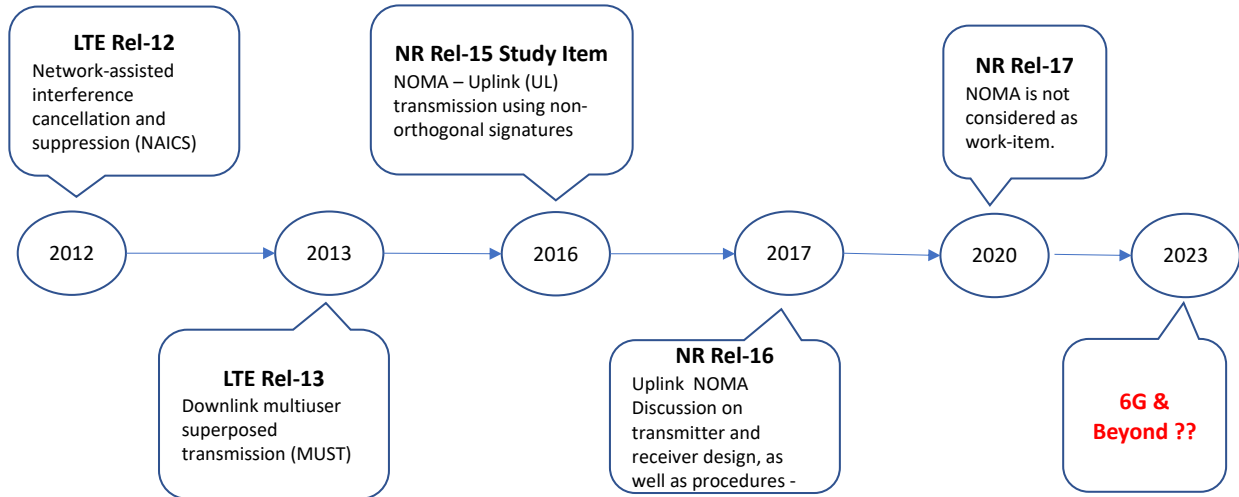


Figure 2.2: The timeline of NOMA studies in 3GPP standardization.

behind NOMA having two different techniques, such as power-domain and code-domain, is the increased connectivity compared to OMA, which can meet the harsh requirements of the Internet of Things (IoT) [27]. Several NOMA schemes have been integrated into various standardization efforts. In LTE, the downlink NOMA scheme, called multi-user superposition transmission (MUST), was studied for the 3rd Generation Partnership Project (3GPP) Release 14 [28], whose motivation is weak in 5G, because higher performance gains can be provided with downlink massive MIMO [29]. A study on the application of NOMA for uplink transmission has been recently carried out for 3GPP Release 16, where different implementations of NOMA have been studied [30]. However, since power-domain NOMA has performance degradation in some cases, such as imperfect SIC and strict power control, it is not considered as a work-item in Release 17 [31]. The timeline of NOMA in 3GPP standardization process is depicted in Figure 2.2.

On the other hand, the transmit power of users is arranged in a way that the users' power received at the BS is significantly different in order to enhance the overall system throughput in power-domain NOMA [25]. This arrangement in power-domain NOMA introduces additional computational complexity that dynamically monitors the wireless system. Moreover, users transmitting at a similar power level may also be grouped in the case of high

connectivity. Therefore, various researches have been conducted to find new NOMA schemes that operate in power-balanced scenarios [26]. Also, the design principle of forcing a user to fully decode the interference from other users limits the advantages of PD-NOMA [32]. To overcome the drawbacks of NOMA, several schemes are proposed, for example, authors have come up with the concept of waveform-domain NOMA enabling the coexistence of different waveforms dedicated to different applications [6, 7, 33]. It is shown that waveform-domain NOMA concept provides significant performance improvement in the power-balanced scenario where conventional PD-NOMA suffers.

2.3 Code-Domain NOMA

Code-domain NOMA uses user-specific sequences for sharing the entire radio resource [19]. In the literature, there are several different techniques regarding code domain NOMA, such as sparse code multiple access (SCMA) [34], interleave division multiple access (IDMA) [35], pattern division multiple access (PDMA) [36], low density spreading multiple access (LDS-MA) [37]. In this section, the most common one, which is SCMA, will be investigated. In this scheme, the encoding operations, for both the uplink and downlink, involve replacing the quadrature amplitude modulation (QAM) modulator with an SCMA modulator, which maps the coded bits directly to the multi-dimensional codeword from the standardized codebooks. The decoding operations replace the single-user channel equalization and QAM de-mapper of existing LTE receiver with an SCMA demodulator that jointly detects the superposed data layers and output separate LLR results to the turbo decoders of each layer [34].

SCMA is capable of supporting overloaded access over the coding domain, hence increasing the overall rate and connectivity. By carefully designing the codebook and multi-dimensional modulation constellations, the coding and shaping gain can be obtained simultaneously. In an SCMA system, users occupy the same resource blocks in a low-density way, which allows affordable low multi-user joint detection complexity at the receiver. The

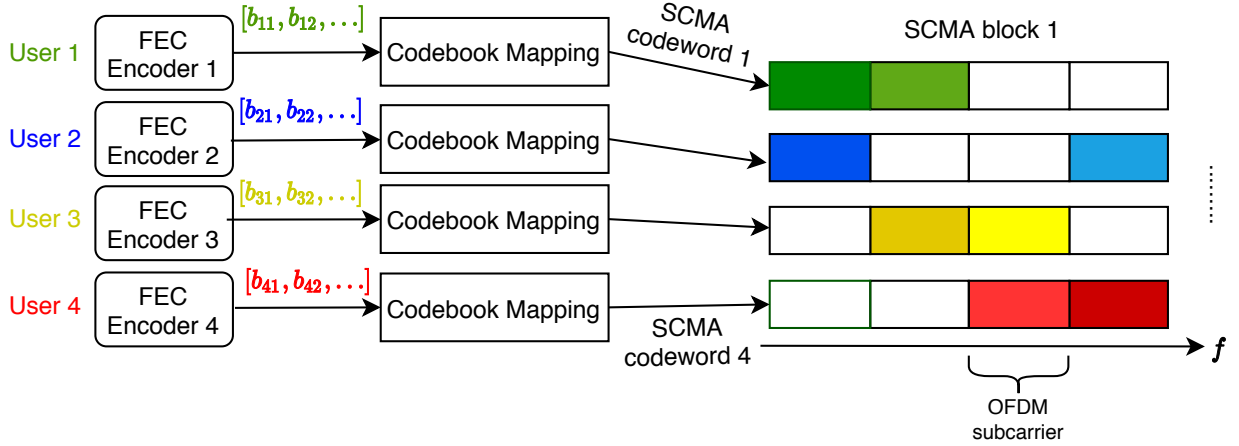


Figure 2.3: Sparse coding multiple accessing (SCMA) system model.

sparsity of signal guarantees a small collision even for a large number of concurrent users, and the spread-coding like code design brings good coverage and anti-interference capability due to spreading gain as well [19].

An SCMA transmitter system model can be illustrated in Figure 2.3 where K synchronous users multiplexing over N share orthogonal resources. Each SCMA codebook maps the coded bits $b_{k,n}$ to a N -dimensional complex codeword. Generated codewords are superimposed over the air transmission in uplink or at the transmitter in downlink, constituting an SCMA block. This multiple access process is similar to that of CDMA, where the spread signals are replaced with the SCMA codewords. Multi-user detection is carried out at the receiver to recover the colliding codewords. Beside, SCMA uses sparse spreading to reduce inter-layer interference, so that more codewords collisions can be tolerated with low receiver complexity [19].

In order to strike a good balance between link performance (close to maximum-likelihood detection and robust to channel imperfection) and implementation complexity (the complexity of the receiver), the features of SIC with message-passing algorithm (MPA) can be combined to have a SIC-MPA receiver which developed to reduce the complexity of conventional MPA receiver. Specifically, MPA is first applied to a limited number of layers, so that the number of colliding layers over each resource element does not exceed a given threshold

value. Then, the successfully decoded MPA layers are removed by SIC, and the procedure continues until all layers are successfully decoded, or no new data layer gets successfully decoded by MPA. Due to the fact that MPA is used for a limited number of layers instead of all the layers, the decoding complexity is greatly reduced [38].

2.4 Waveform Domain NOMA

Waveform design is one of the core components of the physical layer in wireless communication systems. Basically, waveform can be defined as a physical signal that contains information. These signals occupy physical resources in multi-dimensional hyper-space consisting of time, frequency, space, code, power and beam. The main components of the waveform design procedure are shown in Table 2.1, including data and redundant symbols, lattice structure, pulse shape and frame structure. Waveform designs employ various parameters under these main components [39, 40]. The waveform consisting of symbol, pulse shape, and lattice is the physical shape of the signal carrying modulated information [41].

Possible spacings between lattice points are defined by the numerology structure of a waveform. Numerology includes a set of parameters for a specific lattice structure of a waveform and 5G NR is standardized based on multiple numerologies of cyclic prefix (CP)-OFDM on the time frequency plane. For 5G NR, parameters that define numerology type of the waveform are subcarrier spacing, CP duration, inter-numerology guard band, roll-off factor, filter coefficients, slot duration, number of symbols in one slot, number of slots per subframe, and frame length.

The novel waveform-domain NOMA concept proposes the combination of different waveforms along with the non-orthogonal resources to introduce flexibility, separability, and detectability.

Table 2.1: Fundamental Points on the Waveform Design

Parameter	Feature
Data symbols	They are a set of complex numbers representing information bits.
Redundant symbols	They can be utilized for precoding, guard utilization and artificial noise generation.
Lattice structure	It represents locations of samples in hyper-space. It is a multi-dimensional resource mapping and each mapped sample shows a location of one resource element.
Pulse shape	The form of symbols in the signal plane is defined by the pulse shaping filters. The shape of filters determines how the energy is spread over the multi-dimensional hyper-space.
Frame structure	It can be defined as a packaging of multiple user information because the waveform design is the process of generating the collective physical signal, which occupies the hyper-space, corresponding to multiple users.

2.4.1 Waveform Selection

Some intelligent techniques for overlapping of users with different waveforms are studied in the prior works [42, 43, 44]. In [42], the separability aspect on the overlapping of two different waveforms, which are OFDM and CDMA, is investigated with an iterative receiver design that is computationally complex. Similarly, the coexistence of OFDM and single carrier frequency division multiple access (SC-FDMA) is studied in [43]. It is shown that the proposed multi-user detection (MUD) approach utilizing iterative likelihood testing and signal-to-interference-plus-noise ratio (SINR) based processing outperforms conventional SIC. Moreover, the orthogonal time-frequency space (OTFS) waveform is used for the high mobility user, whereas the signal of the low mobility user is transmitted via the OFDM waveform in [44]. This NOMA concept provides flexibility among users according to their mobility profiles. In our study, due to some superiority of OFDM-IM over OFDM such as

ergodic achievable rate, peak-to-average power ratio (PAPR) reduction, and robustness to ICI [45], OFDM-IM is chosen as a candidate for waveform-domain NOMA.

2.4.2 Reconstruction of the Waveform

In the uplink NOMA, errors in channel estimation and information detection propagate through the users coming in successive decoding order. To mitigate the performance degradation, we have used LDPC codes aided soft-interference cancellation. The soft reconstruction scheme is compared with the reencoding scheme proposed in [46] in terms of EVM performance.

EVM is calculated as the ratio of root mean squared (RMS) power of the error vector to the RMS power of the reference symbol overall OFDM subcarriers. For user 1, EVM is calculated as follows:

$$\text{EVM(dB)} = 10 \log_{10} \left(\sqrt{\frac{\sum_{n=1}^N \|\hat{u}_{1,n} - u_{1,n}\|^2}{\sum_{n=1}^N \|u_{1,n}\|^2}} \right),$$

where $\hat{u}_{1,n}$ corresponds to the reconstructed symbol of user 1 at the n th subcarrier. Two different techniques are used to reconstruct the decoded waveform to be stripped away from the superimposed received signal:

1. If the signal of user 1 is demodulated first, the decoded bits of user 1 are reencoded and remodulated to reconstruct the waveform of user 1. Then it is subtracted from the superimposed signal to decode the signal of user 2.
2. For the reconstruction of the firstly decoded signal, we have utilized the Gallager sum-product algorithm [47] that provides the total LLR of each variable node at the stopping stage. The total LLR shows how reliable the symbol consisting of the related bit can be reconstructed. Soft decision reconstruction is done at the end of the iterative

process of the sum-product algorithm over the variable node v_i as follows:

$$\zeta = \tanh(L_i), \quad (2.1)$$

where ζ denotes the scale factor for the symbol consisting of the related bit i and L_i is the sum of the extrinsic LLRs from connected check nodes and initial LLR of the bit i . For example, in BPSK modulation, the reconstructed signal of user 2 for the i th bit on the n th subcarrier becomes $\hat{u}_{2,n} = -\sqrt{p_2} \tanh(L_i)$. Subsequently, the reconstructed signal is canceled from the aggregate received signal to decode the signal of another user.

Comparison of different reconstruction schemes is evaluated through Monte Carlo simulations over the Frequency Selective Channel with 10 taps. Power delay profile (PDP) of the channel is considered as uniform. Moreover, MSE is defined as the expected value of the normalized difference between the channel response h and the channel estimation \tilde{h} , $\sigma_e^2 = \frac{\mathbb{E}[|\tilde{h}-h|^2]}{\mathbb{E}[|h|^2]}$, where $\mathbb{E}[\cdot]$ denotes the expected value. In Figure 2.4, EVM results are provided for different MSEs in channel estimation. It portrays the superiority of the proposed reconstruction scheme with extrinsic soft LLRs information obtained from the LDPC decoder. It can also be seen that, in the uplink NOMA, accuracy in channel estimation has a high impact on the reconstruction of the firstly decoded user's waveform.

2.4.3 System Model for the Proposed Waveform Domain NOMA Scheme in Uplink Transmission

For brevity, consider two users uplink NOMA scenario where both users transmit to a single BS over N subcarriers in the presence of frequency selective channels, including additive white Gaussian noise (AWGN).

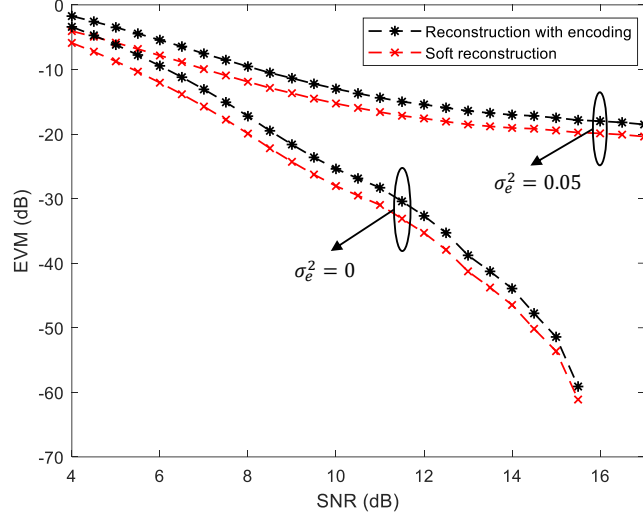


Figure 2.4: Comparison of reconstruction schemes for different MSE (σ_e^2) in channel estimation.

2.4.3.1 OFDM Based Conventional PD-NOMA in Uplink Transmission

Firstly, both user equipments (UEs) encode their messages by LDPC codes and modulate via QAM, where data symbols of users are drawn from a complex symbol alphabet \mathbb{S} . Then, these symbols are OFDM modulated and transmitted to be received by the BS over the same resource element (RE). Moreover, p_1 and p_2 denote the signal power of user 1 and user 2 for each subcarrier, respectively. In the OFDM with total N subcarriers, the total powers of user 1 and user 2 become $P_1 = Np_1$ and $P_2 = Np_2$, respectively. After the process of fast Fourier transform (FFT) and removal of cyclic prefix, the baseband received signal at the n th subcarrier is expressed as follows:

$$r_n = \sqrt{p_1}h_{1,n}u_{1,n} + \sqrt{p_2}h_{2,n}u_{2,n} + w_n, \quad (2.2)$$

where $h_{1,n}$, $h_{2,n}$, $u_{1,n}$, and $u_{2,n}$ are the channel gains and data symbols of users 1, and 2, respectively. Also, $w_n \sim \mathcal{CN}(0, \sigma^2)$ denotes the AWGN at the n th subcarrier.

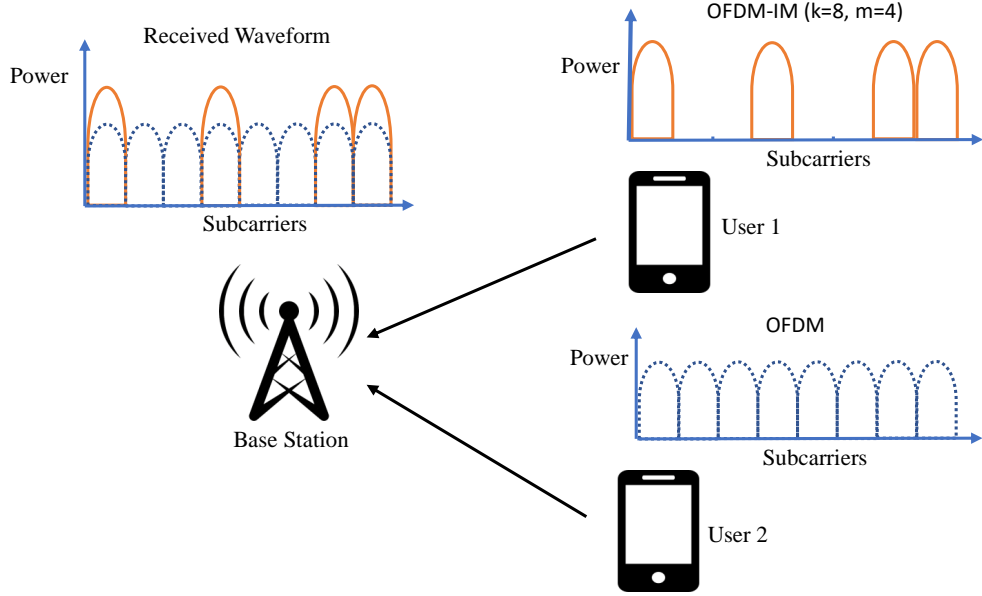


Figure 2.5: Two users uplink NOMA scheme with OFDM-IM+OFDM.

Assuming that the signal of user 1 is decoded first, the capacity of user 1 (R_1) in conventional power-domain NOMA is given by

$$R_1 = \sum_{n=1}^N \log_2 \left(1 + \frac{p_1 h_{1,n}}{\sigma^2 + p_2 h_{2,n}} \right) \text{ bit/s/Hz.} \quad (2.3)$$

Assuming perfect SIC, which is infeasible, the capacity of user 2 (R_2) is calculated as follows:

$$R_2 = \sum_{n=1}^N \log_2 \left(1 + \frac{p_2 h_{2,n}}{\sigma^2} \right) \text{ bit/s/Hz.} \quad (2.4)$$

In the case of maximum likelihood multi-user detection (ML-MUD) without SIC, the decoding order does not have any effect on the sum-rate; therefore, any arbitrary decoding order can be assumed to be performed [48]. On the other hand, when ML-MUD with SIC is used, the stronger user should be decoded first.

2.4.3.2 Proposed Waveform Domain NOMA Scheme for Uplink Transmission

As Figure 2.5 depicts, user 1 has utilized OFDM-IM waveform, whereas user 2 sends its signal via OFDM waveform over N subcarriers. In the OFDM-IM scheme [49], the total $Q = Q_1 + Q_2$ bits are transmitted as follows: Firstly, N subcarriers are split into g subblocks consisting of k subcarriers. The Q_1 bits are used to determine the indices of m active subcarriers where the total number of active subcarrier positions is denoted as c . In each subblock β , only m out of k subcarriers have activated.

Activated subcarriers are used to map Q_2 bits on to M -ary signal constellation symbols selected from the complex set \mathbb{S} . The information of user 1 carried in the subblock β is given by $\mathbf{u}_{1,\beta} = [u_{1,\beta}^{(1)} \dots u_{1,\beta}^{(Q)}]$. The interleaved grouping is performed to increase the achievable rate of OFDM-IM [50]. In subblock β , the vector of modulated symbols of user 2 carried with OFDM waveform is denoted by $\mathbf{u}_{2,\beta} = [u_{2,\beta}^{(1)} \dots u_{2,\beta}^{(k)}]$.

After FFT and cyclic prefix removal, the superimposed received signal at the n th subcarrier becomes

$$r_n = \sqrt{\frac{kP_1}{mN}} h_{1,n} u_{1,n} + \sqrt{P_2} h_{2,n} u_{2,n} + w_k, \quad (2.5)$$

where $u_{1,n} \in \mathcal{S}' = \{0, \mathbb{S}\}$. Moreover, denote $\mathbf{r}_\beta \in \mathbb{C}^{1 \times k}$ as the received signal at the β th subgroup. The reception process of the proposed NOMA scheme is started by decoding the OFDM-IM waveform first. However, the decoding may not always start with the OFDM-IM waveform. It depends on both power, subcarrier allocation, and modulation order.

2.4.4 LLR Calculations for the Proposed Uplink Transmission

This section includes the LLR calculations of each user for two different NOMA schemes. Calculated LLRs are sent to the LDPC decoder as input. For the sake of fair comparison, we have used the log-sum approximation technique [51] to calculate approximate LLRs of two different NOMA schemes.

2.4.4.1 LLR Calculations for OFDM Based Conventional NOMA in Uplink Transmission

With ML-MUD algorithm, the LLR of the bit i of user 1 at the n th subcarrier, $\Lambda_{n^{(i)}}^{u_1}$, is calculated as

$$\begin{aligned} \Lambda_{n^{(i)}}^{u_1} &= \log \left(\frac{f(r_n | u_{1,n}^{(i)} = 0)}{f(r_n | u_{1,n}^{(i)} = 1)} \right) \\ &\approx \min_{u_{1,n}: u_{1,n}^{(i)} \in \mathbb{S}_1^i, u_{2,n} \in \mathbb{S}} \frac{\|r_n - h_{1,n}u_{1,n} - h_{2,n}u_{2,n}\|^2}{\sigma^2} \\ &\quad - \min_{u_{1,n}: u_{1,n}^{(i)} \in \mathbb{S}_0^i, u_{2,n} \in \mathbb{S}} \frac{\|r_n - h_{1,n}u_{1,n} - h_{2,n}u_{2,n}\|^2}{\sigma^2}, \end{aligned} \quad (2.6)$$

where $\mathbb{S}_b^i \subset \mathbb{S}$ denotes the set of all symbols $\alpha \in \mathbb{S}$ whose label has $b \in \{0, 1\}$ in bit position i . The complexity of this LLR calculation, in terms of complex multiplications, becomes $\sim \mathcal{O}(|\mathbb{S}|^2)$. After LDPC decoder fed with LLRs, the symbols of user 1 is reconstructed and subtracted from the superimposed signal with inevitable SIC error. The LLRs of user 2 are calculated with the remaining signal and sent to the LDPC decoder in order to obtain bit decisions of user 2.

2.4.4.2 LLR Calculations for the Proposed Waveform Domain NOMA in Uplink Transmission

The LLR calculations for users' bits in the OFDM-IM+OFDM NOMA scheme depend on which waveform is decided to be decoded first. As it is shown via numerical results, the total power level is not the unique limitation to decide which waveform should be decoded first. By decoding the OFDM-IM waveform first, the LLR of the bit i of user 1 at the β th

subgroup, $\Lambda_{\beta^{(i)}}^{u_1}$ is

$$\begin{aligned}
\Lambda_{\beta^{(i)}}^{u_1} &= \log \left(\frac{f(\mathbf{r}_\beta | u_{1,\beta}^{(i)} = 0)}{f(\mathbf{r}_\beta | u_{1,\beta}^{(i)} = 1)} \right) \\
&\approx \min_{\mathbf{u}_{1,\beta}: u_{1,\beta}^{(i)}=1, \mathbf{u}_{2,\beta} \in \{\mathcal{S}\}^k} \frac{\|\mathbf{r}_\beta - \mathbf{h}_{1,\beta} \odot \mathbf{u}_{1,\beta} - \mathbf{h}_{2,\beta} \odot \mathbf{u}_{2,\beta}\|^2}{\sigma^2} \\
&\quad - \min_{\mathbf{u}_{1,\beta}: u_{1,\beta}^{(i)}=0, \mathbf{u}_{2,\beta} \in \{\mathcal{S}\}^k} \frac{\|\mathbf{r}_\beta - \mathbf{h}_{1,\beta} \odot \mathbf{u}_{1,\beta} - \mathbf{h}_{2,\beta} \odot \mathbf{u}_{2,\beta}\|^2}{\sigma^2}
\end{aligned} \tag{2.7}$$

where $\mathbf{h}_{1,\beta} \in \mathbb{C}^{1 \times k}$ and $\mathbf{h}_{2,\beta} \in \mathbb{C}^{1 \times k}$ denote the channel state information (CSI) of users 1 and 2 through β th subgroup, respectively, and \odot denotes Hadamard multiplication. When the OFDM-IM waveform is decoded first, the complexity of LLR calculation, in terms of complex multiplications, becomes $\sim \mathcal{O}(c |\mathcal{S}|^m |\mathcal{S}|^k)$. On the other hand, starting the decoding process with the OFDM waveform, the LLR of the bit i of user 2 at the n th subcarrier, $\Lambda_{n^{(i)}}^{u_2}$, becomes

$$\begin{aligned}
\Lambda_{n^{(i)}}^{u_2} &= \log \left(\frac{f(r_n | u_{2,n}^{(i)} = 0)}{f(r_n | u_{2,n}^{(i)} = 1)} \right) \\
&\approx \min_{u_{2,n}: u_{2,n}^{(i)} \in \mathcal{S}_1^i, u_{1,n} \in \mathcal{S}'} \frac{\|r_n - h_{2,n} u_{2,n} - h_{1,n} u_{1,n}\|^2}{\sigma^2} \\
&\quad - \min_{u_{2,n}: u_{2,n}^{(i)} \in \mathcal{S}_0^i, u_{1,n} \in \mathcal{S}'} \frac{\|r_n - h_{2,n} u_{2,n} - h_{1,n} u_{1,n}\|^2}{\sigma^2}.
\end{aligned} \tag{2.8}$$

By decoding the OFDM waveform first, the complexity of LLR calculation, in terms of complex multiplications, becomes $\sim \mathcal{O}(|\mathcal{S}'| |\mathcal{S}|)$. The waveform, whichever is decoded first, is reconstructed and subtracted from the aggregate received signal before the next user's signal is decoded.

2.4.5 System Model for the Proposed Waveform Domain NOMA Scheme in Downlink Transmission

For brevity, consider a two users downlink NOMA scenario in Figure 2.6, where a single BS transmits the superimposed signal to both users over N subcarriers in the presence

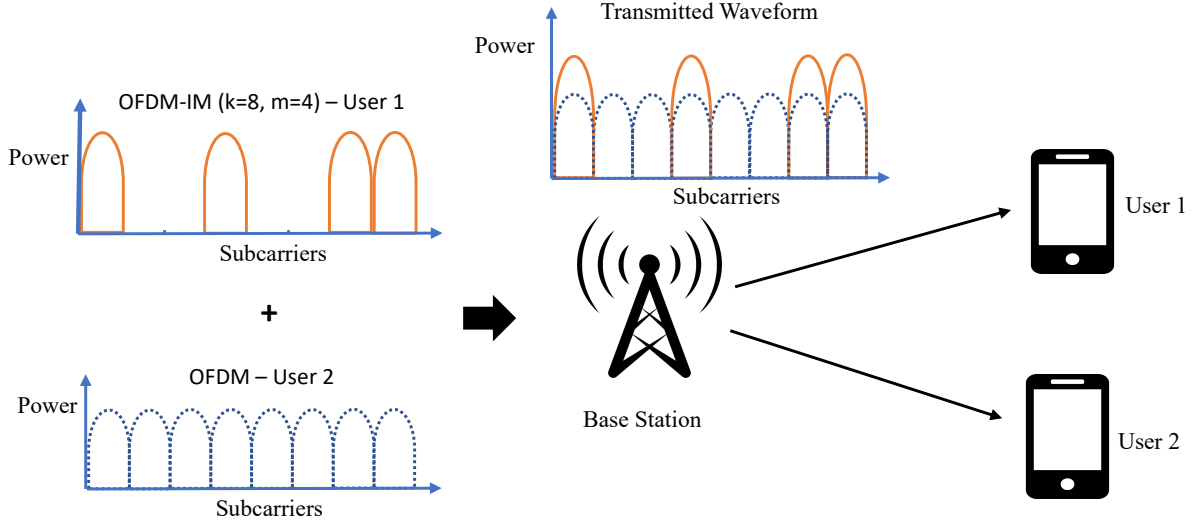


Figure 2.6: Two users downlink NOMA scheme with OFDM-IM+OFDM.

of frequency selective channels, including AWGN. It is assumed that all transceivers are equipped with a single antenna. The transceiver architecture of the proposed NOMA scheme is presented in Figure 2.7 and 2.8.

The LLR calculations are evaluated depending on the waveform type that is decoded first. It is shown that the proposed OFDM-IM and OFDM NOMA scheme outperforms the conventional power-domain NOMA scheme with OFDM waveform in terms of BLER performance in the power-balanced scenarios. Moreover, the proposed NOMA scheme provides flexibility among users regarding their demands.

2.4.5.1 OFDM Based Conventional PD-NOMA in Downlink Transmission

Firstly, BS encodes messages of UEs by LDPC codes and modulate via QAM, where data symbols of users are drawn from a complex symbol alphabet \mathcal{S} . Then, these symbols are OFDM modulated and transmitted to be received by each UE over the same RE. Moreover, $p_{1,n}$ and $p_{2,n}$ denote the signal power of user 1 and user 2 at the n th subcarrier, respectively. In the OFDM with total N subcarriers, the total powers of user 1 and user 2 become $P_1 = \sum_{n=1}^N p_{1,n}$ and $P_2 = \sum_{n=1}^N p_{2,n}$, respectively. After the process of FFT and removal of cyclic

prefix, the baseband received signal at the n th subcarrier for each UE is expressed as follows:

$$r_{1,n} = h_{1,n} (\sqrt{p_{1,n}}u_{1,n} + \sqrt{p_{2,n}}u_{2,n}) + w_n, \quad (2.9)$$

and

$$r_{2,n} = h_{2,n} (\sqrt{p_{1,n}}u_{1,n} + \sqrt{p_{2,n}}u_{2,n}) + w_n, \quad (2.10)$$

where $h_{1,n}$, $h_{2,n}$, $u_{1,n}$, and $u_{2,n}$ are the channel gains and data symbols of users 1, and 2, respectively. Also, $w_n \sim \mathcal{CN}(0, \sigma^2)$ denotes the AWGN at the n th subcarrier.

Assuming that the signal of user 1 is decoded first where user 1 has more power, the capacity of user 1 (R_1) in conventional power-domain NOMA is given by

$$R_1 = \sum_{n=1}^N \log_2 \left(1 + \frac{p_{1,n}h_{1,n}}{\sigma^2 + p_{2,n}h_{1,n}} \right) \text{ bit/s/Hz}. \quad (2.11)$$

Assuming perfect SIC, which is infeasible, the capacity of user 2 (R_2) is calculated as follows:

$$R_2 = \sum_{n=1}^N \log_2 \left(1 + \frac{p_{2,n}h_{2,n}}{\sigma^2} \right) \text{ bit/s/Hz}. \quad (2.12)$$

In the case of ML-MUD without SIC, the decoding order does not have any effect on the sum-rate; therefore, any arbitrary decoding order can be assumed to be performed [48]. On the other hand, when ML-MUD with SIC is used, the user with higher received power should be decoded first.

2.4.5.2 Proposed Waveform Domain NOMA Scheme for Downlink Transmission

As Figure 2.6 depicts, OFDM-IM waveform has been utilized for user 1, whereas OFDM waveform is used to send the signal of user 2 over N subcarriers. In the OFDM-IM scheme [49], the total $Q = Q_1 + Q_2$ bits are transmitted as follows: Firstly, N subcarriers are split into total G subblocks consisting of k subcarriers. The Q_1 bits are used to determine the indices of m active subcarriers where the total number of active subcarrier positions is denoted

as $c = Gm$. In each subblock β , only m out of k subcarriers have activated. Activated subcarriers are used to map Q_2 bits on to M -ary signal constellation symbols selected from the complex set \mathbb{S} . The information of user 1, which is carried in the subblock β , is given by $\mathbf{u}_{1,\beta} = [u_{1,\beta}^{(1)} \dots u_{1,\beta}^{(Q)}]$. Let Ω_j^β denote j th combination of the active subcarrier indices for subcarrier group β , whereas $\bar{\Omega}_j^\beta$ is the complement of it, including empty subcarriers at the β -th subgroup. As seen in Figure 2.7, the interleaved grouping is performed to increase the achievable rate of OFDM-IM [50]. In subblock β , the vector of modulated symbols of user 2 carried with OFDM waveform is denoted by $\mathbf{u}_{2,\beta} = [u_{2,\beta}^{(1)} \dots u_{2,\beta}^{(k)}]$.

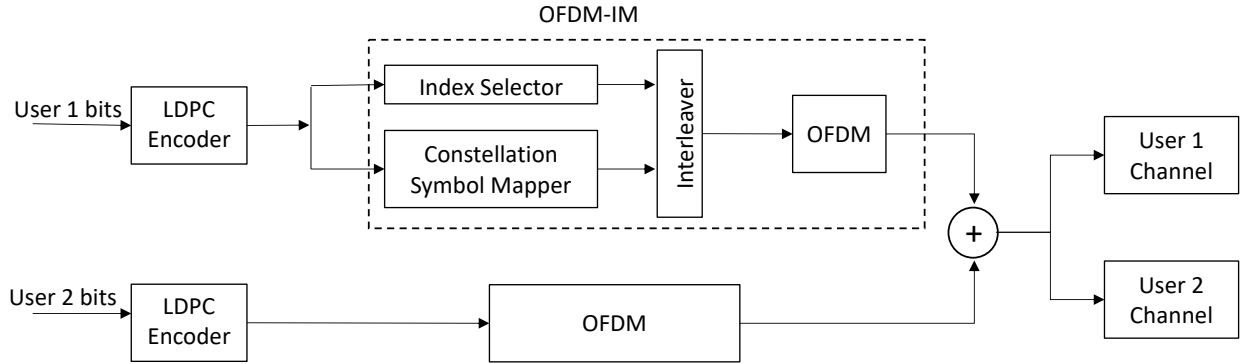


Figure 2.7: Coding and modulating of user 1 (OFDM-IM) and user 2 (OFDM) signals.

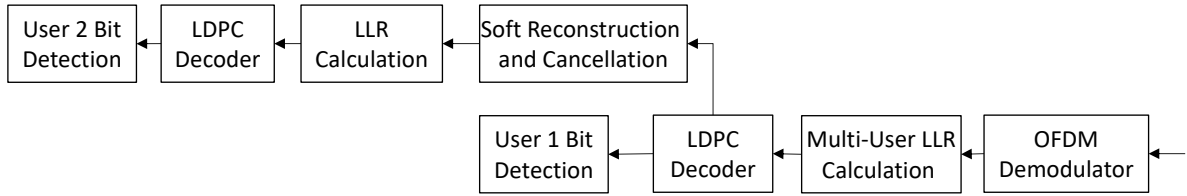


Figure 2.8: Demodulating and decoding of the superimposed received signal with LDPC codes aided soft reconstruction and cancellation.

After FFT and cyclic prefix removal, the superimposed received signal for the users at the n th subcarrier becomes

$$r_{1,n} = h_{1,n} \left(\sqrt{\frac{kp_{1,n}}{mN}} u_{1,n} + \sqrt{p_{2,n}} u_{2,n} \right) + w_{1,n}, \quad (2.13)$$

$$r_{2,n} = h_{2,n} \left(\sqrt{\frac{kp_{1,n}}{mN}} u_{1,n} + \sqrt{p_{2,n}} u_{2,n} \right) + w_{2,n}, \quad (2.14)$$

where $u_{1,n} \in \mathbb{S}' = \{0, \mathbb{S}\}$. Moreover, denote $\mathbf{r}_\beta \in \mathbb{C}^{1 \times k}$ as the received signal at the β th subgroup. Figure 2.8 depicts the reception process of the proposed NOMA scheme by decoding the OFDM-IM waveform first. However, the decoding may not always start with the OFDM-IM waveform. It depends on both power, subcarrier allocation, and modulation order. When OFDM-IM waveform is removed first, the capacity analysis of the proposed NOMA scheme can be found in [52], whereas the other order of decoding is not studied there. In this paper, capacity analysis of the scheme is evaluated when the OFDM waveform is removed first from the superimposed signal. Calculations for the capacity of users are performed on one subblock group. Assuming that the subcarriers in the subgroup are faded independently, the capacity of user 2 is written as

$$R_2 = \sum_{n \in \bar{\Omega}^\beta} \log_2 \left(1 + \frac{p_{2,n} h_{2,n}}{\sigma^2} \right) + \sum_{n \in \Omega^\beta} \log_2 \left(1 + \frac{p_{2,n} h_{2,n}}{\sigma^2 + \frac{k p_{1,n}}{mN} h_{2,n}} \right). \quad (2.15)$$

After successfully removing the OFDM signal from the superimposed signal, the capacity of user 1 with interleaved OFDM-IM waveform is lower bounded as follows [50]:

$$R_1 = \frac{m}{k} \log_2(M) + \frac{\log_2(C(k, m))}{k} - \frac{1}{C(k, m) k M^m} \times \sum_{j=1}^{C(k, m)} \sum_m \times \log_2 \left(\sum_{j'=1}^{C(k, m)} \sum_{k-m} \frac{1}{\det(\mathbf{I}_k + \mathbf{\Lambda}_{j j'})} \right), \quad (2.16)$$

where $C(k, m)$ denotes the binomial coefficient, \mathbf{I}_k is the $k \times k$ unit matrix, $\mathbf{\Lambda}_{j j'}$ is an $k \times k$ diagonal matrix whose i -th diagonal element is given as

$$[\mathbf{\Lambda}_{j j'}]_{i,i} = \begin{cases} \frac{p_1 k}{2\sigma^2 m} \left| s_{t_{\Omega_j^{-1}(i)}} - s_{t'_{\bar{\Omega}_{j'}^{-1}(i)}} \right|^2, & i \in \Omega_j \cap \Omega_{j'}, \\ \frac{p_1 k}{2\sigma^2 m} \left| s_{t_{\Omega_j^{-1}(i)}} \right|^2, & i \in \Omega_j \cap \bar{\Omega}_{j'}, \\ \frac{p_1 k}{2\sigma^2 m} \left| s_{t'_{\bar{\Omega}_{j'}^{-1}(i)}} \right|^2, & i \in \bar{\Omega}_j \cap \Omega_{j'}, \\ 0, & i \in \bar{\Omega}_j \cap \bar{\Omega}_{j'}, \end{cases} \quad (2.17)$$

where \mathbf{s} denotes the QAM modulated symbols in the activated m subcarriers, $\mathbf{s} = [s_{t_1}, \dots, s_{t_m}] \in \mathbb{S}^m$. As mentioned in [50], it should be noted that if $\Omega_j(r) = i$, then $\Omega_j^{-1}(i) = r \cdot \sum_{p(n)} = \sum_{p_1=1}^M \dots \sum_{p_n=1}^M$. To conclude, (2.16) is the lower bound of the achievable data rate with interleaved OFDM-IM waveform for user 1.

2.4.6 LLR Calculations for the Proposed Downlink Transmission

This section includes the LLR calculations of each user for two different NOMA schemes. Calculated LLRs are sent to the LDPC decoder as input. For the sake of fair comparison, we have used the log-sum approximation technique [51] to calculate approximate LLRs of two different NOMA schemes.

2.4.6.1 LLR Calculations for OFDM Based Conventional NOMA in Downlink Transmission

With ML-MUD algorithm, the LLR of the bit i of user 1 at the n th subcarrier, $\Lambda_{n^{(i)}}^{u_1}$, is calculated as

$$\begin{aligned} \Lambda_{n^{(i)}}^{u_1} &= \log \left(\frac{f(r_n | u_{1,n}^{(i)} = 0)}{f(r_n | u_{1,n}^{(i)} = 1)} \right) \\ &\approx \min_{u_{1,n}: u_{1,n}^{(i)} \in \mathbb{S}_1^i, u_{2,n} \in \mathbb{S}} \frac{\|r_n - h_{1,n}(u_{1,n} - u_{2,n})\|^2}{\sigma^2} \\ &\quad - \min_{u_{1,n}: u_{1,n}^{(i)} \in \mathbb{S}_0^i, u_{2,n} \in \mathbb{S}} \frac{\|r_n - h_{1,n}(u_{1,n} - u_{2,n})\|^2}{\sigma^2}, \end{aligned} \quad (2.18)$$

where $\mathbb{S}_b^i \subset \mathbb{S}$ denotes the set of all symbols $\alpha \in \mathbb{S}$ whose label has $b \in \{0, 1\}$ in bit position i . The complexity of this LLR calculation, in terms of complex multiplications, becomes $\sim \mathcal{O}(|\mathbb{S}|^2)$. After LDPC decoder is fed with LLRs, the symbols of user 1 is reconstructed and subtracted from the superimposed signal with inevitable SIC error. The LLRs of user 2 are calculated with the remaining signal and sent to the LDPC decoder in order to obtain bit decisions of user 2.

2.4.6.2 LLR Calculations for the Proposed Waveform Domain NOMA in Downlink Transmission

The LLR calculations for users' bits in the OFDM-IM+OFDM NOMA scheme depend on which waveform is decided to be decoded first. The total power level is not the unique limitation to decide which waveform should be decoded first. By decoding the OFDM-IM waveform first, the LLR of the bit i of user 1 at the β th subgroup, $\Lambda_{\beta^{(i)}}^{u_1}$ is

$$\begin{aligned} \Lambda_{\beta^{(i)}}^{u_1} &= \log \left(\frac{f(\mathbf{r}_\beta | u_{1,\beta}^{(i)} = 0)}{f(\mathbf{r}_\beta | u_{1,\beta}^{(i)} = 1)} \right) \\ &\approx \min_{\mathbf{u}_{1,\beta}: u_{1,\beta}^{(i)}=1, \mathbf{u}_{2,\beta} \in \{\mathcal{S}\}^k} \frac{\|\mathbf{r}_\beta - \mathbf{h}_{1,\beta} \odot (\mathbf{u}_{1,\beta} - \mathbf{u}_{2,\beta})\|^2}{\sigma^2} \\ &\quad - \min_{\mathbf{u}_{1,\beta}: u_{1,\beta}^{(i)}=0, \mathbf{u}_{2,\beta} \in \{\mathcal{S}\}^k} \frac{\|\mathbf{r}_\beta - \mathbf{h}_{1,\beta} \odot (\mathbf{u}_{1,\beta} - \mathbf{u}_{2,\beta})\|^2}{\sigma^2}, \end{aligned} \quad (2.19)$$

where $\mathbf{h}_{1,\beta} \in \mathbb{C}^{1 \times k}$ and $\mathbf{h}_{2,\beta} \in \mathbb{C}^{1 \times k}$ denote the CSI of users 1 and 2 through β th subgroup, respectively, and \odot denotes Hadamard multiplication. When the OFDM-IM waveform is decoded first, the complexity of LLR calculation, in terms of complex multiplications, becomes $\sim \mathcal{O}(c |\mathcal{S}|^m |\mathcal{S}|^k)$. On the other hand, starting the decoding process with the OFDM waveform, the LLR of the bit i of user 2 at the n th subcarrier, $\Lambda_{n^{(i)}}^{u_2}$, becomes

$$\begin{aligned} \Lambda_{n^{(i)}}^{u_2} &= \log \left(\frac{f(r_n | u_{2,n}^{(i)} = 0)}{f(r_n | u_{2,n}^{(i)} = 1)} \right) \\ &\approx \min_{u_{2,n}: u_{2,n}^{(i)} \in \mathcal{S}'_1, u_{1,n} \in \mathcal{S}'} \frac{\|r_n - h_{2,n}(u_{2,n} - u_{1,n})\|^2}{\sigma^2} \\ &\quad - \min_{u_{2,n}: u_{2,n}^{(i)} \in \mathcal{S}'_0, u_{1,n} \in \mathcal{S}'} \frac{\|r_n - h_{2,n}(u_{2,n} - u_{1,n})\|^2}{\sigma^2}. \end{aligned} \quad (2.20)$$

By decoding the OFDM waveform first, the complexity of the LLR calculation, in terms of complex multiplications, becomes $\sim \mathcal{O}(|\mathcal{S}'| |\mathcal{S}|)$. The waveform, whichever is decoded first, is reconstructed and subtracted from the aggregate received signal before the next user's signal is decoded.

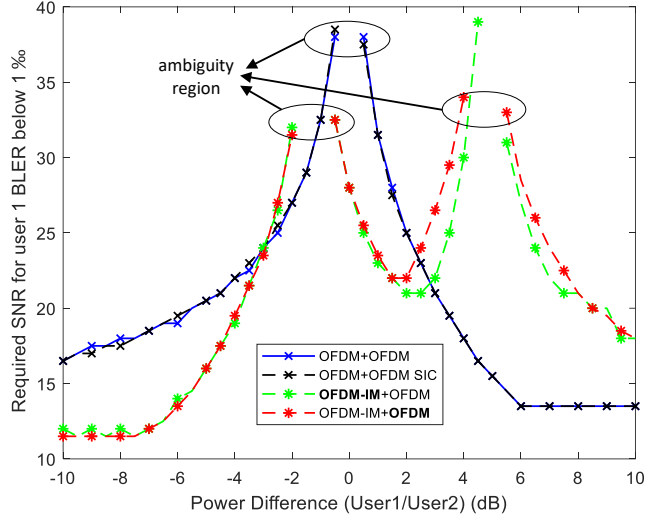


Figure 2.9: User 1 BLER for uncoded uplink NOMA schemes in AWGN.

2.4.7 Simulation Results

The proposed technique is evaluated numerically through Monte Carlo simulations for both uplink and downlink systems. As in [42], the performance of the proposed NOMA scheme is evaluated with BLER metric. Since the SIC is not perfectly performed in practice, achievable rate analysis under the perfect SIC condition misleads the comparison of the schemes. As for the modulation order, QPSK signaling is used for both NOMA schemes, where equal data rate is satisfied with three active subcarriers in groups of four subcarriers ($m = 3$, $k = 4$) for the user utilizing the OFDM-IM waveform. For OFDM+OFDM NOMA, two different decoding schemes are investigated called ML and ML-SIC. For the ML-SIC based decoding, the user with high received power is decoded first, then reconstructed, and eliminated from the superimposed signal, whereas users' bits is directly demodulated with ML algorithm in the ML based decoding. On the other hand, for OFDM-IM+OFDM NOMA, the decoding order is determined according to waveform type. Firstly decoded waveform is shown as bold for all given plots.

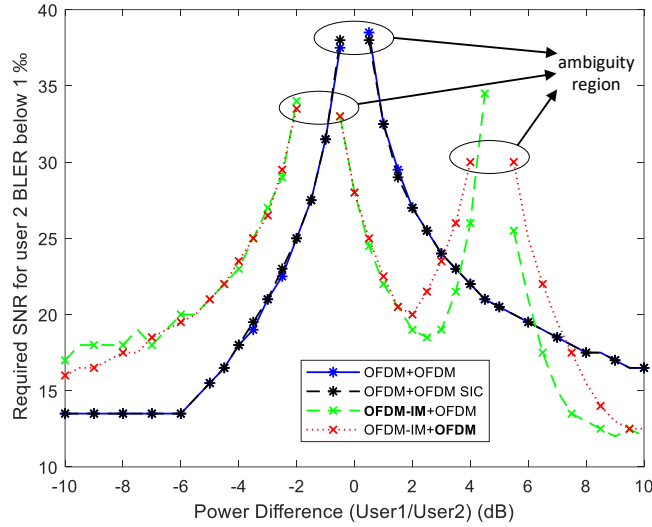


Figure 2.10: User 2 BLER for uncoded uplink NOMA schemes in AWGN.

2.4.7.1 Numerical Evaluation for Waveform Domain NOMA in Uplink System

Figure 2.9 and 2.10 demonstrate the uncoded performance of both NOMA schemes over the AWGN channel for user 1 and user 2, respectively.

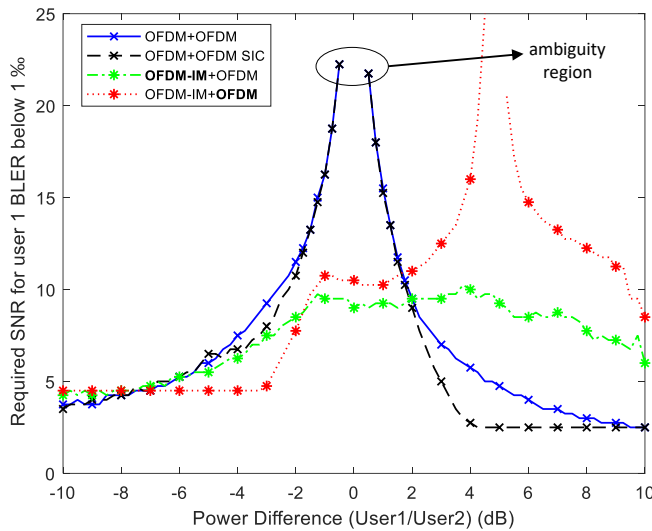


Figure 2.11: User 1 BLER for coded uplink NOMA schemes in AWGN.

The vertical axis denotes the required signal-to-noise ratio (SNR) for a user to achieve the target BLER of 1%, whereas the horizontal axis denotes the power difference in terms of dB between two different users. OFDM+OFDM NOMA performance degrades significantly

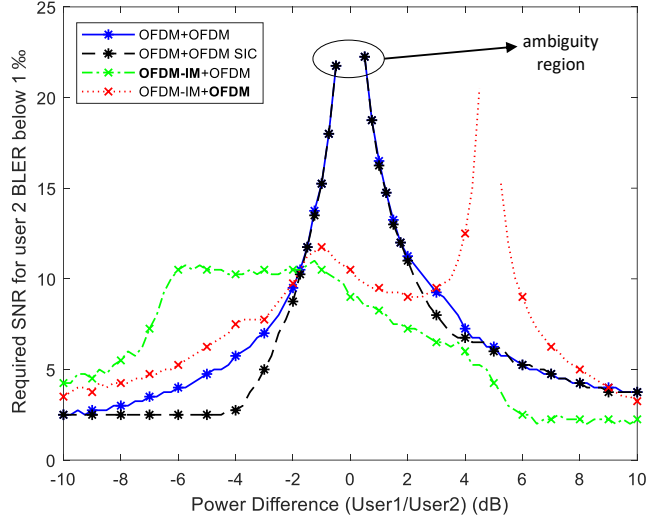


Figure 2.12: User 2 BLER for coded uplink NOMA schemes in AWGN.

when users' power is close to each other. As reference [53] shows that, OFDM-IM+OFDM NOMA is superior in terms of BLER at the region, where power difference between users is very close to 0 dB. This superiority comes from the inherent power difference of the OFDM-IM structure. However, as power imbalance between the users nears -2 dB and 5 dB, the performance degrades significantly because power coefficients $\sqrt{\frac{kP_1}{mN}}$ and $\sqrt{P_2}$ in Figure 2.5 equate the aggregate to the decision boundary. These regions are called as ambiguity region where user's messages are not decoded even with high SNR.

Figure 2.11 and 2.12 compare the LDPC coded conventional power-domain and the proposed waveform-domain NOMA with 0.5 code rate for users 1 and 2, respectively. The block length is chosen as 256.

For waveform-domain NOMA, the decoding order should be chosen properly to enhance the performance gain. As opposed to conventional power-domain NOMA, the superior region of the user 1 and user 2 is roughly below 2 dB and above -2 dB, respectively. Using forward error correction with soft reconstruction and cancellation removes deep performance losses in the range of certain power differences for OFDM-IM+OFDM NOMA scheme. However, conventional power-domain NOMA still has a region where the performance degrades significantly. The proposed waveform-domain NOMA scheme is superior at the region where

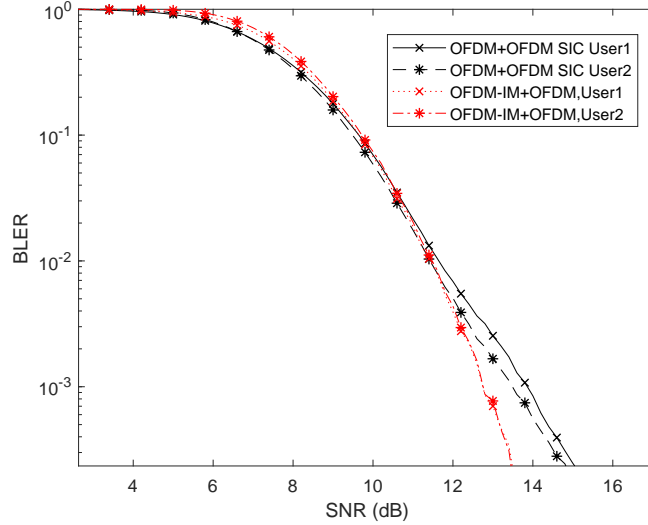


Figure 2.13: Comparison of conventional and proposed uplink NOMA schemes in frequency selective channel with tap number is 10.

the power of users is close to each other without having significant performance losses as the power difference between users increases.

Figure 2.13 depicts the BLER performance of the conventional power-domain and the proposed waveform-domain NOMA schemes through frequency selective channel with 10 taps where users modulate their signal with equal power. Throughout the simulation, it is assumed that channel knowledge is present at the receiver. Since the channel is frequency selective, the received signal has different power imbalances over each subcarrier; in other words, power equality does not hold any more at the receiver side. Even in this case, better performance is obtained with the proposed waveform-domain NOMA scheme. Nearly 1 dB gain is achieved for both users at the target BLER of 1%.

2.4.7.2 Numerical Evaluation for Waveform Domain NOMA in Downlink System

Figure 2.14 and 2.15 demonstrate the performance of conventional OFDM NOMA and proposed OFDM-IM NOMA schemes over the frequency selective channel with 10 taps for user 1 and user 2, respectively. Code rate is selected as 0.5 with 256 block length. Throughout the simulation, it is assumed that channel knowledge is present at the receiver.

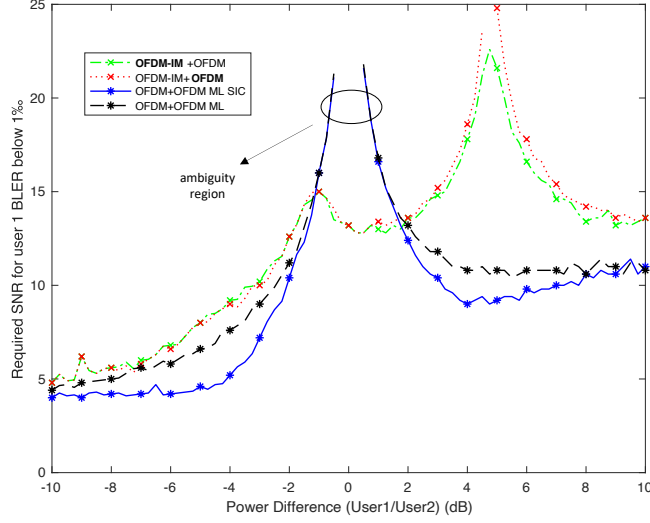


Figure 2.14: BLER of user 1 of the downlink NOMA schemes in frequency selective channel.

OFDM-IM+OFDM NOMA is superior in terms of BLER at the region, where power difference between users is very close to 0 dB. However, as power imbalance between the users is close to each other in conventional OFDM NOMA, the performance degrades significantly because power coefficients of the users equate the aggregated signal to the decision boundary. These regions are called as ambiguity region where user's messages are not decoded even with high SNR.

As opposed to conventional power-domain NOMA, the superior region of the user 1 and user 2 in the proposed scheme is roughly below 2 dB and above -2 dB, respectively. Due to inherent power imbalance in OFDM-IM, the decision of symbol is perplexed when aggregate symbol falls into decision boundary at the 5dB power imbalance. Nevertheless, ambiguity region can not be seen in the proposed scheme by decoding OFDM-IM first, it can be decoded at roughly 20 dB with the help of null subcarriers in OFDM-IM waveform. Using forward error correction with soft reconstruction and cancellation removes deep performance losses in the range of certain power differences for OFDM-IM+OFDM NOMA scheme. However, conventional power-domain NOMA still has a region where the performance degrades significantly. The proposed waveform-domain NOMA scheme is superior at the region where

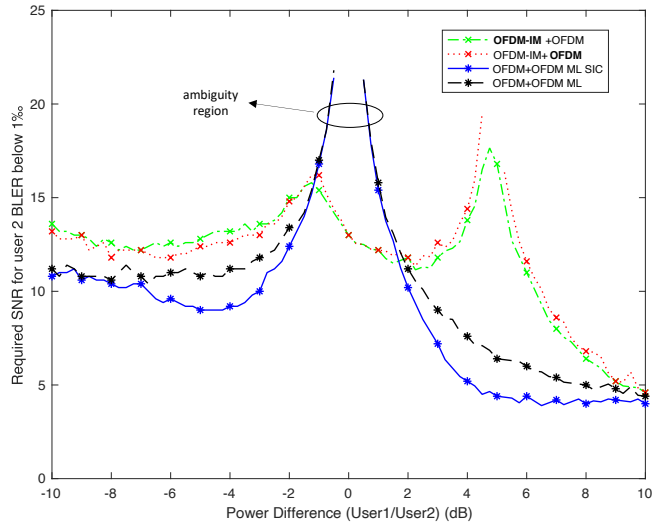


Figure 2.15: BLER of user 2 of the downlink NOMA schemes in frequency selective channel.

the power of users is close to each other without having significant performance losses as the power difference between users increases.

Chapter 3: Rate-Splitting Multiple Accessing

In this chapter² following notations are used. Lower-case bold face variables indicate vectors, and upper-case bold face variables indicate matrices, $\text{diag}(\mathbf{M})$ returns the elements on the main diagonal of matrix \mathbf{M} in a vector, $\mathcal{CN}(\mu, \sigma^2)$ represents complex Gaussian random vectors with mean μ and variance σ^2 . The ℓ_2 -norm of a vector and Frobenius norm of a matrix are denoted as $\|\cdot\|$ and $\|\mathbf{A}\|_F$, respectively. The notation m_{ij} is the value located in i th row and j th column of matrix \mathbf{M} and \mathbf{e}_i denotes the i th standard unit basis vector of for \mathbb{R}^N .

3.1 Introduction

Innovative applications like AR, holographic communication, digital replica require significant capacity and traffic growth. Dedicated multiple access schemes such as NOMA and RSMA are proposed recently to cater for these immersive needs. In single-antenna systems, e.g. SISO BC, PD-NOMA has been shown to achieve higher SE than OMA and simultaneously serves a higher number of users at an additional cost of increased complexity [20].

OFDM waveform has been widely studied and deployed in wireless communication standards such as 4G-LTE, 5G-NR and Wi-Fi due to its low-complexity implementation and robustness against frequency selective channel models [55]. However, 'sinc' shaped subcarriers of OFDM makes it vulnerable to sources of ICI such as Doppler spread, phase noise, mismatch in local oscillators of receiver and transmitter ends, etc. In fact, ICI destroys the orthogonality of subcarriers in OFDM and causes saturation in the data rate and error floor region in the BER analysis even though the overall transmit power of the system increases

²The contents of the chapter are published in [54]. Permissions are included in Appendix A.

[56]. This issue needs to be addressed in order to meet demanding requirements of next generation communication standards.

RSMA has been shown to achieve the largest upper bound for the achievable rate in the interference channel which makes it promising to address the ICI related problems of the OFDM waveform [57]. Moreover, RSMA has been shown to encapsulate and surpass the performance of SDMA, NOMA, OMA, multicasting in multiple antenna networks in terms of spectral and energy efficiency, latency, and resilience to mixed-critical quality of service [58].

Analysis of RSMA in multi-antenna multicarrier systems has been studied by several papers [59, 60, 61]. A three step resource allocation scheme is proposed in [59] where power allocation on a single subcarrier, matching between user and subcarrier and power allocation among different subcarriers are solved in steps to maximize the sum-rate. In [60], RSMA is studied in the overloaded multicarrier multi-group multicast downlink scenario by formulating a joint max-min fairness and sum-rate problem. RSMA for joint communications and jamming with a multi-carrier waveform in MISO BC is studied in [61], where optimal precoder and power allocation is investigated for simultaneous communications and jamming in cognitive radio networks.

The abovementioned works consider RSMA to address the problems of various systems employing multi-carrier waveforms, however, the problems of the waveform itself, such as ICI due to Doppler under mobility, are not addressed. In this study, we employ RSMA to solve the challenging problems that OFDM waveform faces under practical channel conditions for the first time. Owing to the flexibility granted by the use of message-splitting and SIC, we show that OFDM-RSMA outperforms orthogonal frequency division multiple access (OFDMA) and OFDM-NOMA in terms of sum-rate under frequency-selective channels and high mobility.

3.2 System Model

We consider a system model, where a transmitter with a single antenna serves K single-antenna users. The transmitter uses OFDM to serve users in the same time slot. As shown in Figure 3.1, 3.2, and 3.3 for a two-user case, three different multiple accessing (MA) schemes are considered for transmission *i.e.*, OFDMA, OFDM-NOMA and OFDM-RSMA.

3.2.1 OFDM Transmission for K Users

Let \mathbf{x}_k denote the time domain signal of the k -th user expressed as follows:

$$\mathbf{x}_k = \mathbf{A}\mathbf{F}^H \text{diag}(\mathbf{p}_k) \mathbf{d}_k, \quad k \in \mathcal{K} = \{1, 2, \dots, K\}, \quad (3.1)$$

where $\mathbf{F} \in \mathbb{C}^{N \times N}$ is the N -point FFT matrix, \mathbf{d}_k is the data symbols carrying information of k -th user, and $\mathbf{p}_k \in \mathbb{C}^{N \times 1}$ is the precoding vector that captures the power allocated to OFDM subcarriers. The CP-addition matrix $\mathbf{A} \in \mathbb{N}^{(N+C) \times N}$, and the CP-removal matrix $\mathbf{B} \in \mathbb{N}^{N \times (N+C)}$ can be expressed as follows:

$$\mathbf{A} = \begin{bmatrix} \mathbf{0}_{C \times (N-C)} & \mathbf{I}_C \\ & \mathbf{I}_N \end{bmatrix}, \quad \mathbf{B} = \begin{bmatrix} \mathbf{0}_{N \times C} & \mathbf{I}_N \end{bmatrix}. \quad (3.2)$$

The time-domain signal $\mathbf{y}_k \in \mathbb{C}^{(N+C) \times 1}$ received through the k -th user channel \mathbf{H}_k can be written as follows:

$$\mathbf{y}_k = \mathbf{H}_k \sum_{k=1}^K \mathbf{x}_k + \mathbf{n}_k, \quad (3.3)$$

where the vector $\mathbf{n}_k \in \mathbb{C}^{(N+C) \times 1}$ is the AWGN with $n_{k,i} \sim \mathcal{CN}(0, \sigma^2)$ where $n_{k,i} \in \mathbf{n}_k$ and σ^2 is the power of AWGN.

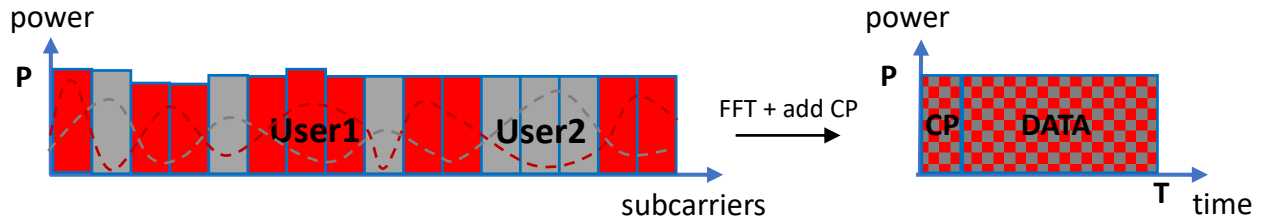


Figure 3.1: Conventional OFDMA with two users showing channel power of users (dashed line) and power allocation (solid box).

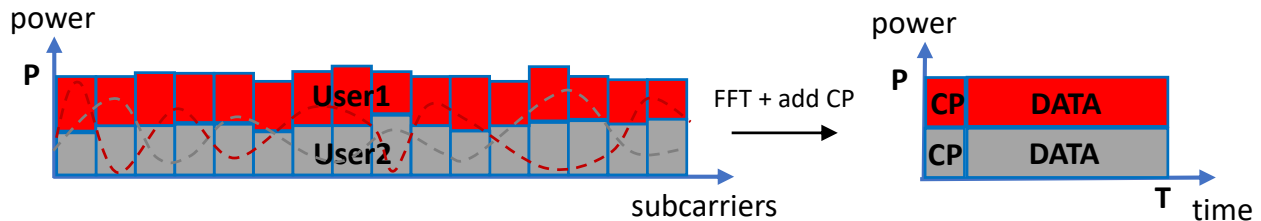


Figure 3.2: OFDM-NOMA with two users showing channel power of users (dashed line) and power allocation (solid box).

3.2.2 Channel Model

The linear time-varying (LTV) channel model includes multipath propagation and Doppler effect leading to time and frequency shifts on the transmitted signal. The channel model includes complex channel gain, Doppler shift and delay for every path. Therefore, the LTV channel in the time-delay domain, $c(t, \tau)$, can be modeled as follows [62]:

$$c(t, \tau) = \sum_{l=1}^L \alpha_l e^{j2\pi\nu_l t} \delta(\tau - \tau_l), \quad (3.4)$$

where α_l , τ_l , and ν_l denote the complex attenuation factor, time delay, and Doppler frequency shift associated with the l^{th} discrete propagation path where $l \in \{1, 2, \dots, L\}$. Let N and C be the total subcarrier number with the set of $\mathcal{N} = \{1, 2, \dots, N\}$ and CP length of the OFDM waveform, respectively. It is assumed that CP length is larger than the maximum delay spread to ensure ISI free transmission. The relation of (3.4) with the k -th user's time

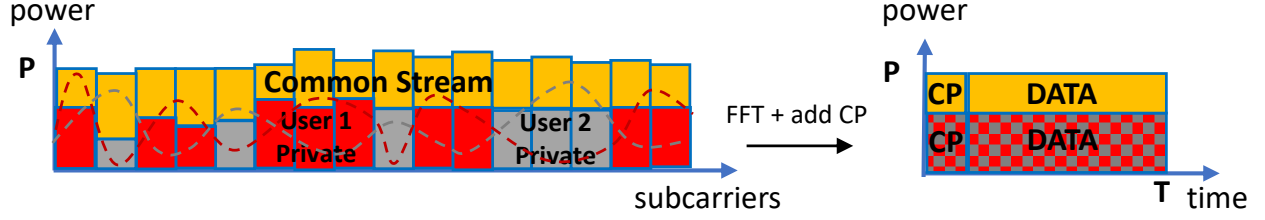


Figure 3.3: OFDM-RSMA with two users showing channel power of users (dashed line) and power allocation (solid box).

domain channel matrix $\mathbf{H}_k \in \mathbb{C}^{(N+C) \times (N+C)}$ can be represented as follows:

$$\mathbf{H}_k = \sum_{l=1}^L \alpha_l \mathbf{\Pi}^{n_{\tau_l}} \mathbf{\Delta}(\nu_l), \quad (3.5)$$

where the delay matrix $\mathbf{\Pi}^{n_{\tau_l}} \in \mathbb{C}^{(N+C) \times (N+C)}$ is the forward cyclic shifted permutation matrix according to the delay of the l th path. The Doppler shift matrix for the l th path, $\mathbf{\Delta}(\nu_l) \in \mathbb{C}^{(N+C) \times (N+C)}$, is defined as $\mathbf{\Delta}(\nu_l) = \text{diag} \left(\left[e^{\frac{j2\pi\nu_l}{F_s}}, e^{\frac{j2\pi\nu_l 2}{F_s}}, \dots, e^{\frac{j2\pi\nu_l(N+C)}{F_s}} \right] \right)$, where F_s is the sampling frequency in the system model.

3.3 Proposed OFDM-RSMA Scheme

In this section, we describe the proposed OFDM-RSMA scheme and formulate a sum-rate maximization problem to obtain the optimal common rate, subcarrier, and power allocation for the proposed scheme. Fig. 3.4 demonstrates proposed scheme for a two-user scenario. At the transmitter, the message intended for user- k , W_k , is split into common and private parts, which are denoted as $W_{c,k}$ and $W_{p,k}$, $\forall k \in \mathcal{K}$. The common parts of messages for all users are combined into a single common message W_c . The common and private messages are independently encoded into the common and private streams, \mathbf{d}_c and \mathbf{d}_k , $\forall k \in \mathcal{K}$, respectively. The encoded symbols \mathbf{d}_c and \mathbf{d}_k are chosen from a Gaussian alphabet for theoretical analysis. We assume that the streams have unit power, i.e., $\mathbb{E}\{\tilde{\mathbf{d}}\tilde{\mathbf{d}}^H\} = \mathbf{I}$, where $\tilde{\mathbf{d}} = [\mathbf{d}_c^T, \mathbf{d}_1^T, \dots, \mathbf{d}_K^T]^T$.

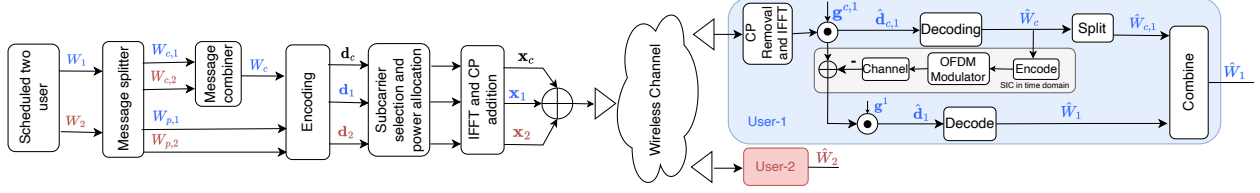


Figure 3.4: Proposed OFDM-RSMA scheme.

For a K -user OFDM-RSMA system, the transmitted common stream $\mathbf{x}_c \in \mathbb{C}^{(N+C) \times 1}$, is expressed as follows:

$$\mathbf{x}_c = \mathbf{A}\mathbf{F}^H \text{diag}(\mathbf{p}_c) \mathbf{d}_c, \quad (3.6)$$

where $\mathbf{p}_c \in \mathbb{C}^{N \times 1}$ is the power allocation precoding vector for the common stream over the OFDM subcarriers. The private stream for user- k , $\mathbf{x}_k \in \mathbb{C}^{(N+C) \times 1}$, is expressed as in (3.1). The matrix $\mathbf{P} = [\mathbf{p}_1, \dots, \mathbf{p}_K]$ is defined as the collection of all precoding vectors of private streams, $\mathbf{p}_k, \forall k \in \mathcal{K}$. Vectors $\bar{\mathbf{p}}_{k,n}$ and $\bar{\mathbf{p}}_{c,n}$ denote that n -th subcarrier is forced not to carry any energy for private and common streams, i.e., $\bar{\mathbf{p}}_{k,n} = [p_{k,1}, \dots, p_{k,n-1}, 0, p_{k,n+1}, \dots, p_{k,N}]$ and $\bar{\mathbf{p}}_{c,n} = [p_{c,1}, \dots, p_{c,n-1}, 0, p_{c,n+1}, \dots, p_{c,N}]$. Accordingly, the time-domain received signal (3.3) can be re-written as follows:

$$\mathbf{y}_k = \mathbf{H}_k \left(\mathbf{x}_c + \sum_{k=1}^K \mathbf{x}_k \right) + \mathbf{n}_k. \quad (3.7)$$

At the receiver side, we first process the common stream. CP removal matrix and FFT operation are applied to the superimposed signal \mathbf{y}_k to convert it into frequency domain for equalization and demodulation of the common stream. The received frequency domain signal at user- k , $\mathbf{r}_{c,k}$ is expressed as follows:

$$\mathbf{r}_{c,k} = \mathbf{F}\mathbf{B}\mathbf{y}_k. \quad (3.8)$$

The average received power at the n -th subcarrier of $\mathbf{r}_{c,k}$, $T_{c,k,n} \triangleq \mathbf{E} \{ |(\mathbf{r}_{c,k})_n|^2 \}$, is written as:

$$T_{c,k,n} = |s_{n,n}^{c,k,n}|^2 + \underbrace{\sum_{j=1}^N |\bar{s}_{n,j}^{c,k,n}|^2 + \sum_{u=1}^K \sum_{j=1}^N |s_{n,j}^u|^2}_{I_{c,k,n}} + \sigma^2, \quad (3.9)$$

with

$$\mathbf{S}^{c,k,n} = \mathbf{FBH}_k \mathbf{A} \mathbf{F}^H \text{diag} (p_{c,n} \mathbf{e}_n), \quad \forall k \in \mathcal{K}, \quad \forall n \in \mathcal{N}, \quad (3.10a)$$

$$\bar{\mathbf{S}}^{c,k,n} = \mathbf{FBH}_k \mathbf{A} \mathbf{F}^H \text{diag} (\bar{\mathbf{p}}_{c,n}), \quad \forall k \in \mathcal{K}, \quad \forall n \in \mathcal{N}, \quad (3.10b)$$

$$\mathbf{S}^u = \mathbf{FBH}_k \mathbf{A} \mathbf{F}^H \text{diag} (\mathbf{p}_u), \quad \forall u \in \mathcal{K}, \quad (3.10c)$$

where the matrix in (3.10a) denotes the energy leaking from the n -th subcarrier of the common stream to the other OFDM subcarriers after passing through the LTV channel. The ICI on the n -th subcarrier caused by the energy leakage from the common stream on all subcarriers except the n -th subcarrier is written in (3.10b). Lastly, interference due to all private streams is expressed in (3.10c). After the common stream is demodulated at user- k , it is reconstructed and subtracted from the received signal. Then, FFT matrix succeeding CP removal matrix is applied to the remaining signal in order to demodulate the intended private stream for user- k as follows:

$$\begin{aligned} \mathbf{r}_k &= \mathbf{FB} (\mathbf{y}_k - \mathbf{H}_k \mathbf{A} \mathbf{F}^H \text{diag} (\mathbf{p}_c) \mathbf{d}_c) \\ &= \mathbf{FB} \left(\mathbf{H}_k \sum_{k=1}^K \mathbf{x}_k + \mathbf{n}_k \right), \end{aligned} \quad (3.11)$$

The average received power at the n -th subcarrier of \mathbf{r}_k , $T_{k,n} \triangleq \mathbb{E} \left\{ |(\mathbf{r}_k)_n|^2 \right\}$, can be written as:

$$T_{k,n} = |v_{n,n}^{k,n}|^2 + \underbrace{\sum_{j=1}^N |\tilde{v}_{n,j}^{k,n}|^2 + \sum_{\substack{i=1 \\ i \neq k}}^K \sum_{j=1}^N |w_{n,j}^i|^2}_{I_{k,n}} + \sigma^2, \quad (3.12)$$

with

$$\mathbf{V}^{k,n} = \mathbf{FBH}_k \mathbf{AF}^H \text{diag}(p_{k,n} \mathbf{e}_n), \quad \forall k \in \mathcal{K}, \quad \forall n \in \mathcal{N}, \quad (3.13a)$$

$$\tilde{\mathbf{V}}^{k,n} = \mathbf{FBH}_k \mathbf{AF}^H \text{diag}(\bar{\mathbf{p}}_{k,n}), \quad \forall k \in \mathcal{K}, \quad \forall n \in \mathcal{N}, \quad (3.13b)$$

$$\mathbf{W}^i = \mathbf{FBH}_k \mathbf{AF}^H \text{diag}(\mathbf{p}_i), \quad \forall i \in \mathcal{K} \setminus k, \quad (3.13c)$$

where (3.13a) denotes the energy of the n -th subcarrier of the private stream of user- k spread over all subcarriers due to channel effects. The expressions (3.13b) and (3.13c) denote the ICI and MUI due to the private stream of user- k and other users' private streams, respectively. By using (3.9) and (3.12), SINRs of the common and private streams for a given channel state can be stated as follows:

$$\gamma_{c,k,n} \triangleq |s_{n,n}^{c,k,n}|^2 I_{c,k,n}^{-1} \quad \text{and} \quad \gamma_{k,n} \triangleq |v_{n,n}^{k,n}|^2 I_{k,n}^{-1}. \quad (3.14)$$

The achievable rates for common stream and private streams corresponding to user- k in the corresponding subcarriers can be written as follows:

$$R_{c,k,n} = \log_2(1 + \gamma_{c,k,n}) \quad \text{and} \quad R_{k,n} = \log_2(1 + \gamma_{k,n}), \quad (3.15)$$

and the achievable rates for an OFDM symbol can be written as follows:

$$R_{c,k} = \sum_{n=1}^N R_{c,k,n} \text{ bit/s/Hz} \quad \text{and} \quad R_k = \sum_{n=1}^N R_{k,n} \text{ bit/s/Hz}. \quad (3.16)$$

The sum-rate maximization problem for the proposed OFDM-RSMA can be formulated as follows:

$$\begin{aligned}
& \max_{\mathbf{R}_c, \mathbf{p}_c, \mathbf{P}} && \sum_{n=1}^N R_{c,k,n} + \sum_{k=1}^K \sum_{n=1}^N R_{k,n} \\
& \text{s.t.} && \sum_{n=1}^N R_{c,k,n} \geq \sum_{n=1}^N R_{c,n}, \\
& && R_k + C_k \geq R_k^{\min} \\
& && \|\mathbf{P}\|_F^2 + \|\mathbf{p}_c\|^2 \leq P_t,
\end{aligned} \tag{3.17}$$

where the common rate at the n th subcarrier $R_{c,n}$ is shared among users such that $C_{k,n}$ is the k -th user's portion of the common rate with $R_{c,n} = \sum_{k=1}^K C_{k,n}$, and R_k^{\min} is the minimum data rate constraint for the k -th user. The weighted minimum mean-square error (WMMSE) based precoding optimization framework studied in [63] is adopted to solve the optimization problem (3.17).

3.4 OFDM-NOMA Transmission

In a K -user OFDM-NOMA system, k -th user message is decoded after $k - 1$ users' signals are successively canceled. SIC order is not alternated at subcarrier level but kept fixed throughout one OFDM symbol as done in practical systems. The received frequency domain signal at the k -th user, \mathbf{r}_k in (3.11), is modified as follows:

$$\mathbf{r}_k = \mathbf{FB} \left(\mathbf{y}_k - \mathbf{H}_k \mathbf{A} \mathbf{F}^H \left(\sum_{l=1}^{k-1} \text{diag}(\mathbf{p}_l) \mathbf{d}_l \right) \right). \tag{3.18}$$

The received power, $T_{k,n} \triangleq \mathbb{E} \left\{ |(\mathbf{r}_k)_n|^2 \right\}$, at the n th subcarrier of \mathbf{r}_k can be written as follows:

$$T_{k,n} = |v_{n,n}^{k,n}|^2 + \underbrace{\sum_{j=1}^N |\bar{v}_{n,j}^{k,n}|^2 + \sum_{i=k+1}^K \sum_{j=1}^N |w_{n,j}^i|^2}_{I_{k,n}} + \sigma^2, \tag{3.19}$$

where

$$\begin{aligned}\mathbf{V}^{k,n} &= \mathbf{FBH}_k \mathbf{A} \mathbf{F}^H \text{diag}(\rho_{k,n} \mathbf{e}_n), \quad \forall k \in \mathcal{K}, \forall n \in \mathcal{N}, \\ \bar{\mathbf{V}}^{k,n} &= \mathbf{FBH}_k \mathbf{A} \mathbf{F}^H \text{diag}(\bar{\rho}_{k,n}), \quad \forall k \in \mathcal{K}, \forall n \in \mathcal{N}, \\ \mathbf{W}^i &= \mathbf{FBH}_k \mathbf{A} \mathbf{F}^H \text{diag}(\mathbf{p}_i), \quad \forall i \in \{k+1, \dots, K\}.\end{aligned}$$

Then, the optimization problem for achievable rate maximization using OFDM-NOMA is formulated as follows:

$$\begin{aligned}\max_{\mathbf{P}} \quad & \sum_{k=1}^K \sum_{n=1}^N R_{k,n} \\ \text{s.t.} \quad & \|\mathbf{P}\|_F^2 \leq P_t, \\ & R_k \geq R_k^{\min},\end{aligned}\tag{3.20}$$

where the matrix $\mathbf{P} = [\mathbf{p}_1, \dots, \mathbf{p}_K]$ is defined as the collection of all users' precoding vector, $\mathbf{p}_k, \forall k \in \mathcal{K}$. The formulated problem can be solved using the WMMSE-based approach as described in the previous section.

3.5 Simulation Results

In this section, we demonstrate the performance gain of the proposed OFDM-RSMA scheme over OFDMA and OFDM-NOMA under different channel conditions including flat fading, frequency and time selectivity. For simplicity, we study the scenarios where $K = 2$. For OFDM-NOMA, it is assumed that user-1 is the weak user having a smaller overall channel gain than user-2 (strong user), so that, the signal of user-1 is decoded first in the SIC process [64]. Throughout the simulations, the OFDM waveform has 35 subcarriers with a sub-carrier spacing (SCS) of 60 kHz.

Fig. 3.5 illustrates the performance of the considered MA schemes under flat-fading channel without Doppler. Here, the sum-rate performance of the proposed OFDM-RSMA method is compared to OFDM with a single user utilizing the whole bandwidth, OFDMA with two

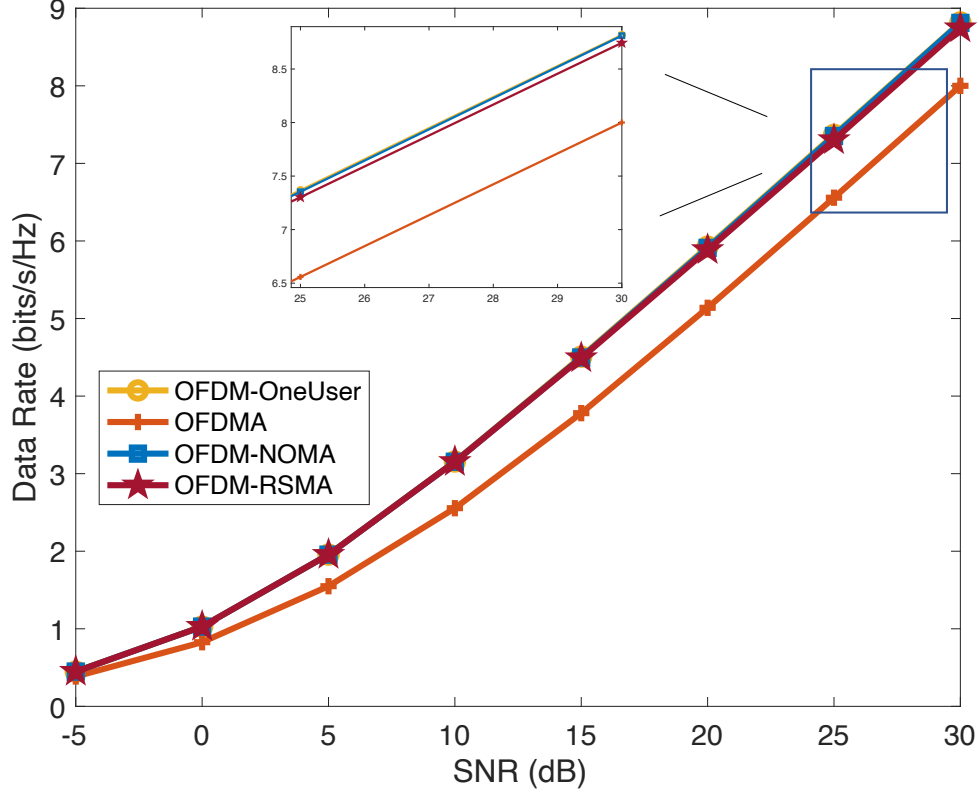


Figure 3.5: Performance comparison of OFDMA, OFDM-NOMA, OFDM-RSMA and one user OFDM under flat fading channel.

users where the whole bandwidth is divided into two equal parts, and OFDM-NOMA. Since flat fading channel with OFDM waveform can be seen as single pipeline SISO-BC scenario, maximizing the sum-rate in OFDM-NOMA and OFDM-RSMA results in allocating power to the strongest user, and hence, performing single user OFDM [65]. The gain of OFDM-RSMA and OFDM-NOMA over OFDMA emanates from the bandwidth division among users, which makes OFDMA a suboptimal transmission strategy from information-theoretic perspective [9].

Figure 3.6 demonstrates the sum-rate performance of OFDMA, OFDM-NOMA, and OFDM-RSMA under the both frequency selective and doubly dispersive channels with varying $\Delta d = \frac{f_d}{\Delta f}$, where f_d is the maximum Doppler spread and Δf is the subcarrier spacing. When $\Delta d = 0$, the channel becomes a frequency selective channel without Doppler, and the proposed OFDM-RSMA scheme provides more than 5% sum-rate gain compared to the

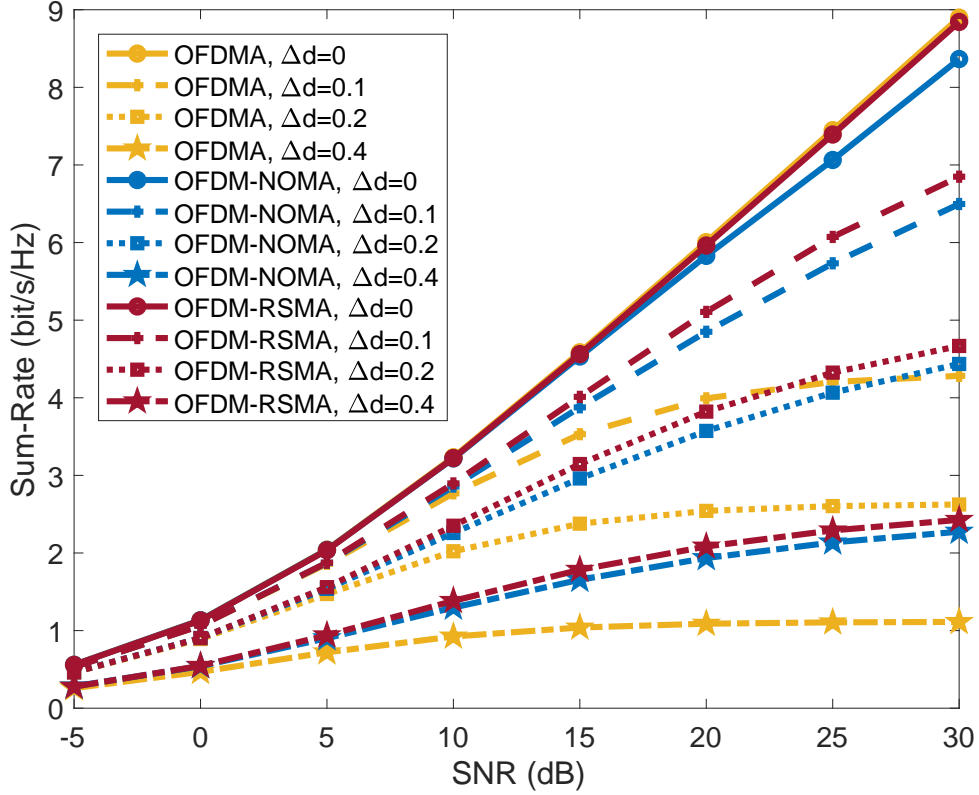


Figure 3.6: Sum-rate comparison of OFDMA, OFDM-NOMA, and OFDM-RSMA under the frequency selective and doubly selective channels.

OFDM-NOMA. Such a gain is achieved owing to the message-splitting and the deterministic decoding order in SIC for OFDM-RSMA, enabling it to overcome the power variations over subcarriers as opposed to OFDM-NOMA, which requires switching decoding order at each subcarrier for optimal performance.

Furthermore, OFDM-RSMA achieves the same performance as waterfilling-based orthogonal frequency division multiple accessing (OFDMA), which is known to be capacity achieving in frequency selective channels without Doppler [66]. As ICI increases in doubly selective channels, the sum-rate of OFDMA drops sharply and saturates at the high SNR regime when interference becomes more dominant than the noise level. It can be seen that OFDM-RSMA and OFDM-NOMA achieve higher data rate than OFDMA in this case due to the SIC process. At high SNR regime, the proposed OFDM-RSMA achieves a higher sum-rate due to its performance gain under frequency selectivity compared to OFDM-NOMA. One can also

conclude that the gain over OFDM-NOMA depends on the total subcarrier number in an OFDM symbol, and the maximum Delay spread of the channel.

In this study, we consider RSMA to address the problems of OFDM waveform under LTV channels. The proposed OFDM-RSMA scheme is robust against ICI stemming from time variations and outperforms OFDMA. Additionally, it is shown that inefficient use of SIC in the OFDM-NOMA scheme limits the exploitation of power variation over subcarriers, a problem which OFDM-RSMA tackles owing to its message-splitting framework. The results show that OFDM-RSMA can provide robustness against performance-limiting challenges of wireless propagation channel, such as, ISI, MUI, ICI, and inter-numerology interference (INI).

Chapter 4: Dual-Functional Radar and Communication Systems

This chapter³ initially explains the concept of dual-functional radar and communication systems. Later, it introduces the two different proposed waveform concept that allows simultaneous functionality for radar-sensing and communication.

Future 6G and beyond wireless systems are evolving rapidly in terms of flexibility, interoperability, and co-existence of various wireless technologies. Due to the invaluable and scarce bandwidth, as researchers explore techniques to make efficient use of strict resources; different applications, systems, and waveforms are envisioned to co-exist and operate together in harmony. On account of radar, wireless sensing and communication being eminently common and important radio frequency (RF) applications, the marriage of these concepts has recently attracted substantial attention. In the literature, radar-sensing and communication marriage has been given numerous names such as radar-communication co-existence (RCC), dual-functional radar-communication (DFRC), [69]. In the first category, two systems share the same habitat (cohabitation) and they operate with efficient interference management techniques cooperation. The second category can be seen as codesign of a system having both radar and communication capabilities. Design approach of a DFRC system can be divided into three subgroups which are joint radar-communication (JRC), joint communication-radar (JCR) [70], and unified architecture. JRC mainly focuses on the radar capability and performs communication as a secondary functionality. On the other hand, JCR refers to the systems whose essential design parameter is the communication capability of a DFRC system. Last but not the least, a unified architecture proposes a co-design system that is designed for the application requirements from the scratch.

³Second section of this chapter is published in [67] and [7], whereas third section is published in [68]. Permissions are included in Appendix A.

4.1 Need for Integration of Radar-Sensing and Communication

With rapid developments in hardware such as large antenna arrays for millimeter wave (mmWave) and THz frequencies, efficient amplifiers, and ultra-capable digital signal processing (DSP) chips; and software regarding algorithms for detection and estimation capabilities, radar and communication systems tend to intersect in order to provide efficient usage of radio resources. Combining these two different worlds to work in harmony will pave the way for new techniques in wireless technologies that may enable lots of promising applications in wireless technologies to emerge [69]. For autonomous wireless networks, the capability to sense dynamically changing states of the environment and exchange information among various nodes needs to be integrated into 6G and beyond wireless systems [71]. Also, radar-sensing is seen as an enabling technology for environment-aware communication in 6G [3]. Therefore, this trend encourages both industry and academia to plan and use the available radio resources efficiently. For example, the WLAN sensing group is organized under the IEEE 802.11 study group [72], where techniques to utilize the existing Wi-Fi frame as a sensing node are being developed regarding the future use cases of the concept. As a result, these concerns have created the joint radar-sensing and communication concept, which has gained a significant amount of attention from both industry and academia [73]. So far, most of the papers investigate the optimal waveform to function jointly for both radar-sensing and communication, which is called joint radar and communication (JRC) waveform [74]. The aim is to combine radar-sensing and communication into a single mmWave system that utilizes a standard waveform. This kind of system is aimed to be optimized regarding cost, size, power consumption, spectrum usage, and adoption of communication-capable vehicles, for example, in case of autonomous driving, which needs both radar and vehicle-to-vehicle (V2V) communication [75].

4.2 NOMA-based Joint Sensing and Communication

Joint radar-sensing and communication can be actualized using different approaches such as frequency-sharing, time-sharing and signal-sharing [76]. Time and frequency sharing approaches can be regarded as resource scheduling in wireless systems. Scheduling techniques make efficient use of hardware, but limit the spectral efficiency. On the other hand, the main aim of the signal-sharing approach is to have one waveform performing both functions, i.e, data embedded radar waveform or communication waveform with radar capabilities including multi or single carrier systems [77]. The use of waveform-domain NOMA scheme superimposing frequency modulated continuous wave (FMCW) and OFDM waveforms to support joint radar-sensing and communication is firstly proposed by authors in [67]. Here, the superiority of the proposed NOMA scheme over the conventional OFDM scheme for JRC [78] is demonstrated. The proposed architecture separately performs radar-sensing and communication functions using the same radio resources non-orthogonally and leverages the information obtained from radar process to the communication functionality.

4.2.1 System Model

The V2V scenario is considered as shown in Figure 4.1, however, the proposed scheme is also applicable for different use cases needing both radar-sensing and communication activity. For example, more complicated wireless network system is shown in Figure 4.2, including several nodes that function both radar-sensing and communication. The general transmission and reception scheme can be seen in Figure 4.3 where radar-sensing knowledge obtained from FMCW is leveraged to perform the channel estimation process in OFDM waveform.

4.2.2 Transmission Design

The FMCW waveform consisting of many chirps and the OFDM waveform are utilized for radar-sensing and communication operations, respectively. The complex equivalent time-domain representation of one chirp, whose frequency increases linearly across a total band-

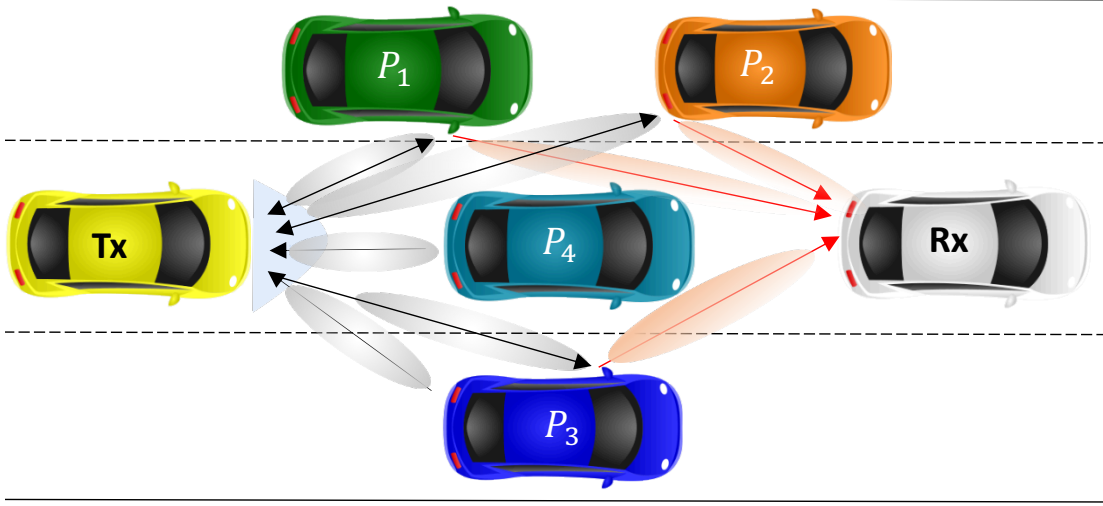


Figure 4.1: Vehicular to vehicular (V2V) system model needing both radar-sensing and communication functionality.

width of β Hz during the τ -second is expressed as [79]

$$s_{\text{chirp}}(t) = e^{j\pi\beta t^2/\tau}, \quad 0 \leq t \leq \tau. \quad (4.1)$$

The FMCW waveform consisting of K chirps per frame is

$$s_{\text{FMCW}}(t) = \sqrt{P_{\text{FMCW}}} \sum_{k=0}^{K-1} s_{\text{chirp}}(t - k\tau), \quad 0 \leq t \leq T, \quad (4.2)$$

where T and P_{FMCW} denote the total frame duration and power of the FMCW waveform, respectively.

Let $\{d_n\}_{n=0}^{N-1}$ be the complex symbols modulated via QAM drawn from a complex symbol alphabet \mathbb{S} . An OFDM symbol with N subcarriers is expressed in the time-domain as follows:

$$s_{\text{OFDM}}(t) = \sqrt{P_{\text{ofdm}}} \sum_{n=0}^{N-1} d_n e^{j2\pi n\Delta f t}, \quad 0 \leq t \leq T_s, \quad (4.3)$$

where T_s , Δf and P_{OFDM} denote one OFDM symbol duration, the subcarrier spacing and the OFDM power, respectively.

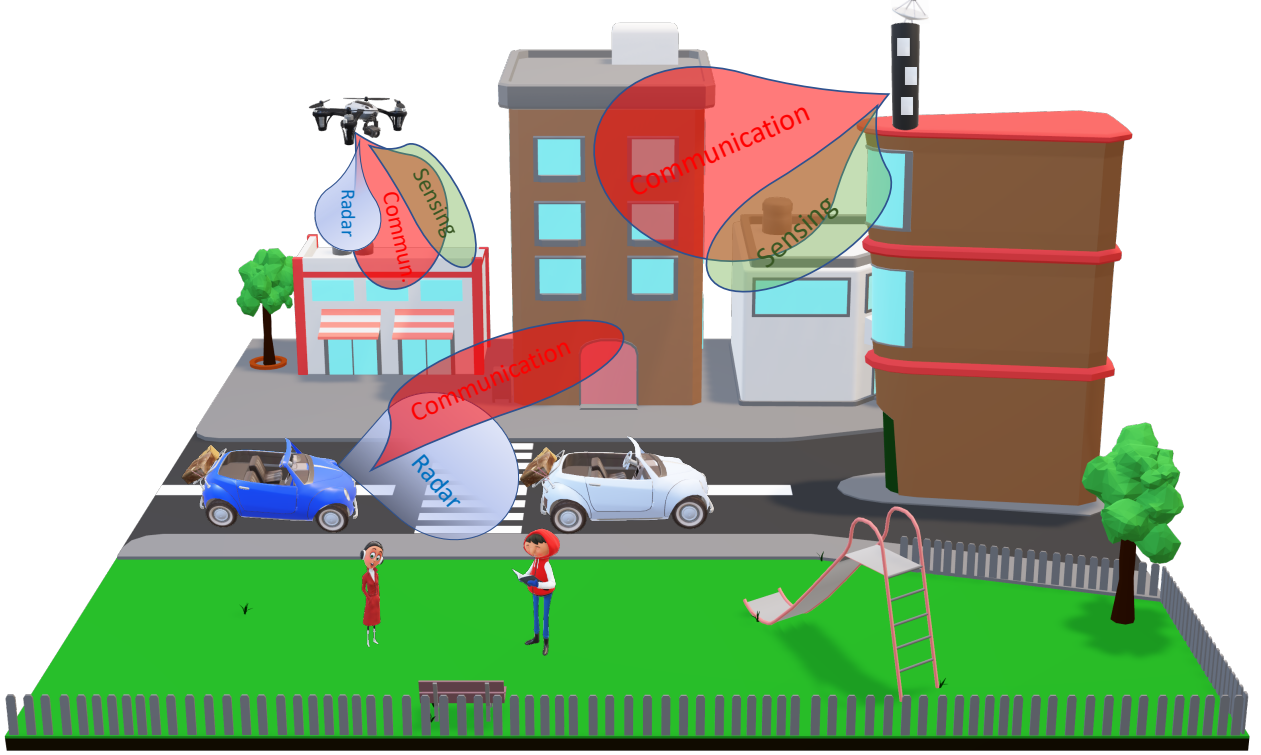


Figure 4.2: Generalized framework for joint radar-sensing and communication.

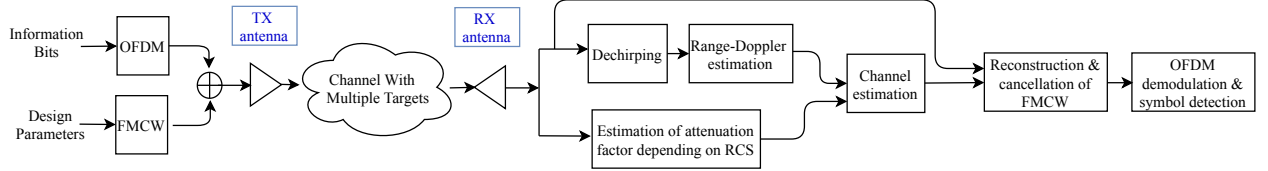


Figure 4.3: Transmission and reception operations of the proposed NOMA scheme for joint radar-sensing and communication.

A CP of length T_g is prepended to each OFDM symbol to keep OFDM subcarriers orthogonal by preventing ISI across OFDM symbols. The CP transforms the linear convolution of the multipath channel to a circular convolution, where one-tap equalization can be used [80]. After the CP addition, the m th OFDM symbol can be expressed as follows:

$$\bar{s}_m(t) = \begin{cases} s_{\text{OFDM}}(t + T_s - T_g), & \text{if } 0 \leq t \leq T_g, \\ s_{\text{OFDM}}(t - T_g), & \text{if } T_g < t \leq T_{\text{OFDM}}, \end{cases} \quad (4.4)$$

where $T_{\text{OFDM}} = T_g + T_s$ is the duration of one OFDM symbol after CP addition. Having

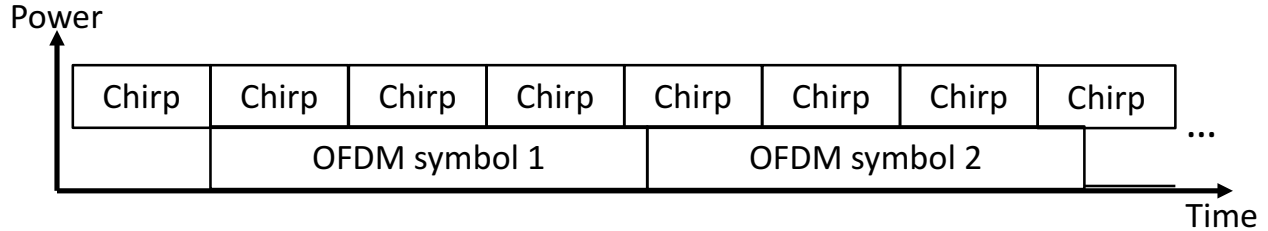


Figure 4.4: Time-power representation of proposed NOMA frame for DFRC.

M OFDM symbols in a frame during $T_{\text{sym}} = T - \tau$, the time-domain OFDM signal can be represented as follows:

$$\bar{s}_{\text{OFDM}}(t) = \sum_{m=0}^{M-1} \bar{s}_m(t) \times \text{rect} \left(\frac{t - mT_{\text{OFDM}}}{T_{\text{OFDM}}} \right), \quad 0 \leq t \leq T_{\text{sym}}. \quad (4.5)$$

In the proposed NOMA scheme, the transmitted frame $s(t)$ superimposes both waveforms. To obtain the radar-sensing and communication (RCS) information of the objects in the environment, single chirp is prepended to the NOMA frame. The final transmit frame for the objectives of multi-functional radar-sensing and communication transmission is designed as follows:

$$s(t) = \begin{cases} s_{\text{FMCW}}(t), & \text{if } 0 \leq t \leq \tau, \\ s_{\text{FMCW}}(t) + \bar{s}_{\text{OFDM}}(t), & \text{if } \tau < t \leq T. \end{cases} \quad (4.6)$$

The transmitted frame can be seen in Figure 4.4 where it starts with a chirp following the superimposed OFDM symbols and many chirps. The waveforms are superimposed in a way that the allocated bandwidth is the same for each waveform type. The time-frequency illustration of the superimposed signal can be seen in Figure 4.5. It can be realized that the OFDM signal is distributed along with the whole bandwidth, whereas FMCW waveform patterns consecutive pulses whose frequency increases linearly. It should be noted that there is power leakage in frequency band in the case of transition from one waveform to another. It can be reduced with proper windowing operations. Then, the baseband signal $s(t)$ is upconverted to the desired radio frequency (RF) band, where the transmitted passband

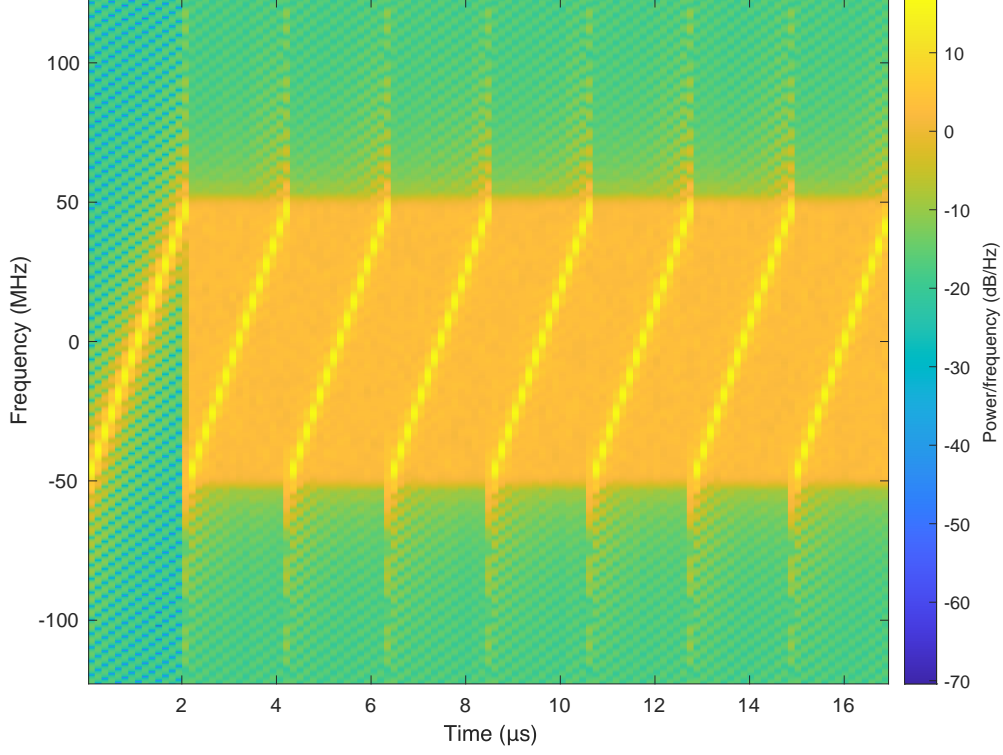


Figure 4.5: Time-frequency representation of proposed NOMA frame for DFRC.

analog signal becomes

$$x(t) = \Re\{s(t)e^{j(2\pi f_c t + \bar{\theta})}\}, \quad (4.7)$$

where $\Re\{\cdot\}$ denotes the real part of the complex quantity. The notations f_c and $\bar{\theta}$ are the carrier frequency and the initial phase of the transmitted signal, respectively.

4.2.3 Channel Effect

The Doppler shift due to mobility and flight time for the paths reflecting from the targets are as shown in Figure 4.1. It is assumed that the environment does not change over a coherent transmission time T leading to fixed Doppler shifts and delays. Actually, it is a reasonable assumption that is commonly used in radar literature [79]. With modeling the environment that signal propagates as a linear time-varying channel [62], the received

passband signal is represented as follows:

$$r(t) = \sum_{p=1}^P \alpha_p \Re\{x(t - \tau_p) e^{j2\pi(f_c + \psi_p)(t - \tau_p)}\} + n(t), \quad (4.8)$$

where α_p and τ_p are the attenuation factor depending on nonfluctuating radar cross section (RCS) and time delay related with the distance between the transmitter to target plus target to the receiver (bi-static range) for the p target, respectively. There exist total P target in the environment causing signal reflections, in other words, P is the number of specular scatterers. The notation $\psi_p = \frac{f_c v_p}{c}$ is the Doppler frequency associated with the p th path depending on relative speed v_p and the speed of light c . Also, $n(t) \sim \mathcal{CN}(0, \sigma^2)$ denotes the additive AWGN. The attenuation factor α_p is proportional to the large-scale path-loss. Having the path distance d between receiver and transmitter, the large-scale path-loss G is given as

$$G = \frac{G_{\text{TX}} G_{\text{RX}} \lambda^2}{(4\pi)^2 d^{\text{PL}}}, \quad (4.9)$$

where PL is the path-loss exponent, G_{TX} and G_{RX} are the transmit and receive antenna gain, respectively.

4.2.4 Multi-functional Reception

In this section, the receiver scheme for radar-sensing and communication operations is investigated. Since the receiver performs both functions, the knowledge obtained from one process can be leveraged to another to improve the performance.

4.2.4.1 Bi-static Radar Functionality

Down-converting the received passband signal $r(t)$ into baseband and sampling with the frequency of $F_s = N\Delta f$, the discrete-time signal becomes

$$y[n] = \sum_{p=1}^P h_p x(n/F_s - \tau_p) e^{j2\pi n\psi_p/F_s} + w(n), \quad n \in \mathbb{N}^+, \quad (4.10)$$

and

$$h_p = \alpha_p e^{-j2\pi(f_c + \psi_p)\tau_p + j\bar{\theta}}, \quad (4.11)$$

where h_p is the complex channel gain of p th target and $\bar{\theta}$ is the phase error. Then, the stretch processing is employed in the discrete domain for the superimposed signal to get delays and Doppler shifts estimations. The processed signal in one chirp time interval can be written as

$$\bar{y}[n'] = y[n'] \times e^{-j\pi\beta(n'/F_s)^2/\tau}, \quad n' = 1, 2, \dots, \lfloor \tau F_s \rfloor = N_c, \quad (4.12)$$

and dechirping process is repeated for each chirp time interval. Remember that stretch processing is generally done in time domain with down-conversion. However, here it is assumed that the occupied bandwidth of FMCW is the same as OFDM bandwidth, therefore, the sampling rate F_s for both radar and communication is taken as equal to each other.

The fast-time/slow-time coherent processing interval (CPI) matrix $\mathbf{K} \in \mathbb{C}^{K \times N_c}$ is formed where fast time samples (l) are obtained at the rate of F_s from the points on each chirp. Slow-time samples (k) are taken from the points on every chirp at the same fast-time sample point. Then this matrix is utilized to perform periodogram based radar processing. The output power of the periodogram at the m th Doppler and n th range bin is

$$P(m, n) = \frac{1}{KN_c} \left| \underbrace{\sum_{k=0}^{N_c-1} \left(\overbrace{\sum_{l=0}^{K-1} (\mathbf{K})_{k,l} e^{-j2\pi \frac{lm}{K}}}^{N_c \text{ FFTs of length } K} \right) e^{-j2\pi \frac{kn}{N_c}}}_{K \text{ FFTs of length } N_c} \right|^2, \quad (4.13)$$

sinusoids in \mathbf{K} related to object's distance and velocity lead to peaks in $P(m, n)$. Then certain distance and velocity values can be found from related range and Doppler bin value of peaks.

Estimation of complex attenuation factor h_p for every p th scatterer (target) is done with the first chirp by the least-square estimation [81]. It is worth to note that first chirp in the transmitted frame is interference-free as seen in Figure 4.4. Let the vector $\mathbf{y}_c \triangleq [y[1], y[2], \dots, y[\tau F_s]]^T$ be the samples of the received signal throughout the time τ , the estimated complex attenuation coefficients $\hat{\mathbf{h}} \triangleq [\hat{h}[1], \hat{h}[2], \dots, \hat{h}[P]]^T$ become

$$\hat{\mathbf{h}} = \arg \min_{\mathbf{h}} (\mathbf{y}_c - \mathbf{B}\mathbf{h})^H (\mathbf{y}_c - \mathbf{B}\mathbf{h}), \quad (4.14)$$

where \mathbf{B} is a $(\tau F_s - \bar{n}) \times P$ matrix whose rows corresponds to different shifts of the transmitted chirp where shift values are determined according to the estimated range value of the p th scatterer (target). The offset value $\bar{n} \in \mathbb{N}$ depends on the maximum range requirement of the system. Also, the selection of higher value for \bar{n} decreases fluctuations in the estimation of $\hat{\mathbf{h}}$ depending on Doppler shifts along with one chirp, whereas the maximum range is reduced. By differentiating with respect to \mathbf{h} and setting the result equal to zero, the least-square estimation of the channel becomes

$$\hat{\mathbf{h}} = (\mathbf{B}^H \mathbf{B})^{-1} \mathbf{B}^H \mathbf{y}_c. \quad (4.15)$$

Besides the estimation of delays τ_p and Doppler shifts ψ_p , the matrix $\hat{\mathbf{h}}$ completes the process to recreate the channel matrix \mathbf{H} with some estimation errors.

4.2.4.2 Communication Functionality

Here, the communication symbols are demodulated using the estimated channel knowledge in the previous section. Let the channel gain of the k th sample of the transmitted signal during the reception of the n th sample denote as $h_{n,k}$. Also, if the discrete channel convolution matrix along one OFDM symbol duration with N_{OFDM} samples is shown as

$\mathbf{H} \in \mathbb{C}^{(N_{\text{OFDM}}) \times (N_{\text{OFDM}})}$, the element in the k th column of the n th row of \mathbf{H} is $h_{n,k}$. Firstly, the FMCW sequence is removed from the total received signal by using estimated channel matrix $\hat{\mathbf{H}}$ as follows:

$$\mathbf{y}_{\text{OFDM}} = \mathbf{y} - \hat{\mathbf{H}}\mathbf{s}_{\text{FMCW}}, \quad (4.16)$$

where $\mathbf{y}_{\text{OFDM}} = [\mathbf{y}_1, \mathbf{y}_2, \dots, \mathbf{y}_M]$ and \mathbf{y}_m is the m th OFDM symbol in the received vector \mathbf{y} . The CP addition matrix $\mathbf{A} \in \mathbb{R}^{N_{\text{OFDM}} \times N}$ is defined as

$$\mathbf{A} = \begin{bmatrix} \mathbf{0}_{N_g \times N} & \mathbf{I}_{N_g} \\ & \mathbf{I}_{N_{\text{OFDM}}} \end{bmatrix}, \quad (4.17)$$

and the CP removal matrix is generated as $\mathbf{B} = [\mathbf{0}_{N \times N_g} \mathbf{I}_N]$ where N_g is the total sample number during CP duration T_g . The matrix $\hat{\Theta} \in \mathbb{C}^{N \times N}$ is the estimated channel frequency response (CFR) matrix which equals to

$$\hat{\Theta} = \mathbf{F}_N \mathbf{B} \hat{\mathbf{H}} \mathbf{A} \mathbf{F}_N^H. \quad (4.18)$$

The diagonal components of (4.18) are the channel coefficients scaling the subcarrier in interest collected in a vector $\hat{\theta} = \text{diag}(\hat{\Theta})$. Off-diagonal components of $\hat{\Theta}$ are not zero due to Doppler effect from the channel causing ICI. Finally, estimates of QAM data symbols for m th OFDM symbol are obtained as:

$$\hat{\mathbf{d}}_m = \left(\left(\text{diag}(\hat{\theta} \odot \hat{\theta}^*) \right)^{-1} \text{diag}(\hat{\theta})^* \mathbf{F}_N \mathbf{B}_K \mathbf{y}_m \right), \quad (4.19)$$

where $\text{diag}(\hat{\theta})$ returns a square diagonal matrix with the elements of vector $\hat{\theta}$ on the main diagonal. This equation finalizes the proposed receiver structure without introducing pilots on the OFDM subcarriers to estimate the channel.

Table 4.1: Simulation Parameters for NOMA Based DFRC System

Parameter	Value
Carrier frequency (f_c)	28 GHz
Bandwidth (β)	122.88 MHz
Chirp duration (T_c)	2.4 μ s
Number of chirps (T_c)	640 μ s
Duration of proposed NOMA scheme (T)	2.8 ms
Subcarrier spacing(Δf)	60 kHz
Number of FFT(N)	2048
Range of targets	15 m, 90 m and 180 m
Relative velocity of targets	0 m s ⁻¹ , 23.2 m s ⁻¹ and -30.9 m s ⁻¹

4.2.5 Numerical Evaluation of the Proposed NOMA Scheme

In this section, the radar-sensing and communication performance of the proposed NOMA scheme is compared with the OFDM scheme with pilots for JRC systems proposed in [78]. Comb-type pilot design is used for the compared scheme and pilot spacings in frequency (D_f) and time (D_t) is arranged as follows [82]:

$$D_f \leq \frac{1}{\tau_{\max} \Delta f}, \quad (4.20)$$

and

$$D_t \leq \frac{1}{2f_{d_{\max}} T_{\text{sym}}}, \quad (4.21)$$

where $f_{d_{\max}}$ and τ_{\max} denote the maximum Doppler shift and delay caused by targets, respectively. To satisfy the constraints given in (4.20) and (4.21), QPSK modulated Gold sequences [83] are inserted into one in every four subcarriers for each OFDM symbol.

Simulation parameters for proposed NOMA scheme depending on radar and communication requirements are shown in Table 5.1. It is assumed that the maximum delay τ_{\max} is smaller than the CP length of each OFDM symbol and the channel includes three targets in the bi-static radar case, as shown in Figure 4.1. The PDP of the channel is determined as an exponentially decaying function where the power of channel coefficients is set as $E[h_p(\gamma)]^2 = \eta e^{-\gamma p}$, where η denotes the normalization factor and p is the target index. The

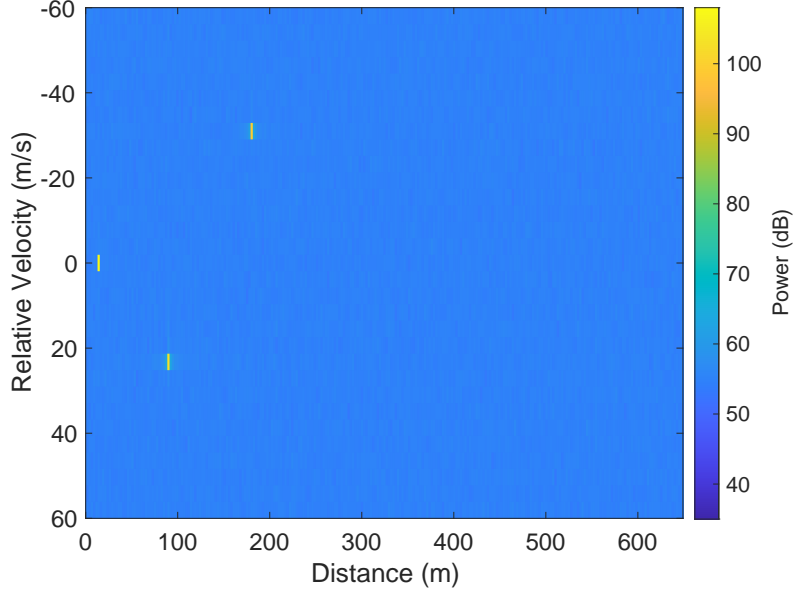


Figure 4.6: Radar-sensing performance of the proposed NOMA scheme at 10 dB SNR.

decaying factor γ is taken as unity for simplicity and each tap amplitude follows Rayleigh distribution. During the simulation, powers of waveforms P_{OFDM} and P_{FMCW} equal to each other. However, the distribution of power between FMCW and OFDM can be arranged according to system requirements for each chirp and OFDM symbol. Then, it turns out a optimization problem with constraints of data rate and Cramér-Rao lower bound (CRLB) of parameter estimation for communication and radar-sensing functionalities, respectively.

The comparison of radar-sensing performance of proposed NOMA scheme and OFDM JRC is depicted in Figure 4.6 and 4.7 when the SNR of the transmitted signal is 10 dB. For both scheme, periodogram based estimation is utilized which is explained in (4.36). As it can be seen in Fig. 4.6, three different reflections can be identified clearly, whereas OFDM JRC scheme includes side-lobes seen in Fig. 4.7 which deteriorates the radar detection performance. Side-lobes in the periodogram of OFDM JRC scheme results from the copies of the existing targets beyond the unambiguous radar range due to fixed placement of pilots.

MSE is calculated considering diagonal elements of $\hat{\Theta}$ presented in (4.18) and its true value Θ . The MSE is represented as $\sigma_e^2 = \frac{E[|\hat{\theta} - \theta|^2]}{E[|\theta|^2]}$, where $E[\cdot]$ denotes the expected value. Channel estimation process of conventional OFDM JRC scheme is performed with transform

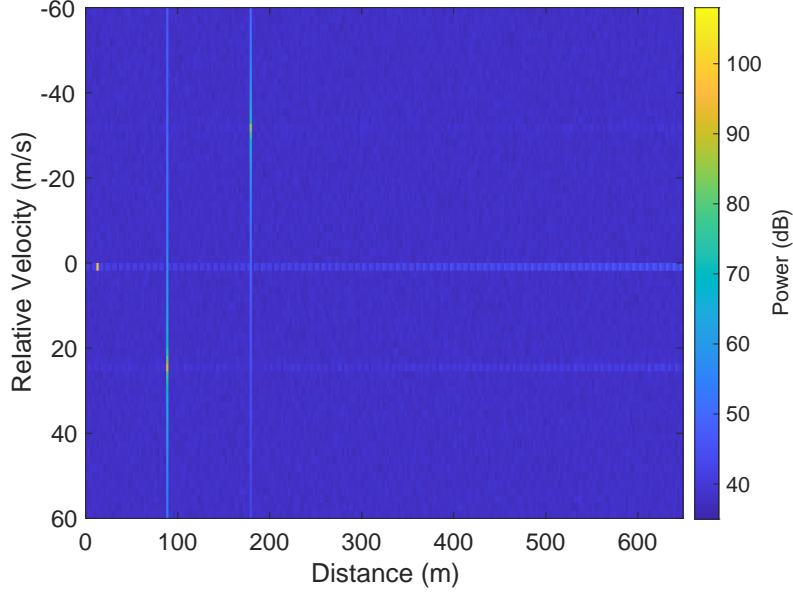


Figure 4.7: Radar-sensing performance of the conventional OFDM scheme with comb-type pilot structure at 10 dB SNR.

domain technique [82]. First, the CFR vector is obtained by implementing spline interpolation over pilots. Then, IFFT of the CFR is taken. The resultant transform domain is the time domain, where typically the channel taps are concentrated into a sub-region. By zeroing the terms out of this sub-region that corresponds to noise only, the significant taps are obtained. This sub-region is determined via the length of CP. The noise reduced signal is then transformed back into the frequency domain via FFT operation to retain $\hat{\theta}$.

MSE performance of the proposed NOMA scheme and OFDM JRC can be seen in Fig. 4.8, which degrades as SNR increases. Proposed NOMA scheme performs well beyond the OFDM JRC. It is worth noting that the complex attenuation factors for each target are estimated using the first chirp, while delays and Doppler shifts are estimated using the FMCW waveform in the proposed NOMA scheme. After evaluating the complex attenuation factor h_p denoted in (4.11), the estimation of channel matrix $\hat{\mathbf{H}}$ is created by using the obtained values of Doppler shifts and delays which is done previously via FMCW waveform. Finally, this channel estimation is used to demodulate communication symbols in the OFDM waveform.

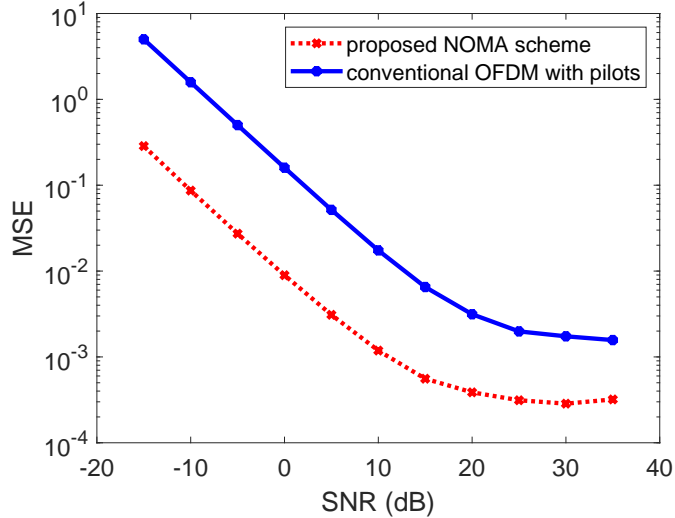


Figure 4.8: MSE of proposed method at 20 dB.

The BER performance of the proposed NOMA scheme, where channel estimation knowledge is leveraged from the FMCW waveform, can be seen in Fig. 4.9 by comparing it with OFDM JRC. The information bits are encoded via 1/2 rate convolutional codes with interleaving to get rid of the deep fading effect of the channel. The proposed NOMA scheme is also compared with the presence of perfect CSI. In other words, the FMCW waveform is totally removed from the superimposed signal without affecting the OFDM waveform and OFDM signal is demodulated with perfect channel estimation. Proposed NOMA scheme outperforms the conventional OFDM JRC scheme proposed in [78] which reaches error floor after 25 dB due to multiple Doppler shifts in the channel. It can also be seen that performance degradation of the proposed NOMA scheme is negligible compared to case where perfect CSI is available. It should be noted that, ICI effect is not totally removed and demodulation is performed as it is shown in (4.19). To sum up, non-orthogonally coexistence of two different waveforms, OFDM and FMCW, has good sensing accuracy with minimal degradation to communication performance.

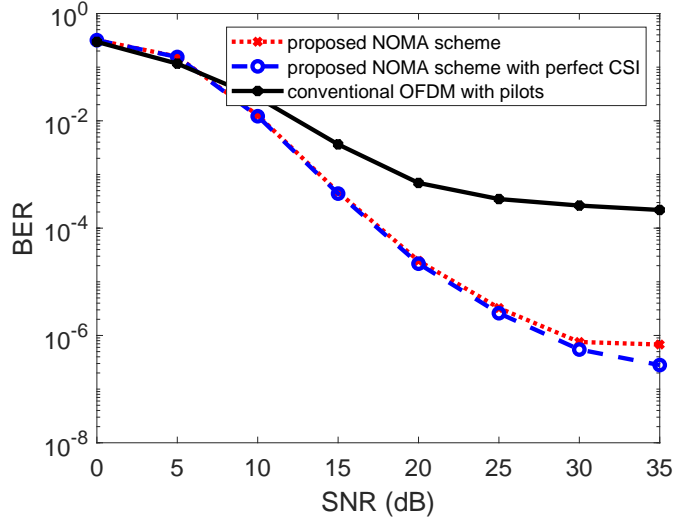


Figure 4.9: BER performance of proposed method at 20 dB.

4.3 OFDM-IM for DFRC Systems

DFRC provides hardware and software convergence of radar-sensing and communication applications to utilize scarce resources more efficiently and effectively. With these and upcoming considerable contributions, DFRC is envisioned to be implemented and provide service to many applications, some of which include intelligent vehicular transportation, aircraft traffic, and military applications whether it is in the air, sea or space. JCR, which is a form of the DFRC system, creates a fusion of both functionalities in a unified platform which is feasible since the gap between radar and communication systems is small. This unification grants not only a cost reduction, but also enables an efficient spectrum usage, efficient power consumption, and a more compact system size. One major challenge of designing a JCR system is the performance criteria [4], i.e., both functionalities are desired to be designed cooperatively without performance degradation. Additional challenges include dedicated receiver algorithms and complication of the transmitter design.

JCR research has pushed significant efforts to share the spectrum between radar and communication without interference. Fundamental concepts and important performance metrics have been discussed and resource management approaches have been analyzed for

JCR in [76]. Waveform design plays a critical role in the JCR concept and a single novel waveform for both radar and communication functionalities, without a reduction of neither’s performance, is yet to exist. Orthogonal frequency division multiplexing (OFDM) is a very popular waveform integrated to JCR [78]. Also, a JCR technique on the wireless system standard IEEE 802.11 employing OFDM is proposed in [84] with dedicated OFDM-radar algorithms. However, for the dual-functionality of the system, it is not mandatory to have a single waveform. Different waveforms may be superimposed and transmitted simultaneously as in [67, 7], where frequency modulated continuous wave (FMCW) and OFDM are used. Additionally, millimeter wave (mmWave) communication provides large transmission bandwidth enabling large data rates, and has a potential to collaborate with JCR. From the signal processing perspective, [85] dives in to mm-Wave JCR systems and waveform design. As a further note, [86] explores state-of-the-art JCR evolution with an comprehensive survey on the DFRC technology.

On the other hand, index modulation (IM) is a simple, spectral and energy efficient scheme that can be implemented to many waveforms and techniques, such as OFDM. OFDM with index modulation (OFDM-IM) is a very popular scheme that not only conveys information through quadrature amplitude modulated symbols but also through the indices of active subcarriers in the frequency domain [49]. It has been utilized in various ways to transmit additional bits, provide flexibility, improve reliability and more such as in [87, 88, 89, 90]. Superiorities of OFDM-IM over classical OFDM include efficient implementation and flexibility of active subcarriers, energy-efficiency, reduced peak-to-average power ratio (PAPR), robustness to inter-carrier interference (ICI) and improved bit error performance [45]. Recently, IM has even been applied to DFRC. In [91], IM-aided circularly shifted chirps are proposed for DFRC systems. In [92], information is embedded on the DFRC system in an IM manner, where different frequency and antenna selections construct possible constellation space. However, to best of our knowledge, there is no study focusing on the implementation and analysis of OFDM-IM in JCR systems.

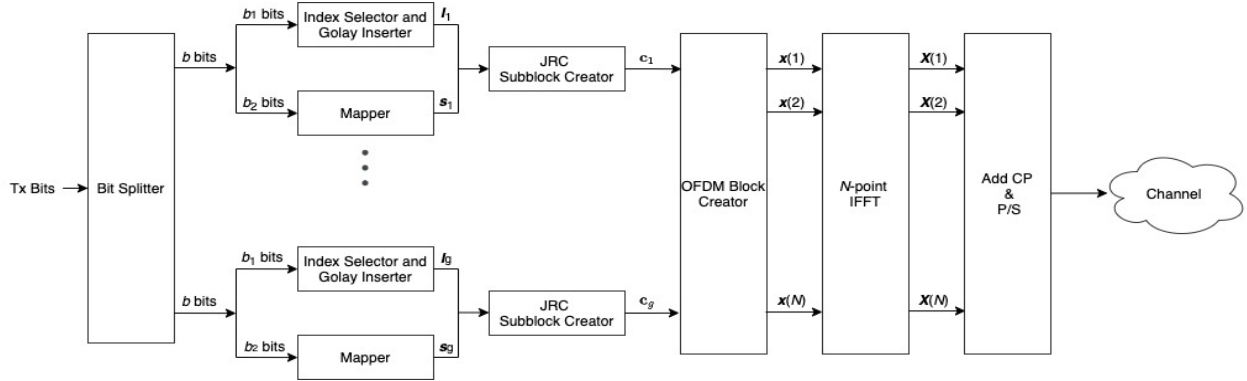


Figure 4.10: Transmitter structure for the m^{th} OFDM symbol of the proposed DFRC system.

This study sheds lights on the drawbacks of pilot-based OFDM in JCR system such as limited unambiguous radar range and channel estimation errors, and proposes a novel structure using OFDM-IM to overcome these problems. To perform radar functionality on the proposed structure, Golay complementary sequences (GCS) are inserted to OFDM-IM waveform. Since GCS have suitable ambiguity function properties for radar functionality [93], they are used as pre-known radar symbols in our proposed scheme.

The contributions of this study can be summarized and highlighted as follows:

- A novel JCR waveform scheme is proposed using the OFDM-IM structure and GCS as radar symbols.
- The transmitter and receiver structures are introduced to improve both the communication and radar performance of the proposed waveform scheme.
- A novel channel estimation scheme is proposed for OFDM-IM utilizing its radar functionality.
- Superiority of the proposed scheme is analyzed compared to conventional OFDM structure with comb-type pilots for JCR systems proposed in [78].

Look-up Table for $n = 4$ and $k = 2$					
m_1	d	i_1	i_2	i_3	i_4
[00]	0	C_1	C_2	null	radar
[01]	1	null	radar	C_1	C_2
[10]	2	radar	C_1	C_2	null
[11]	3	C_1	null	radar	C_2

Figure 4.11: Look-up table for two active subcarriers out of four subcarriers in a subblock.

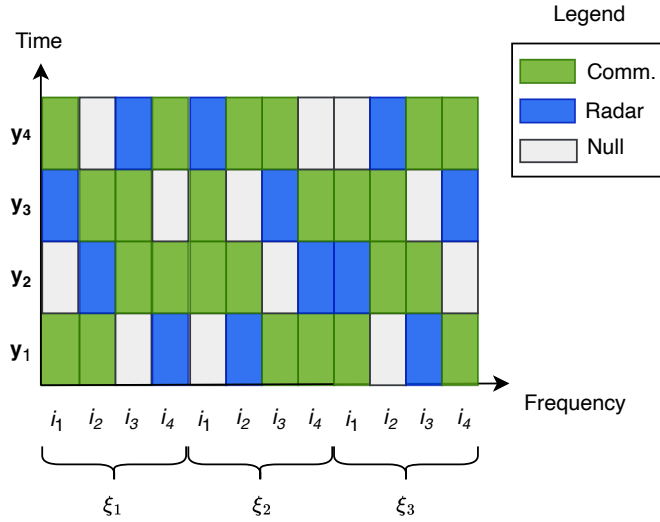


Figure 4.12: Transmitted OFDM-IM JCR frame.

4.3.1 System Model

In this section, the system model of the proposed OFDM-IM JCR scheme is provided. First, the transmitter architecture is presented, then the channel model is explained.

4.3.1.1 Transmitter Design

The block diagram of the considered OFDM-IM JCR system is presented in Figure 4.10. As in classical OFDM-IM, the entire OFDM-IM symbol consisting of N subcarriers is split into total G subblocks. Since each subblock undergoes the same procedures, it is sufficient to consider the ξ^{th} subblock $\mathbf{x}(\xi) \in \mathbb{C}^{g \times 1}$ where $\xi \in \{1, \dots, G\}$. Each subblock has a length

of $g = N/G$ subcarriers with indices $(i_1, \dots, i_n, \dots, i_g)$ where i_n is the n^{th} subcarrier index of the ξ^{th} subblock.

For the ξ^{th} subblock, incoming b bits are split into b_1 and b_2 bits. The $b_1 = \lfloor \log_2 \binom{g}{k} \rfloor$ bits determine the indices of the k communication, r radar and l null subcarriers of a subblock, via binary-to-decimal conversion, using a pre-defined look-up table. Then the remaining $b_2 = k \log_2(Q)$ bits assign quadrature amplitude modulation (QAM) symbols, which are chosen from complex set \mathbb{S} , to the communication subcarriers of the subblock. Consequently, a total of

$$b = b_1 + b_2 = \left\lfloor \log_2 \binom{g}{k} \right\rfloor + k \log_2 Q \quad (4.22)$$

bits can be transmitted per subblock. An example look-up table with a subblock size of four and two communication subcarriers ($k = 2$) per subblock with symbols C_o , where $o \in \{1, 2\}$, is shown in Figure 4.11. In this example, there is one radar ($r = 1$) and one null subcarrier ($l = 1$) in a subblock. The number of total radar symbols in one OFDM symbol is denoted as $R = rN/g$. Figure 4.12 is presented to visualize the considered time-frequency lattice according to Figure 4.11. The flexible design of OFDM-IM allows the proposed scheme to utilize the whole bandwidth for radar processing such as frequency-agile radars. At the receiver side, the location of the radar symbol is found via estimation of the null subcarrier location. Therefore, null subcarriers are distributed intelligently to find the locations of radar symbols.

Next, two complementary Golay sequences G_a and G_b , both with length $R/2$, are generated. In succession, the elements of G_a are placed into the first half of the OFDM-IM JCR block with $N/2$ subcarriers. Subsequently, the aforementioned is repeated for the remaining $N/2$ subcarriers using G_b . After this point, the procedures as in OFDM are applied. The time domain m^{th} OFDM symbol \mathbf{x}_m is generated by applying the inverse fast Fourier (IFFT) transformation on frequency domain samples \mathbf{X}_m :

$$\mathbf{x}_m = \text{IFFT}\{\mathbf{X}_m\} = \left[X_{m,1} \quad X_{m,2} \quad \cdots \quad X_{m,N} \right]^T. \quad (4.23)$$

Let the matrix $\mathbf{X} \in \mathbb{C}^{M \times N}$ be the frame of frequency domain transmitted symbols, where the element $X_{m,n}$ is the m th symbol transmitted on subcarrier n , for $m = 1, \dots, M$ and $n = 1, \dots, N$. After the IFFT operation, a cyclic prefix (CP) of length C samples expressing mathematically as follows:

$$\left[X_{m,(N-C+1)}, \dots, X_{m,(N-1)}, X_{m,N} \right]^T, \quad (4.24)$$

is added to the beginning of the OFDM symbol. Then, the OFDM-IM frame $\mathbf{x} \in \mathbb{C}^{M(N+C) \times 1}$ including M OFDM symbols is generated by appending each OFDM symbol back to back.

Afterwards, the baseband discrete signal \mathbf{x} is processed with digital-to-analog converter (DAC) and upconverted to the desired radio frequency (RF) band, where the transmitted passband analog signal becomes

$$\tilde{\mathbf{x}}(t) = \Re\{\mathbf{x}(t)e^{j(2\pi f_c t + \bar{\theta})}\}, \quad (4.25)$$

where $\Re\{\cdot\}$ denotes the real part of a complex quantity. Here, f_c and $\bar{\theta}$ are the carrier frequency the initial phase of the transmitted signal, respectively, where f_c is selected according to the 5G mmWave-band.

4.3.1.2 Channel Model

Throughout the study, the communication receiver is also exploited as a radar receiver. Hence, the bi-static radar model is used, where the transmitter and the radar receiver are not co-located. The wireless channel is dedicated for both communication and radar operation, where the transmitted OFDM-IM JCR waveform propagates through. The channel model includes complex channel gain, Doppler shift and delay for every path. It is also assumed that the transmission of the frame is long enough to be affected from time selectivity, but short enough such that the time variation can be accurately modeled as depending only on per-tap linear phase variations due to Doppler effects [94]. Therefore, the linear time-variant

channel in the time-delay domain, $c(t, \tau)$, can be modeled as follows [62]:

$$c(t, \tau) = \sum_{p=1}^P \alpha_p e^{j2\pi\nu_p t} \delta(\tau - \tau_p), \quad (4.26)$$

where α_p , τ_p , and ν_p denote the complex attenuation factor, bi-static time delay, and Doppler frequency shift associated with the p^{th} target where there are total of P targets. The estimation of the complex gain, delay and Doppler shift from each tap of the multipath channel is performed via radar signal processing techniques. It is known that, the frequency domain channel coefficients for an entire frame can be expressed as the superimposition of two-dimensional complex sinusoids which allow us to use periodogram based delay and Doppler shift estimation. Down-converting the received passband signal into baseband and sampling with the frequency of $F_s = N\Delta f$, the discrete-time signal becomes

$$y[n] = \sum_{p=1}^P \alpha_p \times \left(\frac{n}{F_s} - \tau_p \right) e^{j2\pi n \frac{\nu_p}{F_s}} + w[n], \quad n \in \mathbb{N}^+, \quad (4.27)$$

where $w[n] \sim \mathcal{CN}(0, \sigma^2)$ denotes the sampled additive white Gaussian noise (AWGN). With the assumption that the channel components remains as same during transmission of an OFDM frame and the CP length (C) is larger than maximum bi-static delay eliminating inter-symbol interference (ISI), the received vector is given by

$$\mathbf{y} = [y_1^T \cdots y_M^T]^T = \mathbf{H}^t \mathbf{x} + \mathbf{w}, \quad (4.28)$$

where $\mathbf{H}^t \in \mathbb{C}^{M(N+C) \times M(N+C)}$ is the time domain channel matrix and \mathbf{w} is the noise vector. The signal-to-noise ratio (SNR) is defined as $1/\sigma^2$.

The relation of (4.26) with the time domain channel matrix \mathbf{H}^t can be represented as follows:

$$\mathbf{H}^t = \sum_{p=1}^P \alpha_p \mathbf{\Pi}^{n\tau_p} \mathbf{\Delta}(\nu_p), \quad (4.29)$$

where the delay matrix $\mathbf{\Pi}^{n_{\tau p}} \in \mathbb{C}^{M(N+C) \times M(N+C)}$ is the forward cyclic shifted permutation matrix according to the delay of the p th path. It can be expressed as follows:

$$\mathbf{\Pi} = \begin{bmatrix} 0 & 0 & \cdots & 0 & 1 \\ 1 & 0 & \cdots & 0 & 0 \\ 0 & 1 & \cdots & 0 & 0 \\ \vdots & \vdots & \ddots & \vdots & \vdots \\ 0 & 0 & \cdots & 1 & 0 \end{bmatrix}, \quad \text{and} \quad n_{\tau p} = \left\lfloor \frac{\tau_p}{N\Delta f} \right\rfloor. \quad (4.30)$$

The Doppler shift matrix for the p th path, $\mathbf{\Delta}(\nu_p) \in \mathbb{C}^{M(N+C) \times M(N+C)}$, can be written as follows:

$$\mathbf{\Delta}(\nu_p) = \text{diag} \left(\left[e^{\frac{j2\pi\nu_p}{N\Delta f}}, e^{\frac{j2\pi\nu_p^2}{N\Delta f}}, \dots, e^{\frac{j2\pi\nu_p(N+C)M}{N\Delta f}} \right] \right), \quad (4.31)$$

where there are total P paths with different delays and Doppler shifts.

The channel estimation and decoding processes are explained in the next sections.

4.3.2 Bi-static Radar and Channel Estimation

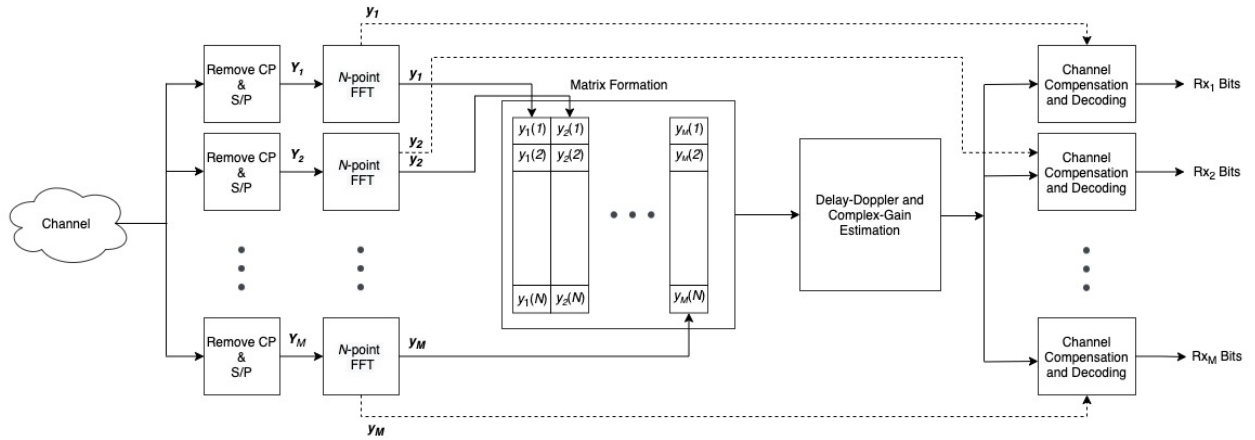


Figure 4.13: Decoding process for an OFDM-IM frame of the proposed DFRC system.

In this section, bi-static radar signal processing scheme is introduced using the known Golay sequence on the transmitted OFDM-IM frame. The general structure of the steps followed both in this section and next section can be seen in Figure 4.13. Revisiting (4.28),

the received signal can be written in frequency domain as follows:

$$\mathbf{Y} = \mathbf{H}^f \odot \mathbf{X} + \mathbf{Z}, \quad (4.32)$$

where \odot denotes the Hadamard product, $\mathbf{Y} \in \mathbb{C}^{M \times N}$ is the frequency domain received matrix, and $\mathbf{Z} \in \mathbb{C}^{M \times N}$ is frequency domain representation of the noise \mathbf{w} . The elements of frequency domain channel matrix $\mathbf{H}^f \in \mathbb{C}^{M \times N}$ can be expressed as follows:

$$H_{m,n}^f = \sum_{p=1}^P \alpha_p e^{-j2\pi\nu_p T_d(m-1)} e^{-j2\pi(n-1-\lfloor N/2 \rfloor)\tau_p/T}, \quad (4.33)$$

where T_d is the OFDM symbol duration after cyclic prefix (CP) addition to the original duration $T = \frac{1}{\Delta f}$.

4.3.2.1 Null Subcarrier Estimation

In this step, the entire \mathbf{Y} matrix is processed to estimate the null subcarrier locations. Once the null subcarrier location is found for each subblock, the location of radar and communication subcarrier can also be found as it can be seen in Figure 4.11. For each ξ subblock in the m^{th} OFDM symbol, the null subcarrier estimation $(n_m^\xi)^*$ is performed as follows:

$$(n_m^\xi)^* = \min_{n: n \in \{1, \dots, N/g\}} |Y_{m,n}^\xi|^2 \quad (4.34)$$

Afterwards, the vector $\mathbf{n}^* \in \mathbb{C}^{1 \times M \cdot R}$ indicating null subcarriers is constructed by gathering all estimated $(n_m^\xi)^*$. Once the null subcarrier location is estimated, locations of radar and communication subcarriers are also known due to the mapping scheme shown in Figure 4.11.

4.3.2.2 De-chirping

After the null subcarrier estimation de-chirping of the received sequence is done. Also, it is followed by filling estimated communication subcarriers with zeros. In this step, the fast-time/slow-time coherent processing interval matrix $\mathbf{K} \in \mathbb{C}^{M \times N}$ is formed. Let the matrix

$\tilde{\mathbf{X}} \in \{-1, 1\}^{M \times R}$ denote the known Golay sequences for all OFDM frame. Then, the elements $K_{m,n}$ of matrix \mathbf{K} becomes

$$K_{m,n} = \begin{cases} Y_{m,n}/X_{m,\beta}, & \text{when } n \in \mathbf{n}^*, \\ 0, & \text{otherwise,} \end{cases} \quad (4.35)$$

where the index in Golay sequence matrix is $\beta = \lceil \frac{n \cdot g}{N} \rceil$.

4.3.2.3 Delay and Doppler Shift Estimation

Delay and Doppler shift estimation of the proposed method is done via 2D-periodogram method. The matrix \mathbf{K} is utilized to perform periodogram-based radar processing. The output power of the periodogram at the ι^{th} Doppler and ς^{th} range bin is

$$P(\iota, \varsigma) = \frac{1}{NM} \left| \underbrace{\sum_{m=0}^{M-1} \left(\sum_{n=0}^{N-1} \mathbf{K}_{m,n} e^{-j2\pi \frac{n\iota}{N}} \right) e^{-j2\pi \frac{m\varsigma}{M}}}_{N \text{ FFTs of length } M} \right|^2, \quad (4.36)$$

where sinusoids in \mathbf{K} related to object's distance and velocity lead to peaks in $P(\iota, \varsigma)$. Then certain distance and velocity values can be found from related range and Doppler bin value of peaks. The threshold value is set according to the SNR of the system. Distance d and velocity ν of the paths are found as follows:

$$d = \frac{\iota c}{\Delta f N} \quad \text{and} \quad \nu = \frac{\varsigma c}{f_c T} \quad (4.37)$$

where c denotes the speed of light.

4.3.2.4 Complex Attenuation Estimation

In this step, the complex attenuation factor of the channel is estimated. It is assumed that the total number of targets is known in advance. The number of targets can be obtained by simply putting a threshold in (4.36). Let the vector $\tilde{\mathbf{Y}} \in \mathbb{C}^{M \cdot R \times 1}$ denotes the complex

symbols extracted from the estimated radar subcarrier locations, which are also affected by the noise $\tilde{\mathbf{Z}} \in \mathbb{C}^{M \cdot R \times 1}$. Considering frequency domain channel shown in (4.33), $\tilde{\mathbf{Y}}$ can be written as follows:

$$\tilde{\mathbf{Y}} = \mathbf{\Omega}(\boldsymbol{\tau}, \boldsymbol{\nu}, \tilde{\mathbf{X}})\boldsymbol{\alpha} + \tilde{\mathbf{Z}}, \quad (4.38)$$

and the $MR \times P$ matrix $\mathbf{\Omega}$ as a function of $\boldsymbol{\tau}, \boldsymbol{\nu}, \tilde{\mathbf{X}}$ becomes

$$\mathbf{\Omega}(\boldsymbol{\tau}, \boldsymbol{\nu}, \tilde{\mathbf{X}}) = \begin{pmatrix} X_{1,1}\Psi(v_1)\Phi(\tau_1) & \dots & X_{1,1}\Psi(v_P)\Phi_{\tau_P} \\ \vdots & \ddots & \vdots \\ X_{1,R}\Psi(v_1)\Phi(\tau_1) & \dots & X_{1,R}\Psi(v_P)\Phi_{\tau_P} \\ \vdots & \ddots & \vdots \\ X_{M,1}\Psi(v_1)\Phi(\tau_1) & \dots & X_{M,1}\Psi(v_P)\Phi_{\tau_P} \\ \vdots & \ddots & \vdots \\ X_{M,R}\Psi(v_1)\Phi(\tau_1) & \dots & X_{M,R}\Psi(v_P)\Phi_{\tau_P} \end{pmatrix}, \quad (4.39)$$

where $\Psi(\nu_p) = e^{-j2\pi\nu_p T_d(m-1)}$ and $\Phi(\tau_p) = e^{-j2\pi(n-1-\lfloor N/2 \rfloor)\tau_p/T}$. Then, the estimation of complex attenuation factor vector $\hat{\boldsymbol{\alpha}} \in \mathbb{C}^{P \times 1}$ for all targets can be found as follows:

$$\hat{\boldsymbol{\alpha}} = (\mathbf{\Omega}^H \mathbf{\Omega})^{-1} \mathbf{\Omega}^H \tilde{\mathbf{Y}}, \quad (4.40)$$

where $(\cdot)^H$ denotes the Hermitian operator.

4.3.3 Communication Functionality and Decoding Algorithms

In this section, the decoding process of transmitted information is explained with two different options. Both options are numerically evaluated in the following section.

4.3.3.1 Null Subcarrier Estimation Based Decoding

Here, the null subcarrier estimation in the first step of radar processing is utilized to determine the location of communication symbols and the index bits b_1 . The QAM symbols

on estimated communication subcarrier locations is demodulated via well-known maximum likelihood (ML) QAM demodulation, which calculates the minimum Euclidean distance with the possible symbols in complex symbol set.

4.3.3.2 Maximum-likelihood Based Decoding

The full-ML detector considers all possible subblock realizations by searching for all possible subcarrier index combinations, the signal constellation points, and corresponding radar symbol for each subblock in order to make a joint decision on the active indices and the constellation symbols. For m^{th} OFDM symbol, full-ML detector is employed in each subblock by minimizing the following metric:

$$\left(\hat{\mathbf{l}}_{\xi}, \hat{\mathbf{s}}_{\xi}\right) = \arg \min_{\mathbf{l}_{\xi}, \mathbf{s}_{\xi}} \left\| \mathbf{Y}_m^{\xi} - \mathbf{c}^{\xi} \right\|^2, \quad (4.41)$$

where \mathbf{c} denotes all possible subblock realizations including radar symbol, null subcarrier and QAM symbols.

4.3.3.3 Soft Decoding with Channel Decoder

This section includes the log-likelihood ratio (LLR) calculations of the proposed OFDM-IM structure. Calculated LLRs are sent to the channel decoder as input. For the sake of fair comparison, we have used the log-sum approximation technique [51] to calculate approximate LLR of the proposed OFDM-IM scheme and conventional OFDM with comb-type pilot scheme [78]. The LLR of the bit i ($b_{\xi}^m(i)$) of the proposed OFDM-IM JCR scheme

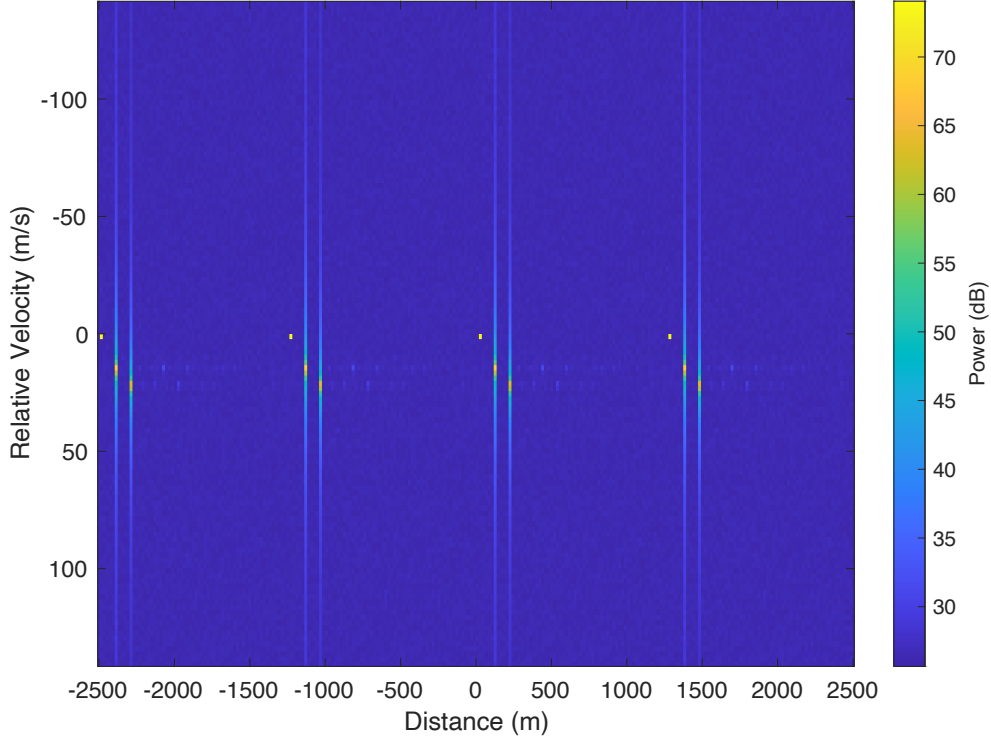


Figure 4.14: Sensing performance of the conventional OFDM with comb-pilots. Distance velocity plot of the three targets with velocities $[0, 14.9, 21.2]$ (m/s) and distances $[29.3, 127.3, 225.3]$ (m) at 10 dB SNR in conventional comb-type pilot-based OFDM.

at the ξ^{th} subblock of m^{th} OFDM symbol, $\Lambda_{\xi}^m(i)$ is

$$\begin{aligned}
 \Lambda_{\xi}^m(i) &= \log \left(\frac{f(\mathbf{Y}_m^{\xi} | b_{\xi}^m(i) = 0)}{f(\mathbf{Y}_m^{\xi} | b_{\xi}^m(i) = 1)} \right) \\
 &\approx \min_{\mathbf{b}_{\xi}^m: b_{\xi}^m(i)=1} \|\mathbf{Y}_m^{\xi} - \mathbf{h}_{\xi}^m \odot \mathbf{b}_{\xi}^m\|^2 \\
 &\quad - \min_{\mathbf{b}_{\xi}^m: b_{\xi}^m(i)=0} \|\mathbf{Y}_m^{\xi} - \mathbf{h}_{\xi}^m \odot \mathbf{b}_{\xi}^m\|^2, \tag{4.42}
 \end{aligned}$$

where $\mathbf{h}_{\xi}^m \in \mathbb{C}^{1 \times g}$ denote the channel state information (CSI) through ξ^{th} subblock of m^{th} OFDM symbol. Also, $\mathbf{b}_{\xi}^m(i) \in \mathcal{S}' = \{0, \mathbf{G}_a, \mathbf{G}_b, \mathbf{S}\}$ is the all possible symbol set that is inserted into the proposed OFDM-IM JCR structure.

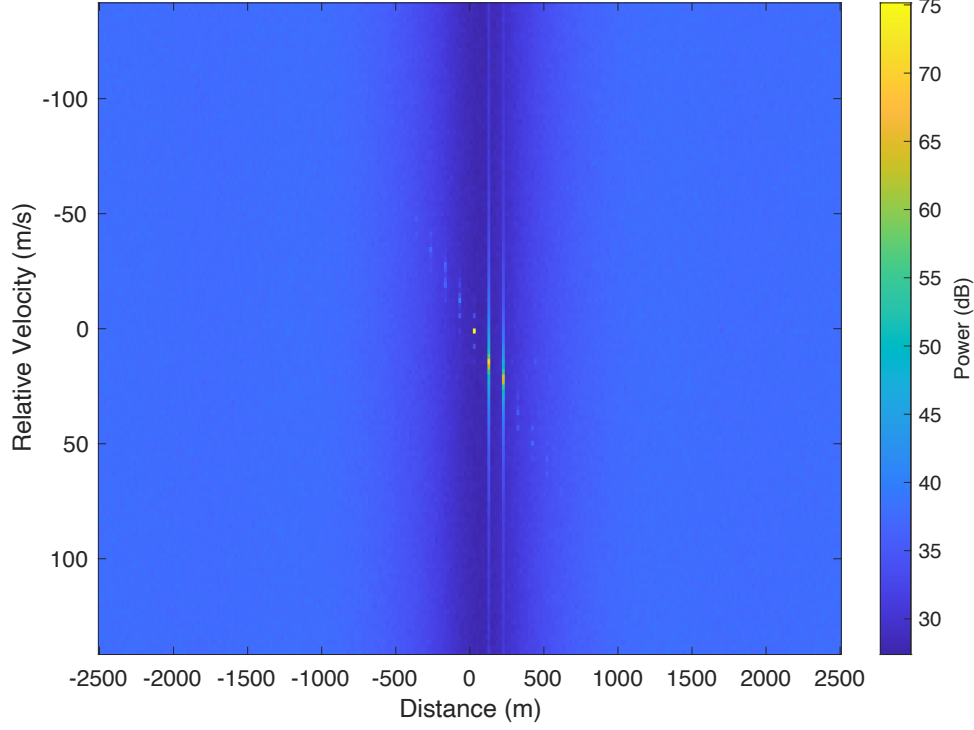


Figure 4.15: Sensing performance of the proposed OFDM-IM based DFRC system. Distance-velocity plot of the three targets with velocities $[0, 14.9, 21.2]$ (m/s) and distances $[29.3, 127.3, 225.3]$ (m) where SNR is 10 dB in the proposed OFDM-IM JCR scheme.

4.3.3.4 Complexity Analysis

Here, the complexity analysis of the proposed decoding methods is performed to compare decoding schemes. The complexity of null subcarrier based decoding becomes, in terms of complex multiplications, $\sim \mathcal{O}(k|S|)$ whereas the complexity of ML based decoding is $\sim \mathcal{O}(2^{b_1}|S|^k)$. The complexity of LLR calculation, in terms of complex multiplications, is also $\sim \mathcal{O}(2^{b_1}|S|^k)$, however, this calculation is followed by the complex channel decoding process. Therefore, the overall complexity is higher than previous two methods.

4.3.4 Simulation Results

This section demonstrates the applicability of the proposed OFDM-IM JCR waveform structure in the presence of multiple and mobile targets. Mean-square error (MSE) and bit error rate (BER) metrics are used to demonstrate the radar-sensing and communication

Table 4.2: Simulation Parameters for OFDM-IM Based DFRC Analysis

Parameter	Value
Carrier frequency (f_c)	28 GHz
Bandwidth (BW)	15.4 MHz
OFDM symbol duration (τ)	16.7 μ s
Total OFDM frame duration (T)	2.4 ms
Subcarrier spacing (Δf)	60 kHz
Number of subcarriers (N)	256
Number of OFDM symbols (M)	180
Modulation order (Q)	4 (QPSK)

performance of the proposed scheme. Simulation parameters depending on radar and communication requirements are shown in Table 5.1. It is assumed that the maximum delay τ_{\max} caused by targets is smaller than the CP length of each OFDM symbol. The total symbol energy is set the same for the proposed scheme and conventional OFDM JCR scheme. For LDPC codes, NR LDPC codes with coderates 0.5 and 0.75 are implemented, where code-length is set to be 384, and the iteration number of decoding is 20. Interleaving after LDPC encoding is not implemented to have fair comparison between conventional OFDM JCR and proposed OFDM-IM JCR scheme. The number of subcarriers in one OFDM symbol is 256 due to the codelength and SE, and 180 OFDM symbols are transmitted with one OFDM frame. BER and MSE results are obtained with repeated 1000 Monte Carlo simulations to get ensemble averages. To compare the proposed OFDM-IM JCR scheme, the conventional OFDM JCR scheme with comb-type pilot arrangement is implemented which is proposed in [78], one out of four subcarriers is assigned with pilot symbol. For communication symbols, QPSK modulation is utilized. Therefore, the spectral efficiency of both schemes becomes 1.5 bit per subcarrier.

The power delay profile (PDP) of the channel is determined as an exponentially decaying function where the power of complex channel coefficients is set as $E[\alpha_p(\gamma)]^2 = \eta e^{-p}$, where

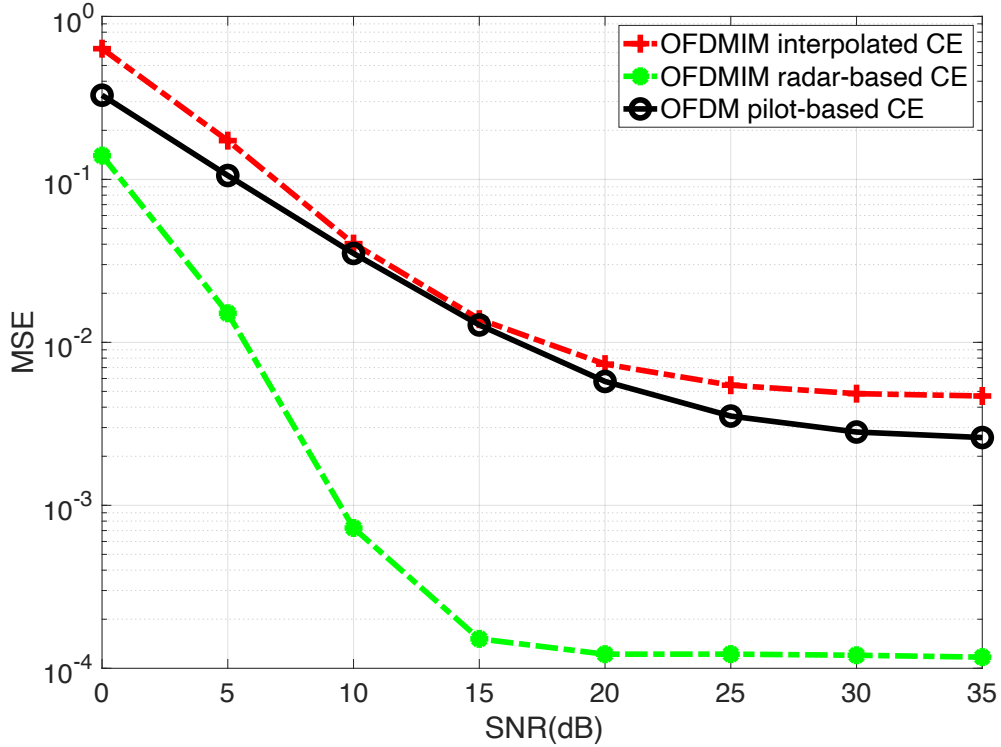


Figure 4.16: MSE vs SNR analysis under three targets. Targets are with velocities $[0, 0, 14.9]$ (m/s) and distances $[39, 136.6, 234.2]$ (m).

η denotes the normalization factor and p is the target index. Each tap amplitude follows Rayleigh distribution.

After evaluating the complex attenuation factor α_p in (4.27), the estimation of channel matrix $\hat{\mathbf{H}}^f$ is performed by using the obtained values of Doppler shifts and delays which is done previously via radar symbols on OFDM-IM. Finally, these estimates are used to demodulate communication symbols in the proposed OFDM-IM waveform structure. MSE is calculated with $\hat{\mathbf{H}}^f$ and \mathbf{H}^f matrices, $\sigma_e^2 = \frac{\mathbb{E}[\|\hat{\mathbf{H}}^f - \mathbf{H}^f\|^2]}{\mathbb{E}[\|\mathbf{H}^f\|^2]}$, where $\mathbb{E}[\cdot]$ denotes the expected value.

The proposed scheme is compared with the conventional OFDM scheme where the channel estimation is done with comb-type pilot arrangements explained in [82]. It is well known that the minimum MSE is obtained when the pilots are equispaced (comb type arrangement), when the MSE of the least-square (LS) estimation is utilized. Also, the use of the

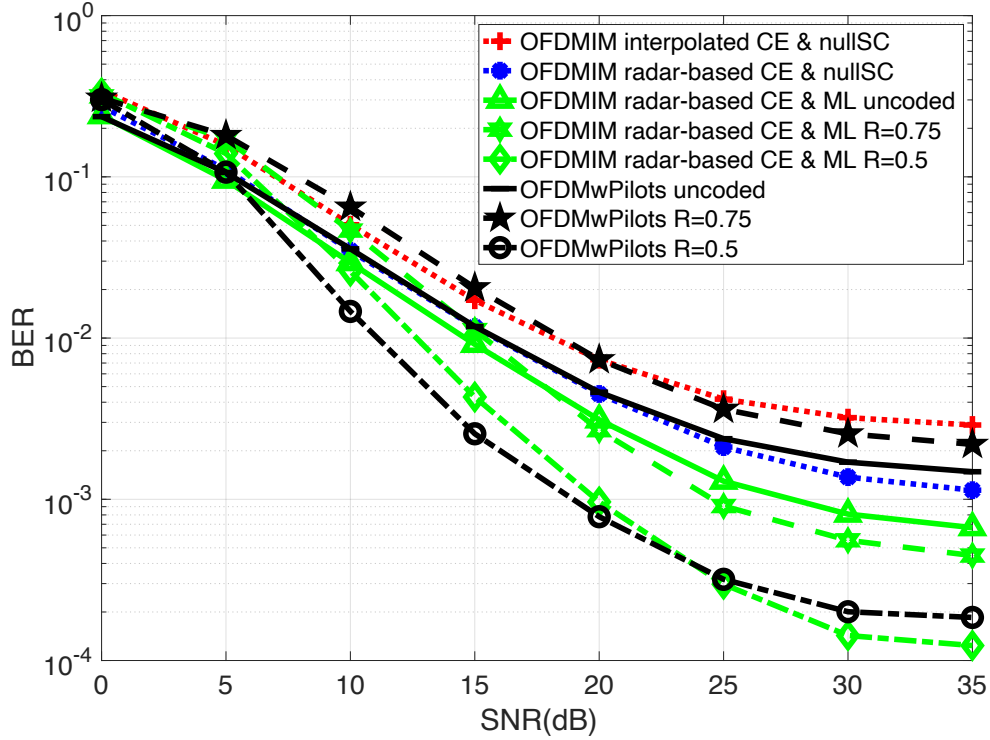


Figure 4.17: BER vs SNR analysis under three targets. Targets are with velocities $[0, 0, 14.9]$ (m/s) and distances $[39, 136.6, 234.2]$ (m).

same subcarriers for pilot allocation among subsequent OFDM symbols is widely used pilot arrangement scheme [82]. Simple LS estimate is employed to find initial channel estimates on pilot subcarriers, where the correlation across the OFDM carriers and OFDM symbols is not exploited. The channel frequency response (CFR) vector is obtained by implementing linear interpolation over all pilots. This is followed by the replacing the samples after the length of the CP with zeros in the time domain by taking IFFT. The noise reduced signal is then transformed back into the frequency domain via FFT operation to obtain the estimated value of the channel over each OFDM symbol. The number of pilots and symbols, subcarrier spacing(Δf) used in conventional OFDM for comparison are the same as proposed OFDM-IM JCR structure. Figure 4.14 and 4.15 illustrates the radar functionality of the proposed scheme compared to conventional OFDM when SNR is 10 dB. It is obviously seen in Figure 4.14 that a fixed pilot design limits the unambiguous radar range, where as it is not the case in the proposed scheme as seen in Figure 4.15.

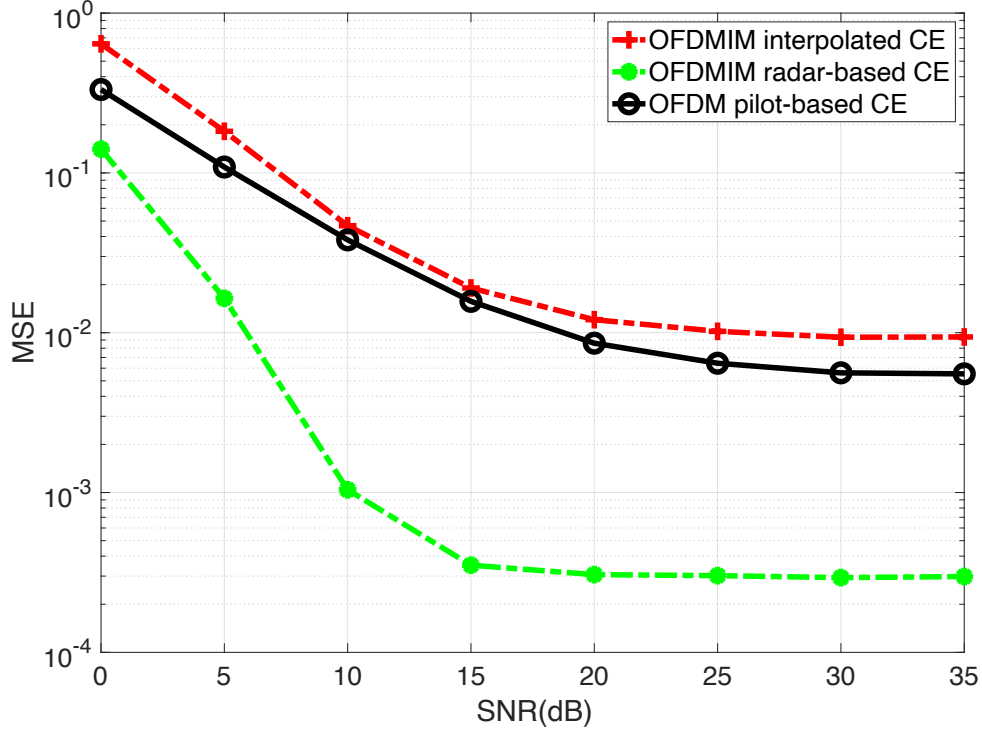


Figure 4.18: MSE vs SNR analysis under four targets. Targets are with velocities $[0, 14.9, 21.2, 30.6](\text{m/s})$ and distances $[29.3, 127.3, 225.3, 323.3](\text{m})$.

Figure 4.16 and 4.17 shows the performance analysis for two stationary and one moving targets and their respective distances. In Figure 4.16, conventional OFDM JCR with comb-type pilot arrangement, OFDM-IM with interpolation of irregularly spaced pilots, and the proposed radar-based OFDM-IM waveform is compared considering their MSE of channel estimation. It can be observed that the proposed scheme significantly outperforms the two existing conventional schemes. As a channel decoder to perform BER simulations, LDPC (low-density parity check) is used with two different rates, which are 0.5 and 0.75. Figure 4.17 shows the benefit of the proposed scheme in terms of error performance compared to conventional OFDM with pilots. It also compares the proposed OFDM-IM JCR scheme with two different decoding types such as the null subcarrier based and ML-based decoding explained in Section 4.3.3. It can be observed that our scheme outperforms the conventional schemes in both detection methods. The ML based scheme provides a better error perfor-

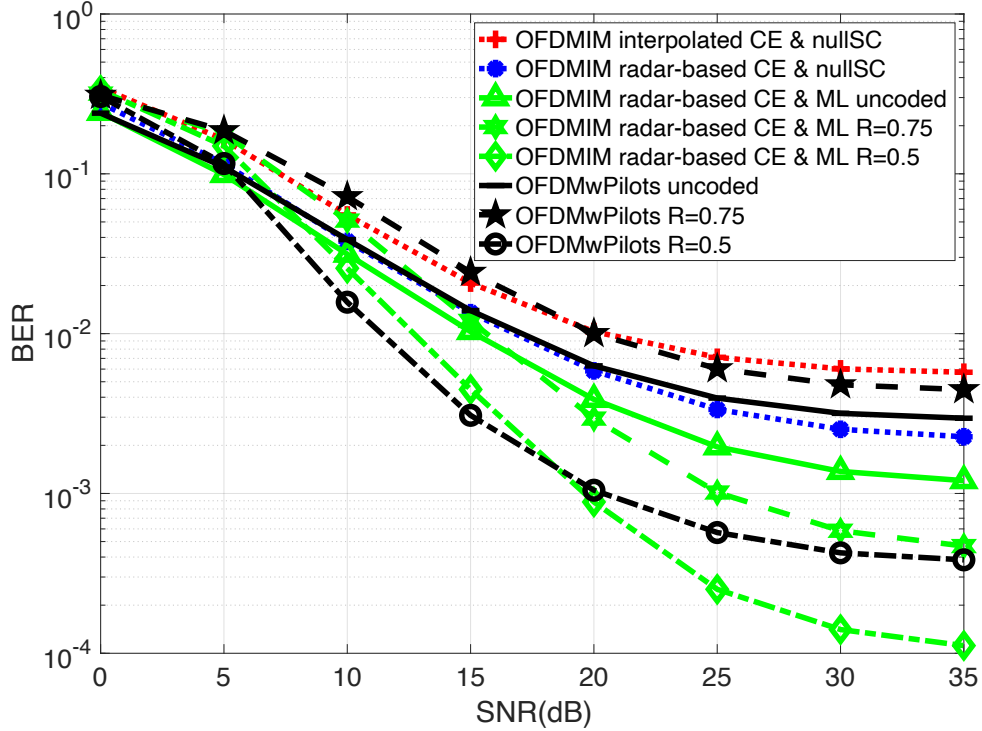


Figure 4.19: BER vs SNR analysis under three targets. Targets are with velocities $[0, 14.9, 21.2, 30.6](\text{m/s})$ and distances $[29.3, 127.3, 225.3, 323.3](\text{m})$.

mance when compared to the proposed null-based decoding however, it has a much higher complexity.

Figures 4.18 and 4.19 show the performance analysis for one stationary and three moving targets and their respective distances. The conventional OFDM scheme reaches error floor at $\sim 10^{-3}$ BER, whereas proposed scheme exhibits promising performance reaching beyond 10^{-4} BER. There exists a trade-off between complexity and performance for ML detection over null subcarrier based detection. It is observed that, since there are more active targets in Figures 4.18 and 4.19, due to multiple Doppler effects, the performance of the conventional OFDM scheme degrades. However, the performance of the proposed OFDM-IM JCR scheme keeps same as Figure 4.17 claiming the superiority of the proposed scheme against high Doppler. Also, it should be noted that the conventional OFDM with 0.75 code rate performs worse than uncoded system in Figures 4.17 and 4.19. It is the case because we do not implement interleaving after encoding the bit sequence for both conventional OFDM JCR scheme and

proposed OFDM-IM JRC scheme. It is can be seen that the proposed OFDM-IM performs better and index bits inherently introduce diversity over one OFDM-IM symbol.

In this study, a novel JCR waveform utilizing OFDM-IM and its promising properties has been proposed. The system model description along with numerical and computational evaluations have been provided. Computer simulations show that the proposed scheme provides improvement not only in error performance for communication but also enhanced radar performance when compared to OFDM-JCR schemes in terms of BER and MSE performance. Also, it is shown that the proposed scheme increases the maximum unambiguous radar range compared to conventional OFDM with comb-type pilot design. For future research direction, generalization of the proposed OFDM-IM scheme for different subblock and active subcarrier numbers will be studied.

Chapter 5: Control of Electromagnetic Radiation on Coexisting Smart Radio Environment

This chapter⁴ explains the novel proposed coexisting smart radio environment to control and guide the electromagnetic radiation.

5.1 Introduction

The 5G wireless communication networks is proposed to enable three imperative service applications which are massive machine type communication (mMTC), enhance mobile broadband (eMBB), and ultra reliable, low latency communication (URLLC). With the recent developments on key 5G technologies such as massive MIMO, polar coding, cloud radio access network (C-RAN), and so on, the theoretical gain is achieved to be validated by the field test [96]. However, as intelligence, autonomy and ubiquity of digital world exponentially grow, 5G wireless networks will not be adequate to meet high demand of future applications that need connection of everything consisting of people, vehicles, UAVs, satellites, sensors, data clouds, computing devices and robotic agents [97].

5.1.1 Vision for 6G

It is expected that 6G wireless networks will fulfill the fully connected digital world and provide ubiquitous wireless connectivity for all. It will open a new era of Internet of intelligence with connected everything [98]. With the emergence of holographic teleportation, increased industrial automation and connection density, next generation 6G systems are needed to possess Tbps-level data rates, microsecond-level latency, improved energy ef-

⁴Contents of the chapter is published in [95]. Permissions are included in Appendix A.

efficiency [99]. Also, industrial Internet of Things (IIoT) concept requires wireless networks guaranteeing spatial reconfigurability and ultra-reliability [100]. With the diverse requirements of emerging applications and use cases, it is believed that 6G systems is intended to enhance the awareness of the whole communication networks including wireless medium and end-points [101]. Such massively connected network needs to have capabilities of real-time learning and data processing for network edges, air interface and user elements that can be enabled via machine learning (ML) [102].

The increase in the number of wireless devices that is expected to reach 125 billion devices all over the world by 2030 [97] and the aim of 1Gb/s/m² area traffic capacity [103] boost the importance of spectrum utilization for the next generation wireless systems in the highly overloaded coexisting scenarios. Also, current wireless communication systems cannot provide services to half of the world's population living in remote areas [104] where next generation systems are planned to guarantee at least 10 Mbps by extending the coverage area. Therefore, the electromagnetic radiation emitting from numerous wireless devices serving various applications needs to be controlled intelligently both in the transceiver ends and along the wireless medium. Therefore ultra-advanced spectrum usage and management schemes in licensed and unlicensed band need to embrace all disruptive and smart technologies such as RIS, ABC and ML.

5.1.2 Shifting from Cognitive Radio to Smart Radio Environment

Since the birth of cognitive radio by J. Mitola [105] and the extreme success of coexisting wireless systems (e.g. WiFi, Bluetooth, and other devices), wireless technology could dynamically utilize the spectrum and high-spectral waveforms by mitigating interference to primary passive/active users [106]. Cognitive radio networking (CRN) emerges as an effective way to design the coexisting wireless communication systems offering potential for enhanced spectrum efficiency, interference mitigation and interoperability [107]. CRN only controls the parameters of end-to-end radios by sensing the environment and smartly

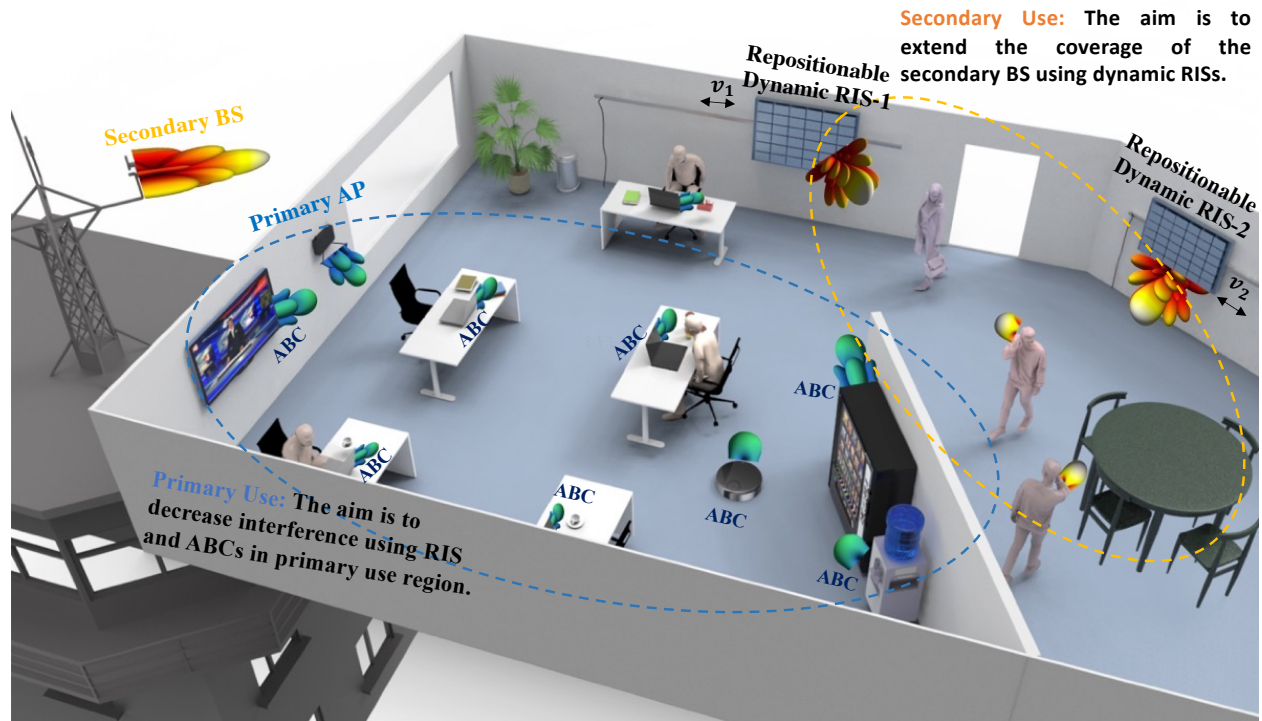


Figure 5.1: Shaping the electromagnetic energy using repositionable dynamic RISs and ABC nodes. ABC nodes are designed to be application specific devices. RISs may operate across in a wide frequency band regime for coarse tuning the radiation of secondary systems.

adjusting relevant transmission and reception parameters [108]. Beside cognitive capabilities on the transmitter and receiver end, effective co-existing wireless communication systems demand a disruptive system design and radio frequency (RF) implementation to maximize the spectrum utilization by keeping extremely high radio rejection to avoid interference [109]. For example, in the light of many potential co-existing frequency bands such as those for commercial radio communication reception whose signal strength may be around -70 dBm to -120 dBm and advanced interference mitigation techniques over the whole area are needed to capture the signal safely. Such a technology challenge, which leads to controlling radio radiation on a geographical area, has not been well addressed in literature or engineering patents beyond personal area. Also, how to maximally utilize the spatial spectrum and radiation control according to traffic dynamics in time and spatial domains remains the key challenge for future application scenarios that require high capacity (e.g., holography, virtual

reality, non-terrestrial communication), high density (e.g., IoT environment in smart factories and smart offices) and high precision (e.g., robotic assembly and warehouse stocktaking).

Shaping the radiation energy and nulls over the region, together with time, frequency, code domains presents a holistic approach toward smart and reconfigurable radio environments, for more effective spatial spectrum utilization of co-existing wireless systems and networks. A fundamental question arises on how to evolve into coexisting wireless system from spectrum efficiency perspective by taking network infrastructure design into consideration [106]. To answer that, the paradigm of smart radio environment is firstly introduced in [110] and detailed in [111] which is empowered by the RIS. It is motivated that future wireless networks necessitate a smart radio environment with RIS which are capable of sensing the environment and of applying customized transformations to the electromagnetic radio waves. Also, smart radio environments provides more degrees of freedom by electronically controlling the environment itself rather than transmitter and receiver end points and turns the wireless medium into software-reconfigurable entity [112]. Secure wireless transmission, interference reduction, transmission range extension can be considered as some of smart radio environment applications [113].

In this study, the smart radio environment concept is enriched with the harmony of multiple repositionable dynamic RISs and coordinated ABCs to extend the geographical coverage (by eliminating spectrum holes) and maximize the sum rate throughput for a given geographical region and a given spectrum, while enhancing geographical isolation and minimizing the interference of underlay coexisting cognitive radio networks. In addition to providing controllable reflection properties with RISs [114, 115] and ABC nodes [116], the mobility of these devices in the environment is proposed to further enhance the system performance. The proposed coexisting smart radio environment strategy illustrated by Figure 5.1 will achieve multiple goals including interference management, coverage improvement, enhanced radio environment awareness (REA), effective spectrum mapping and intentional geographical ra-

dio isolation that could potentially revolutionize the spatial spectrum efficiency of systems migrating from 5G's C-RAN and massive MIMO to 6G.

5.1.3 Contribution

This research aims to enable smart radio environment by merging two appealing technologies repositionable dynamic RIS and ABC, that helps to maximize the spatial spectrum utilization for cognitive radio systems where two different wireless system applications called primary and secondary uses are present as shown in Figure 5.1. The main contributions of the study can be summarized as follows:

- The smart radio environment system is proposed utilizing repositionable dynamic RIS and multiple coordinated ABC to control spatial electromagnetic radiation by creating radiation rejection and coverage extension zones.
- To the best of our knowledge, it is novelly introduced that the repositionable dynamic RISs are utilized to extend the coverage of co-existing secondary systems and coarse radiation rejection for primary systems by having much more control on the exploitation of channel clusters as well as shadowing effects that may causes high power fluctuations in a short time frame.
- It is also first time that a group of coordinated ABC nodes are proposed to create man-made deep fades which greatly reduce the interference from secondary use into the radiation rejection zone hosting primary passive and active uses.
- Construction of spectrum map by cross-layer RF design and support vector machine (SVM) based on 1-bit spectrum sensor data is introduced by novel reusing of ABC to transmit the data to distributed fusion center (DFC).
- The coexistence of all proposed concepts is studied with joint optimization of coverage extension area and radiation rejection zone using both repositionable dynamic RIS

and multiple ABCs. Alternation optimization technique is utilized by subgrouping the general problem into smaller ones. The convergence of the proposed technique is evaluated with numerical study as well.

The unique rationale of this study is therefore to create extended, controlled radiation of the secondary systems in the 2D/3D geographical area as shown in the Fig. 5.1, while creating the radiation-rejection zone to ensure the successful operation of the primary systems. The system architecture of the proposed coexisting wireless communications can be visualized in Figure 5.2. As extremely large antenna arrays approaching the limit of massive MIMO, the aim is to steer electromagnetic radiation while creating man-made radio rejection to protect primary passive or active users. Such a system architecture has a large-scale antenna-array for an access point (AP) or BS, while smaller-scale antenna arrays tagged to each user equipment or smart machine (*e.g.* robot or autonomous vehicle) which function as backscatterer to create a radiation rejection zone. Moreover, multiple repositionable dynamic RISs advanced by RF/antenna techniques to extend and tailor the geographical coverage (in reliability and outage), such that the interference to/from the underlay coexisting radio systems can be minimized. Multiple coordinated ABC nodes for fine-tuning of radio coverage by forming radiation rejection to avoid interference to sensitive primary passive/active users, which is named as virtual region and circled with red curve in Figure 5.2. The mmWave geometric channel model is utilized to demonstrate the feasibility of the system architecture, where SNR and capacity performance on the measurement points (MPs), which are distributed in the whole geometry, are numerically calculated. In the presented numerical studies, it is shown that these mechanisms allow to create regional shapes where radiated power is distributed as desired.

It is demonstrated that at least 5 dB increase can be obtained in the power of secondary system along the specific region by introducing multiple static coordinated RIS. Moreover, the superiority of repositionable dynamic RIS is represented with the increment of nearly 15% in the capacity of the secondary system. Additionally, simulation results demonstrates

that the use of coordinated multiple ABC nodes provides nearly 10 dB interference rejection in the vicinity of primary user. The proposed architectures is merged into one system and optimizes the parameters to enable smart radio environment having radiation rejection and coverage extension zones at the same time. The use of SVM to spatially identify the secondary communication area by 1-bit data transmitted from ABC sensor is illustrated.

5.2 Multiple RIS to Extend the Coverage of Secondary Systems

5.2.1 State of the Art

The mmWave band usage is significantly investigated regarding next-generation wireless communications [117], which allows very small form-factor antenna arrays for both BS and the UEs [118] and provides highly efficient directional transmissions to meet the high capacity demand of future wireless technologies [119]. However, energy losses in mmWave band channel are more susceptible to the propagation distance compared to the classical sub-3 GHz band [120]. The prominent technology, RIS, is proposed as a channel control mechanism which converts the channel from a problem into a design elements [121]. It can achieve a controlled and narrower beams at larger sizes relative to the wavelength [122] in order to overcome the energy loss problem in mmWave channels. Unlike relays, RIS consumes no energy resulting in less noise effect. However, as shown in a comparison of RIS to decode and forward relaying in [123], RIS is required to have many elements to outperform relaying since it has no power source. In both the RIS and multiple-antenna systems, one major challenge is the channel estimation and synchronization due to the large number of passive elements in a RIS. However, the sparseness of mmWave channels allows feasible and efficient synchronization and channel estimation algorithms. Using few active elements along the RIS for channel estimation is proposed in [124], and after estimating the channel, these active elements turn back to the reflecting mode again. For instance, a two stages algorithm is proposed in [125] for multi-user communication, where all elements are turned off firstly, and the channel between BS and users is estimated. Secondly, the RIS elements are turned

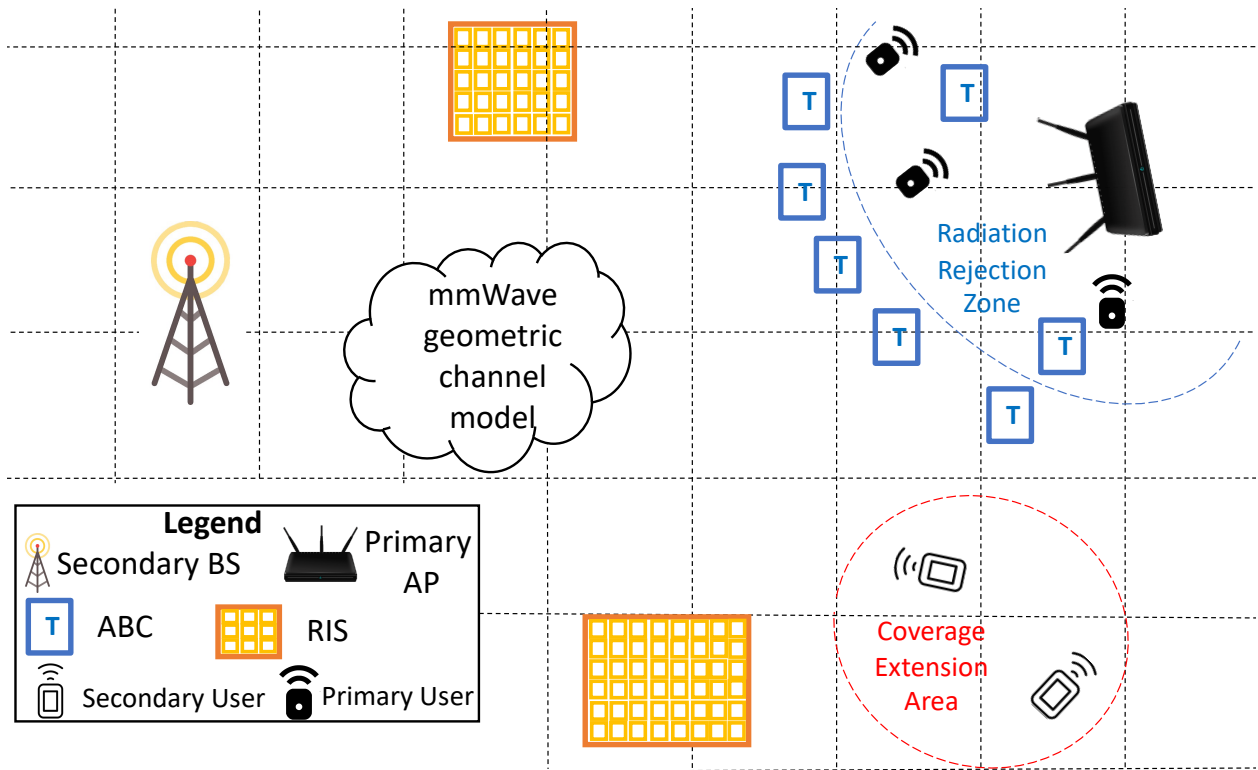


Figure 5.2: System structure including multiple RISs for coverage extension, multiple coordinated ABCs for radiation rejection.

on one by one and the channel of all users is estimated for that element. The full reflection of the RIS is considered at all time, i.e., all of its elements are switched ON with maximum reflection amplitude during both the channel estimation and data transmission phases [126]. It is inevitable fact that as the channel estimation and optimization schemes of the RIS develop, the usage of the RIS in modern wireless systems will expand.

5.2.2 System Model

The RIS smartly controls the radio environment by scattering the signals to mitigate pathloss, fading, blockage, and multipath effects. It is typically configured to direct the primary system signal towards the destination by adapting its antenna elements to the propagation environment, while being regarded as nearly passive elements without any need for amplifiers or analog-to-digital/digital-to-analog converters (ADCs and DACs). This research disruptively utilizes the RIS to extend the coverage area of secondary systems and

to decrease the interference in the vicinity of primary systems as the goal of Figure 5.1. To extend the coverage of secondary active uses, two RISs are illustrated to create the smart radio environment in Figure 5.2. To protect the zone which can be passive or active primary use, multiple ABCs are placed around the primary use area.

Omnidirectional pathloss at the distance d is estimated using the d_0 reference distance for the antenna far-field as follows [127]:

$$\text{PL}(d)[\text{dB}] = \text{PL}(d_0) + 10\bar{n} \log_{10} \left(\frac{d}{d_0} \right) + SF, \quad (5.1a)$$

$$\text{PL}(d_0)[\text{dB}] = 20 \log_{10} \left(\frac{4\pi d_0 f_c}{c} \right), \quad (5.1b)$$

where c is the speed of light, $3 \times 10^8 \text{m/s}$, f_c in Hz is the carrier frequency, \bar{n} is the path loss exponent, and SF is the shadow factor in dB. The far-field path-loss equation in (5.1) is compatible with the pathloss expression given in [128]. Also, outdoor-to-indoor penetration loss is considered assuming the environment has low loss buildings. Therefore, the following parabolic model [129] is used for building penetration loss (BPL):

$$\text{BPL}[\text{dB}] = 10 \log_{10} (5 + 0.03 \cdot f_c^2). \quad (5.2)$$

Throughout the study, the narrow-band mmWave channel model is used. It is assumed that all clusters and multi-path components arrive simultaneously and all their frequency components over the channel bandwidth B are received with the same level of attenuation. The corresponding channel matrix $\mathbf{H} \in \mathbb{C}^{N_r \times N_t}$ at the time instant t is written as follows [120]:

$$\mathbf{H} = \sum_{n_{cl}=1}^{N_{cl}} \sum_{p=1}^{N_p(n_{cl})} \alpha_{n_{cl},p} \cdot \Omega_{n_{cl},p}^{R_x} (\psi_{n_{cl},p}^{R_x}, \theta_{n_{cl},p}^{R_x}) \cdot \Omega_{n_{cl},p}^{T_x} (\psi_{n_{cl},p}^{T_x}, \theta_{n_{cl},p}^{T_x})^H, \quad (5.3a)$$

$$|\alpha_{n_{cl},p}|^2 = \epsilon_0 e^{\frac{-T_{n_{cl}}}{-T_{n_{cl}}}} e^{\frac{-\tau_{n_{cl},p}}{-T_{n_{cl}}}} 10^{-0.1(\text{PL}[\text{dB}] + \text{BPL}[\text{dB}] + Z_{cl} + U_p)}, \quad (5.3b)$$

where N_{cl} and $N_p(n_{cl})$ denote the number of clusters and rays per each cluster, respectively. $Z_{cl} \sim N[0, \sigma_{cl}]$ and $U_p \sim N[0, \sigma_p]$ denote per-cluster and per-subpath shadowing in dB, respectively. $T_{n_{cl}}, \tau_{n_{cl},p}, \Gamma_{n_{cl}},$ and Γ_p correspond to cluster arrival time, subpath arrival time, cluster decay constant, and subpath decay constant, respectively. The parameters $\psi_{n_{cl},p}$ and $\theta_{n_{cl},p}$ are p th multi-path component of the n_{cl} th cluster's azimuth and elevation angles, respectively, and they characterize the angle-of-departure (AoD) and angle-of-arrival (AoA) at the transmitter and receiver. Moreover, $\Omega_{n_{cl},p}^{Tx}$ represents the $N_t \times 1$ array factor (AF) of the transmitter antenna array and $\Omega_{n_{cl},p}^{Rx}$ represents the $N_r \times 1$ AF of the receiver antenna array. The notation $(\cdot)^H$ refers to the Hermitian transpose. The notations for the RIS presented here are also used to clarify the subsequent sections, as well. Define a diagonal matrix $\Theta_{RIS_k} = \text{diag} \left(\beta_1 e^{j\theta_1}, \dots, \beta_{n_{RIS_k}} e^{j\theta_{n_{RIS_k}}}, \dots, \beta_{N_{RIS_k}} e^{j\theta_{N_{RIS_k}}} \right)$ with $k = 1, \dots, K$, where K is total number of the RIS deployed in the environment. The notation N_{RIS_k} denotes for the total reflecting elements in the k th RIS, $\beta_{n_{RIS}}$ is the amplitude reflection coefficient of the n_{RIS} th element of k th RIS and j is the imaginary unit. Throughout the study, the reflection coefficient is assumed to be unit value ($\beta_{n_{RIS_k}} = 1$), same as in [130]. The b_{RIS} -bit discrete phase shift of RIS antennas can be chosen from the set \mathcal{F}_{RIS} which is defined as follows [131]:

$$\mathcal{F}_{RIS} = \left\{ \theta_{n_{RIS_k}} = \frac{\varsigma_{n_{RIS}} \pi}{2^{b_{RIS}} - 1} \mid \varsigma_{n_{RIS}} \in \mathfrak{S}_{RIS} = \{0, 1, \dots, 2^{b_{RIS}} - 1\} \right\}. \quad (5.4)$$

Uniform planar array (UPA) is utilized to represent RISs. Denote l_r and l_c the number of elements along with the row and column of the plane array, then the array response vector becomes the following [132]

$$\Omega_{UPA}(\psi, \theta) = [1, \dots, e^{jx(i_r \cos(\psi) \cos(\theta) + i_c \sin(\theta))2\pi/\lambda}, \dots], \quad (5.5)$$

where x is the inter-element spacing. $0 \leq i_r < l_r$ and $0 \leq i_c < l_c$ are the row and column indices of an antenna element, respectively. Analog beamforming is considered at the transmitter antenna array, where N_{BS} is the total number of antennas. Transmitter antenna

array is considered as more complex compared to RIS elements, therefore, its phase shifter can generate more options with the control of b_{BS} bits. Then, the phase shift for the n_{BS} th transmit antenna can be chosen from the set \mathcal{F}_{BS} where

$$\mathcal{F}_{\text{BS}} = \left\{ \theta_{n_{\text{BS}k}} = \frac{\varsigma_{n_{\text{BS}}}\pi}{2^{b_{\text{BS}}}-1} \mid \varsigma_{n_{\text{BS}}} \in \mathfrak{S}_{\text{BS}} = \{0, 1, \dots, 2^{b_{\text{BS}}}-1\} \right\}. \quad (5.6)$$

After the selection of n_{BS} th antenna phase shift the beamforming matrix \mathbf{W} is formed with power constraint \mathcal{P} . In the smart radio environment, spatial consistency is considered [133] which means that the large fading effects and scattering environment are correlated when multiple MPs are closely located in a local area (e.g. 10-15 m). Detailed explanation regarding how to integrate spatial consistency into the channel model is included in the next section. It should also be mentioned that perfect CSI is assumed throughout out the study for both RIS and ABC phase shift optimization, which is similar to [134, 135].

5.2.3 Problem Formulation for Coverage Extension

In this subsection, the problem formulation to extend the coverage of secondary system via multiple static RISs is derived. In order to perform spatial-domain based simulations, multiple MPs are selected randomly which can be considered as many single antenna receivers. Since the coverage inside the specific area is desired to be increased, these measurement points are selected inside that area. The 2D demonstration of the simulation can be seen in Figure 5.3 and 5.5, where the area, whose capacity for the secondary is intended to increase is shown by red circle.

The overall RIS-assisted MIMO system have three main propagation ways which are between Tx and the RIS, the RIS and Rx and direct way, which is assumed as non-line-of-sight (LOS) (NLOS) channel. Regarding the channel matrices, $\mathbf{H}_{\text{BS-MP}_m}$, $\mathbf{H}_{\text{BS-RIS}_k}$, and $\mathbf{H}_{\text{RIS}_k\text{-MP}_m}$ correspond to the channels between BS and m th MP, BS and k th RIS, k th RIS and m th MP, respectively. Analog beamformer matrix $\mathbf{W} \in \mathbb{C}^{N_{\text{BS}} \times 1}$ is applied at the transmitter

antenna array having N_{BS} antennas with total power P . As an example with two RIS, the channel matrices for the m th MP are $\mathbf{H}_{\text{BS-MP}_m} \in \mathbb{C}^{1 \times N_{\text{BS}}}$, $\mathbf{H}_{\text{BS-RIS}_1} \in \mathbb{C}^{N_{\text{RIS}_1} \times N_{\text{BS}}}$, $\mathbf{H}_{\text{RIS}_1\text{-MP}_m} \in \mathbb{C}^{1 \times N_{\text{RIS}_1}}$, $\mathbf{H}_{\text{BS-RIS}_2} \in \mathbb{C}^{N_{\text{RIS}_2} \times N_{\text{BS}}}$, and $\mathbf{H}_{\text{RIS}_2\text{-MP}_m} \in \mathbb{C}^{1 \times N_{\text{RIS}_2}}$ where N_{RIS_1} and N_{RIS_2} denote the numbers of elements for the first and second RISs. Moreover, phase matrices are $\mathbf{\Theta}_{\text{RIS}_1} \in \mathbb{C}^{N_{\text{RIS}_1} \times N_{\text{RIS}_1}}$, and $\mathbf{\Theta}_{\text{RIS}_2} \in \mathbb{C}^{N_{\text{RIS}_2} \times N_{\text{RIS}_2}}$ for the first and second RISs, respectively. The channel gain, G_m , for the m th MP with the presence of total K RISs can be represented as follows [121]:

$$G_m = \left| \mathbf{H}_{\text{BS-MP}_m} \mathbf{W} + \sum_{k=1}^K \mathbf{H}_{\text{RIS}_k\text{-MP}_m} \mathbf{\Theta}_{\text{RIS}_k} \mathbf{H}_{\text{BS-RIS}_k} \mathbf{W} \right|^2. \quad (5.7)$$

Assuming transmit power equals to 0dBm, capacity of the m th MP is evaluated by Shannon capacity formula:

$$R_m = B \log_2 \left(1 + \frac{G_m}{\sigma^2} \right), \quad (5.8)$$

where B is the bandwidth and σ^2 is the variance of independent and identically distributed (i.i.d) circularly symmetric complex Gaussian noise with zero mean. Let $\mathbf{R} = [R_1, R_2, \dots, R_M]$ and $\mathbf{\Theta}_{\text{RIS}} = [\mathbf{\Theta}_{\text{RIS}_1}, \dots, \mathbf{\Theta}_{\text{RIS}_K}]$, the optimization problem can be formulated as follows [136]:

$$\begin{aligned} (P1) \quad & \max_{\mathbf{\Theta}_{\text{RIS}}, \mathbf{W}} \quad \mathbb{E}\{\mathbf{R}\} \\ & \text{s.t.} \quad \|\mathbf{W}\|^2 \leq P \\ & \quad \theta_{n_{\text{BS}_k}} \in \mathcal{F}_{\text{BS}}, \quad 1 \leq n_{\text{BS}_k} \leq N_{\text{BS}_k} \\ & \quad \theta_{n_{\text{RIS}_k}} \in \mathcal{F}_{\text{RIS}}, \quad 1 \leq n_{\text{RIS}_k} \leq N_{\text{RIS}_k}, \end{aligned} \quad (5.9)$$

where \mathbb{E} is the expectation operator over M total MP. As it is studied in [137], the optimization problem (5.9) is non-convex. Alternating optimization technique, as it is proposed in [138], is utilized to arrange the phase shifts of the BS and RISs at MPs as a solution to (5.9). The procedure of this iterative technique is explained in Algorithm 5.1.

Algorithm 5.1 Alternating Optimization for (5.9)

- 1: Initialize the all elements of \mathbf{W} , and $\theta_{n_{\text{RIS}_k}}, 1 \leq n_{\text{RIS}_k} \leq N_{\text{RIS}_k}, \forall k = 1, \dots, K$ with one.
 - 2: **repeat**
 - 3: **for** $n \leq N_{\text{BS}} + \sum_{k=1}^K N_{\text{RIS}_k}$ **do**
 - 4: Find the indices $\varsigma_{\text{BS}} \in \mathfrak{S}_{\text{BS}}$ and $\varsigma_{\text{RIS}_k} \in \mathfrak{S}_{\text{RIS}}$ that maximize the average capacity of total M MPs, which defined as $\mathbb{E}\{\mathbf{R}\}$
 - 5: Assign the corresponding phase shift values depending on the index ς_{BS} or ς_{RIS_k} to the corresponding antenna phase shifter n
 - 6: **end for**
 - 7: **until** Convergence is reached
-

5.2.4 Numerical Results

The numerical results demonstrates the advantage of deploying multiple static RISs to expand the coverage of the secondary active uses. The 2D topological color map in Figure 5.3 and 5.5 show the performance of RISs compared to BS beamforming in order to maximize the signal power in the red encircled area of 15 MPs in terms of dB. The secondary user (SU) is located at (0,0) and denoted as black star, whereas the primary user (PU), which is white star, is located at (0,120).

Information about other simulation parameters can be found in Table 5.1. In Figure 5.3, only BS beamforming is utilized to extend the coverage on the area encircled with red color. Enlarged picture of the encircled region is shown as well. In Figure 5.5, two RISs are denoted as magenta circles which are distributed in the map. MPs use the single-element antenna where phase shifts of RISs are arranged to maximize the average capacity of all MPs as formulated in (5.9).

Throughout the mathematical simulations of the study, it is assumed that RISs has two different phase options controlled by one-bit, whereas the phase options for BS antennas are chosen from the six-bit discrete phase-shifter. They all are optimized in an iterative manner until convergence is achieved by Algorithm 5.1. In this urban-microcell simulation, the BS antenna number is taken as $N = 16$ and the numbers of elements for first RIS and second RIS are 128 and 256, respectively. The signal power in the encircled area by BS beamforming

Table 5.1: Simulation Parameters for Coverage Extension

Parameter	Value
Carrier Frequency	28 GHz
Antenna gain of BS	30 dB
Transmitter gain of BS	10 dB
Antenna gain of ABC	15 dB
Operating Scenario	Urban Microcell
BS Antenna Number	16
RISs Element Numbers	128, 256
ABCs Antenna Number	4x4 (both Rx, Tx)
Number of total ABCs	16

can be seen in Fig. 5.3, whereas the effect of RISs can be seen in Fig. 5.5. As shown in the enlarged plots, simple usage of two RISs already achieves approximately 6 dB gain regarding the signal power of secondary user even if there is 1 bit control on RIS. It is well known that the number of bits in the RIS design, and the location of RIS remarkably affect the performance in the coverage area. These effects are studied in the following section.

5.3 Repositionable Dynamic RIS Deployment

5.3.1 State of the Art

It is studied that the location, beam alignment, and phase of the RIS can be optimized to enhance the system performance [139, 140]. Although the current RIS technology primarily deploys fixed elements built in the terrestrial scenarios, the integration of RIS into mobile systems gets a lot of interest from the academia. For example, reference [141] studies aerial platforms with RIS and propose a control mechanism for communication, mobility, and sensing. Additionally, joint optimization of active beamforming at the UAV, passive beamforming at the RISs, and UAVs trajectory over a given flying time is studied in [142]. However, locations of the RISs are assumed as fixed and only the movement of UAV is considered. Therefore, the control over the channel clusters is limited.

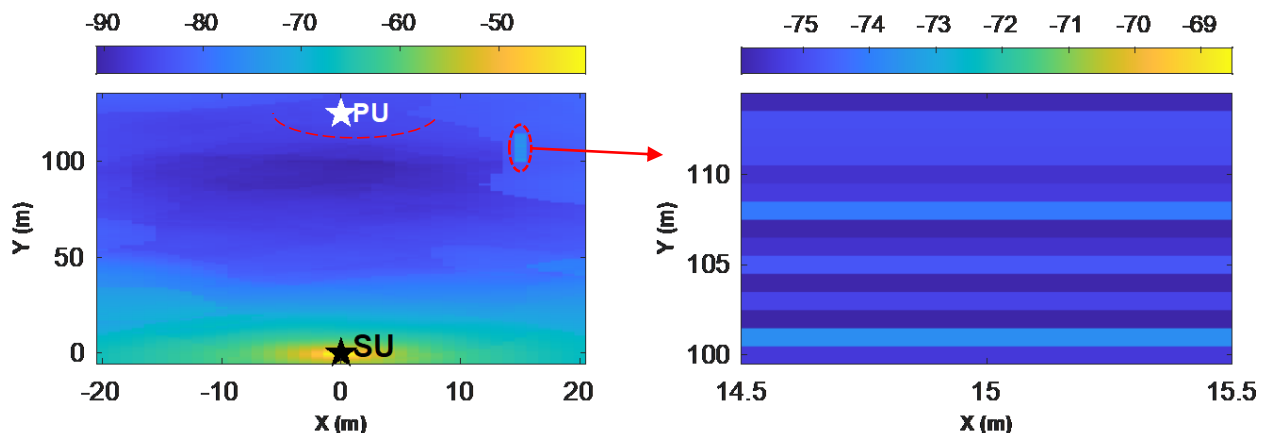


Figure 5.3: Demonstration of coverage extension when only BS is used to extend where the color map is scaled in dB.

It is known that glitches occur in the power of "pencil-beam" signal whenever even humans walk across it resulting in a huge SNR drop of 20dB [143]. This scenario can be encountered in shopping malls, office environments and especially IoT factories where tactile internet plays a very important role. To the best of authors knowledge, a wireless channel control concept based on position adaptive antenna array is firstly introduced by the USF-WAMI team [144, 145] in order to impede detrimental random effects in the wireless channel. In these studies, the concept is implemented via the microfluidically reconfigurable RF devices. Moreover, it is also known that positioning of RIS plays an important role to improve the system performance [146]. However, dynamic positioning of RIS regarding the mobility in the indoor environment hasn't studied yet. Arranging the RIS position dynamically, we will have much more control on exploitation of channel clusters as well as shadowing effects that may causes high power fluctuations in a short time frame. It is believed that the repositionable dynamic RIS will shed a light on how to solve these problems and introduce additional degree of freedom.

Applying repositionable dynamic RIS, the channel control could be more efficient by placing the RIS elements at the optimal location. In addition to the phases of the RIS elements, the location of the surface needs to be optimized. For mobile and nomadic users, the optimal location changes over time, requiring repositionable dynamic RIS deployment. As

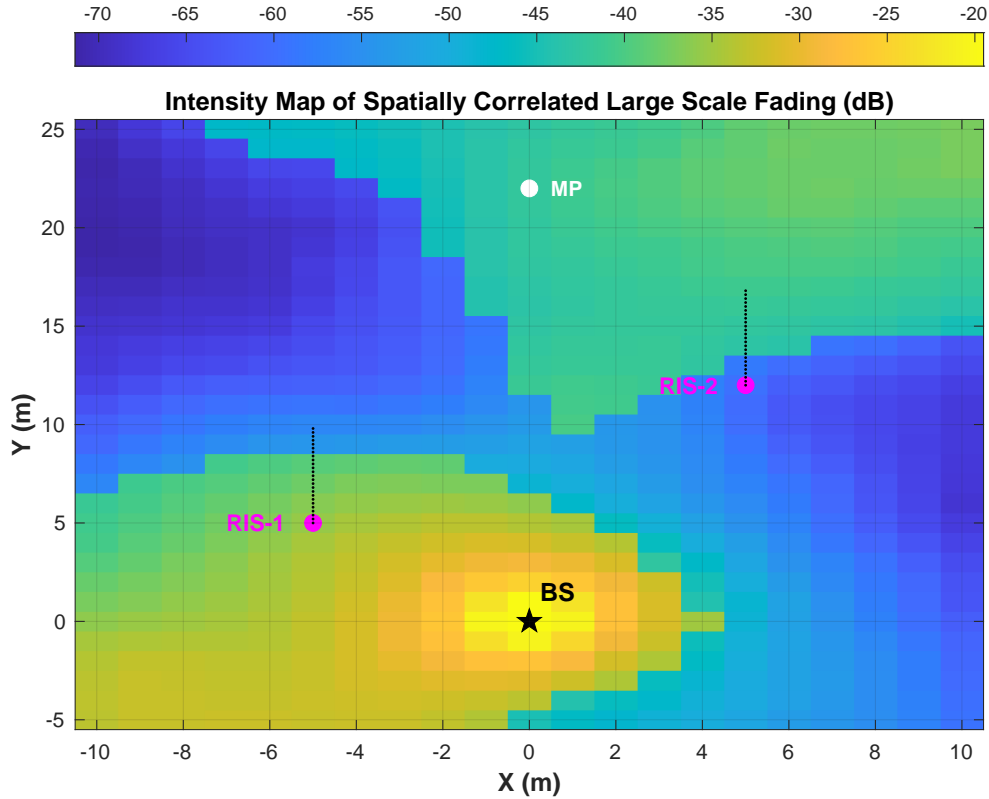


Figure 5.4: Demonstration for the power distribution regarding shadowing and path-loss effects. Initial RISs locations and their trajectories are shown as magenta circle, and black dashed line, respectively.

the scenario in Figure 5.1 depicts, more than one repositionable dynamic RISs with a simple rail-based moving system will be implemented to examine the superiority of repositionable dynamic RISs, in terms of spectrum utilization and interference management.

The position of RIS may be initially changed along the linear line in the range of approximately five meters with a slow speed (in the scale of seconds). Since its position will change along the one dimension and the geometry of RIS elements will be fixed, tracking and channel estimation process (or equivalent synchronization) will be practical to implement and deployment compared to 3D movement in spatially adaptive antenna arrays.

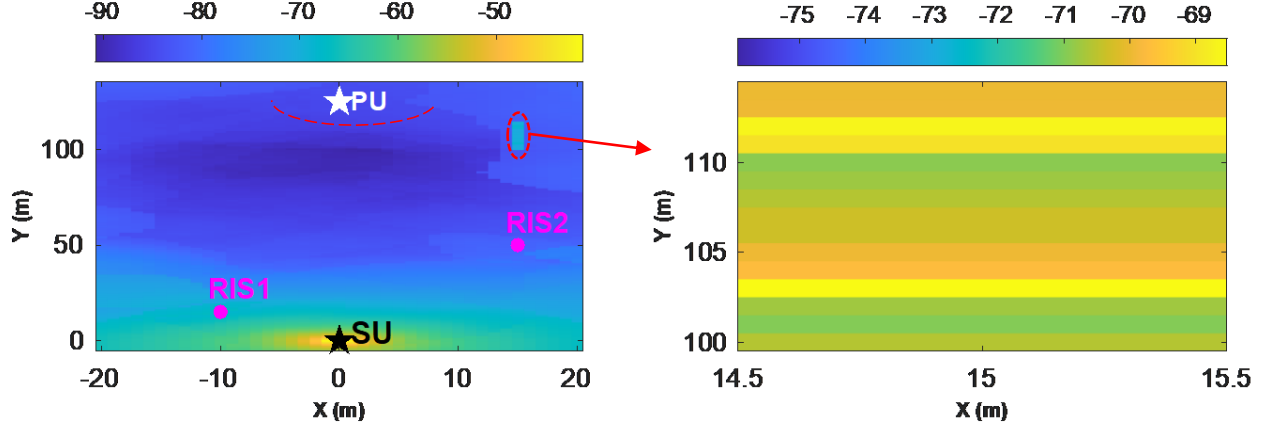


Figure 5.5: Demonstration of coverage extension with two RISs compared where the color map is scaled in dB.

5.3.2 Methodology

To realize the spatial consistency while re-positioning the RIS, spatially correlated large-scale parameters such as SF (shadow fading), line-of-sight (LOS)/non-LOS (NLOS) condition are generated [133]. The correlation distance in indoor simulation is determined as 5 meter [147]. In addition to point-to-point channel \mathbf{H} generated in (5.3a) and (5.3b), a 2D exponential filter is applied to the simulated area as follows:

$$f(p, q) = \exp\left(-\frac{\sqrt{p^2 + q^2}}{d_{co}}\right), \quad (5.10)$$

where p and q are filter coordinates with respect to the center of the filter, d_{co} is the correlation distance of shadowing. Applying the filter to the channel \mathbf{H} , the correlated values in the map is calculated as follows:

$$\mathbf{H}_c(i, j) = \sum_p \sum_q f(p, q) \mathbf{H}(i - p + 1, j - q + 1), \quad (5.11)$$

where $\mathbf{H}_c(i, j)$ is the correlated channel, i and j are the coordinates of grid points in the map \mathbf{M} with $(i, j)_k \in \mathbb{R}^2$ for k th RIS. Throughout the study, the movement of the RIS is constrained in only y axis with at most 5 m distance change as it is shown in Figure 5.4.

5.3.3 Problem Formulation to Control Channel Clusters

The aim to deploy repositionable dynamic RIS on the environment is to have a more control on the channel power variations in a short time frame. It introduces a new degree of freedom, where the speed and location of the RIS can be controlled. The problem is how to extend the coverage of secondary use in the dedicated area with the help of novel technique, repositionable dynamic RIS.

With the concept of repositionable dynamic RIS, the channel gain evaluated in (5.7) depends on the position of k th RIS. The location k th RIS of RISs is expressed as 2D pairs, $(i, j)_k, \forall k = 1, \dots, K$. The channel matrix $\mathbf{H}(i, j)$ at that position is obtained via (5.11). Then, the channel gain G'_m for the m th MP can be written as follows:

$$G'_m = \left| \mathbf{H}_{\text{BS-MP}_m} \mathbf{W} + \sum_{k=1}^K \mathbf{H}(i, j)_{\text{RIS}_k\text{-MP}_m} \mathbf{\Theta}_{\text{RIS}_k} \mathbf{H}(i, j)_{\text{BS-RIS}_k} \mathbf{W} \right|^2. \quad (5.12)$$

One realization of spatially correlated map with two RISs placed in the environment can be seen in Figure 5.4. Similar to (5.8), the capacity of the m th MP with different RISs locations is evaluated as follows:

$$R'_m = B \log_2 \left(1 + \frac{G'_m}{\sigma^2} \right). \quad (5.13)$$

The position $(i, j)_k$ of the k th RIS is needed to be considered in the optimization problem (5.9), when the repositionable dynamic RIS is studied. By defining the position matrix with $\mathbf{Z} = [(i, j)_1^T, \dots, (i, j)_K^T]$, and $\mathbf{R}' = [R'_1, R'_2, \dots, R'_M]$ the problem formulation (5.9) can be

Algorithm 5.2 Alternating Optimization for (5.14)

- 1: Initialize the all elements of \mathbf{W} , and $\theta_{n_{\text{RIS}_k}}, 1 \leq n_{\text{RIS}_k} \leq N_{\text{RIS}_k}, \forall k = 1, \dots, K$ with one. Also, choose arbitrary RISs locations to determine $(i, j)_{\text{RIS}_k}$.
 - 2: **repeat**
 - 3: **for** all grid points $(i, j)_{\text{RIS}_k} \in \mathbf{M}, \forall k = 1, \dots, K$ **do**
 - 4: **for** $n \leq N_{\text{BS}} + N_{\text{RIS}_1} + N_{\text{RIS}_2}$ **do**
 - 5: Find the indices $\varsigma_{\text{BS}} \in \mathcal{S}_{\text{BS}}, \varsigma_{\text{RIS}_k} \in \mathcal{S}_{\text{RIS}}$, and $(i', j')_{\text{RIS}_k} \in \mathbf{M}$ that maximize the average capacity of total M MPs, which defined as $\mathbb{E}\{\mathbf{R}'\}$
 - 6: Assign the corresponding phase shift values depending on the index ς_{BS} or ς_{RIS_k} to the corresponding antenna phase shifter n
 - 7: **end for**
 - 8: Fix the position of k th repositionable dynamic RIS to the point of $(i', j')_{\text{RIS}_k}$
 - 9: **end for**
 - 10: **until** Convergence is reached
-

modified as follows:

$$\begin{aligned} (P2) \quad & \max_{\Theta_{\text{RIS}}, \mathbf{W}, \mathbf{Z}} \mathbb{E}\{\mathbf{R}'\} \\ \text{s.t.} \quad & \|\mathbf{W}\|^2 \leq P \\ & \theta_{n_{\text{BS}_k}} \in \mathcal{F}_{\text{BS}}, \quad 1 \leq n_{\text{BS}_k} \leq N_{\text{BS}_k} \\ & \theta_{n_{\text{RIS}_k}} \in \mathcal{F}_{\text{RIS}}, \quad 1 \leq n_{\text{RIS}_k} \leq N_{\text{RIS}_k} \\ & (i, j)_k \in \mathbf{M}. \end{aligned} \tag{5.14}$$

Similar to Algorithm 5.1, exhaustive searching of both the position of RISs and their phase of elements is considered to solve non-convex optimization problem (5.14). Detailed algorithm scheme is presented Algorithm 5.2.

5.3.4 Numerical Results

The advantage of repositionable RIS in terms of capacity can be seen in Fig. 5.6, considering both 1-bit and 4-bits RIS. It is observed that approximately 15% improvement in the capacity of secondary system is achieved with the use of repositionable dynamic RIS. Also, the increase in the phase shifter capability helps to enhance the system performance, as well.

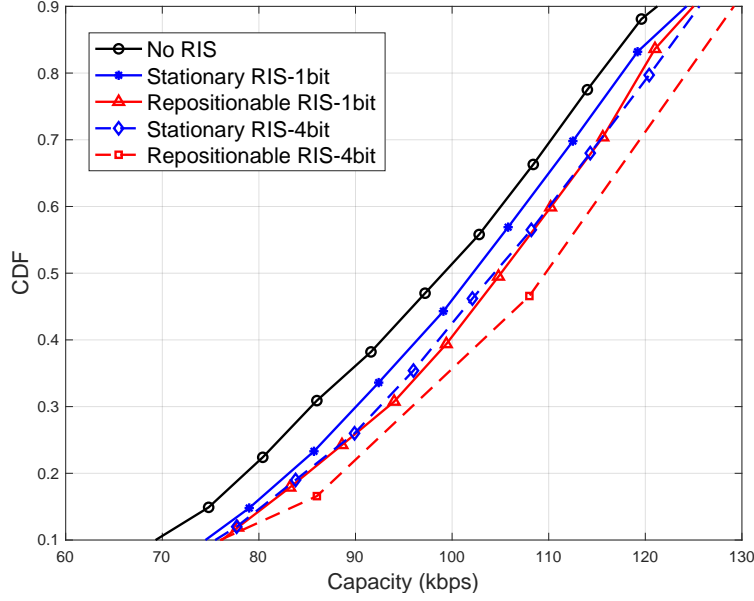


Figure 5.6: Numerical evaluation of capacity of the proposed system showing the advantage of repositionable dynamic RIS.

Throughout the study, it is assumed that the speed of RISs is low enough to neglect the Doppler shifts. However, the time domain representation including time-frequency Doppler shift profile of the received signal and its effect on performance should be studied and more general mobility patterns, including ways of linear and nonlinear motion, should be explored in the future research.

5.4 Creation of Radiation Rejection Zone via ABCs

5.4.1 State of the Art

Although the dynamic deployment of RISs can extend the radio coverage of the co-existing system(s), to avoid the interference to the primary system (particularly the receivers of primary system having high radio sensitivity or operating in low signal strength), there are needs for further improved technology beyond effective guided radio coverage by RISs. A disruptive thinking to this technology challenge is to create the *radiation rejection zone* as shown in Figure 5.2 against signal transmission from the secondary system. Such radiation rejection zone shall meet the following conditions: (i) further degrading the signal strength

from the secondary system into the zone; (ii) minimum interference to the reception of primary system; (iii) the radiation rejection being formed by devices of low energy consumption or battery-less.

To facilitate the disruptive technology forming the radiation rejection zone, considering coherent modulations in state-of-the-art systems, it may disruptively backscatter the signals from secondary system and deploy these nodes just outside the area of desirable radiation rejection zone. The rationale behind is to use each backscatter node to create a new transmission path with appropriate phase change in the nearby area (due to low power), such that creates man-made deep fades of secondary co-existing transmission for nearby receivers of primary use. This disruptive way to apply backscatter technique is simple but surprisingly satisfies desirable conditions.

The ABC is introduced by [148, 149] with little or even no battery power. With the advance of wireless power charging technology, ABCs has received great attention [150] in IoT and sensor networks. Its reservation-based multi-access is studied in [151]. Further explorations based on cooperative communications [152] and cognitive communications [153] suggest wide range of application scenarios. For low-complexity, non-coherent backscatter communication is examined in [154]. All rely on successful RF/antenna implementation. Recently, symbiotic radio (SR) system is proposed to utilize cognitive backscattering communication concept to enhance the reliability and inter-connectivity of ABC devices [155].

5.4.2 Methodology

The concept of creating man-made deep fades to reject radiation from secondary co-existing communication, of course, can not be realized simply by 180° phase inversion at each scattering node, which must be organized into a small antenna array to create meaningful man-made fades. A combination of two beamforming integrated circuit (BFIC) can be used for ABC implementation having two antenna arrays for transmit (Tx) and receive (Rx) functionality. The array can includes both variable 5-bit phase shifter and variable amplifier

Algorithm 5.3 Alternating Optimization for (5.17)

- 1: Initialize the all elements of \mathbf{W} and $\Theta_{ABC_l}, \forall l = 1, \dots, L$ with one.
 - 2: **repeat**
 - 3: **for** $n \leq N_{BS} + \sum_l^L N_{ABC}$ (total elements) **do**
 - 4: Assign the corresponding phase shift value depending on the index j to the antenna i
 - 5: Find the indices $\varsigma_{BS} \in \mathfrak{S}_{BS}$ and $\varsigma_{ABC_l} \in \mathfrak{S}_{ABC}$ that minimize the average channel gain of total M MPs, denoted as \mathbf{G}''
 - 6: Assign the corresponding phase shift values depending on the index ς_{BS} or ς_{ABC_l} to the corresponding antenna phase shifter n
 - 7: **end for**
 - 8: **until** Convergence is reached
-

with the range of 31 dB. Two micro-controller units can arrange both the phase, amplitude and functionality of the ABC antenna array. Actually, thanks to similarity in RIS and ABC, these backscatter nodes together can form the mutual symbiotic wireless system, by reusing earlier mathematical principles regarding the mmWave channel and 2D topographic map generation. Instead of using the RIS, multiple ABCs are placed near the protected zone to collectively form the desirable radiation rejection zone around the sensitive primary receiver as Figure 5.2. Particularly, the radiation rejection zone shown inside the red line in Figure 5.2 may well serve the protection to primary passive and active uses.

Similar to phase shifter matrix of the RIS, the analog beamforming matrix of l th ABC is defined as $\Theta_{ABC_l} = \text{diag} \left(\beta_1 e^{j\theta_1}, \dots, \beta_{n_{ABC_l}} e^{j\theta_{n_{ABC_l}}}, \dots, \beta_{N_{ABC_l}} e^{j\theta_{N_{ABC_l}}} \right)$, where $l = 1, \dots, L$ and L is the total number of ABCs operating in the system where each ABC has N_{ABC} antennas. To explore the advantage of deploying multiple ABCs to protect the radiation rejection zone from secondary transmissions, ABCs are first assumed to locate beside the protected zone. Addition to the common channel model explained in the subsection 5.2.2, for the m th MP, the matrices $\mathbf{H}_{BS-ABC_l} \in \mathbb{C}^{N_{ABC_l} \times N_{BS}}$, and $\mathbf{H}_{ABC_l-MP_m} \in \mathbb{C}^{1 \times N_{ABC_l}}$ are generated where N_{ABC_l} denotes the antenna number of the l th ABC. The phase matrix of l th ABC is $\Theta_{ABC_l} \in \mathbb{C}^{N_{ABC_l} \times N_{ABC_l}}$. Similar to transmitter antenna array, phase shifter of ABC generates $2^{b_{ABC}}$ options with the control of b_{ABC} bits. The phase shift selection for the n_{ABC} th transmit

antenna can be chosen from the set \mathcal{F}_A where

$$\mathcal{F}_A = \left\{ \theta_{n_{\text{ABC}_k}} = \frac{\varsigma_{n_{\text{ABC}}}\pi}{2^{b_{\text{ABC}}}-1} \mid \varsigma_{n_{\text{ABC}}} \in \mathfrak{S}_{\text{ABC}} = \{0, \dots, 2^{b_{\text{ABC}}}-1\} \right\}. \quad (5.15)$$

The channel gain from the secondary user transmission for the m th MP, G''_m , can be written as follows:

$$G''_m = \left| \mathbf{H}_{\text{BS-MP}_m} \mathbf{W} + \sum_{l=1}^L \mathbf{H}_{\text{ABC}_l\text{-MP}_m} \mathbf{\Theta}_{\text{ABC}_l} \mathbf{H}_{\text{BS-ABC}_l} \mathbf{W} \right|^2, \quad (5.16)$$

where the total L number ABCs located in the vicinity of primary user. The interference power in m th MP around the primary user region due to secondary user transmission is equal to G''_m .

5.4.3 Problem Formulation for Nulling the Zones

Here, the aim for using multiple coordinated ABCs is to reject the radiation due to secondary transmission in the vicinity of primary use. The electromagnetic energy is shaped via backscattering phenomena to protect the primary use zone from unwanted and detrimental radiation. It is shown in the numerical results that by coordinating every ABC nodes, the zone which is protected from primary user radiation can be created.

Letting $\mathbf{G}'' = [G''_1, \dots, G''_M]$ and $\mathbf{\Theta}_{\text{ABC}} = [\mathbf{\Theta}_{\text{ABC}_1}, \dots, \mathbf{\Theta}_{\text{ABC}_L}]$, the optimization problem aiming to create radiation rejection zone can be formulated as minimization problem [156]:

$$\begin{aligned} (P3) \quad & \min_{\mathbf{\Theta}_{\text{ABC}}, \mathbf{W}} \mathbb{E}\{\mathbf{G}''\} \\ & \text{s.t.} \quad \|\mathbf{W}\|^2 \leq P \\ & \theta_{n_{\text{BS}_k}} \in \mathcal{F}_{\text{BS}}, \quad 1 \leq n_{\text{BS}_k} \leq N_{\text{BS}_k} \\ & \|\mathbf{\Theta}_{\text{ABC}_l}\|^2 \leq P_l, \quad 1 \leq l \leq L, \\ & \theta_{n_{\text{ABC}_k}} \in \mathcal{F}_A, \quad 1 \leq n_{\text{ABC}_k} \leq N_{\text{ABC}_k} \end{aligned} \quad (5.17)$$

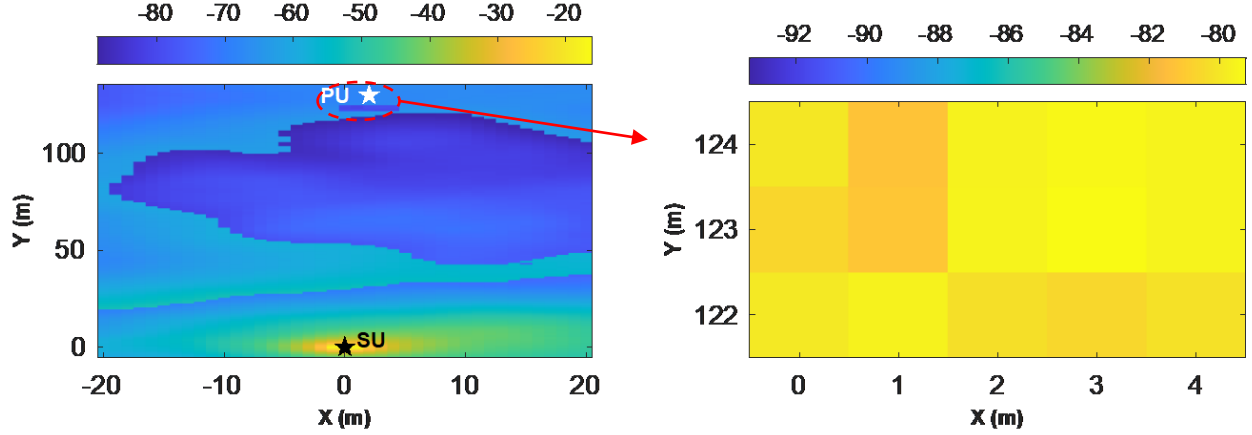


Figure 5.7: Demonstration of zone protection only with BS beamforming antennas are optimized where the color map is scaled in dB.

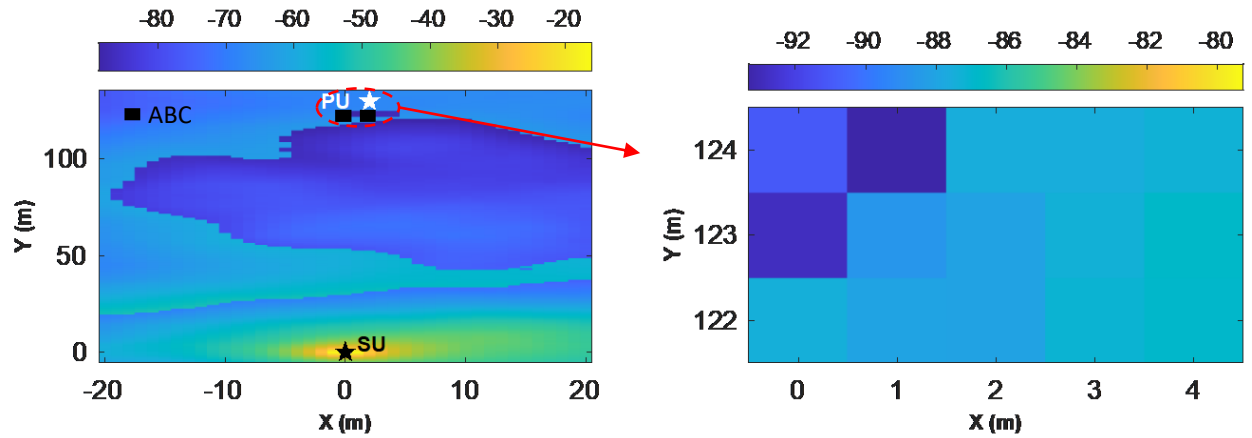


Figure 5.8: Demonstration of zone protection of proposed system architecture with multiple ABCs where the color map is scaled in dB.

where P_l is the power constraint of the l th ABC. Similar to Algorithm 5.1 and Algorithm 5.2, alternating optimization technique is again utilized to arrange the phase shifts at the BS, and ABCs of 5-bit discrete phase-shifters. The aim of the optimization algorithm for the problem (5.17) is instead to minimize the average interference power in the area of secondary use, $\mathbb{E}\{\mathbf{G}''\}$.

5.4.4 Numerical Results

The 2D topological color map in Figure 5.7 and 5.8 show the performance of multiple coordinated ABCs minimizing the signal power in encircled area in terms of dB. The SU is

denoted as black star, where the PU is a white star. Multiple ABCs are denoted as black circles which are distributed around the protected zone. The detected radiation power in the encircled area by BS beamforming is shown in Figure 5.7, whereas the effect of multiple ABCs to suppress the interference is clearly observed (in colder color) in Figure 5.8. In the enlarged plots, initial usage of ABC achieves 12 dB reduction of the interference power in the rejection zone protecting primary system or its sensitive receiver. Although ambient backscatter nodes are just intuitively placed in the study, impressive degradation to form the radiation rejection zone is proven a disruptive but effective approach. Based on the rich literature about ABC, further explorations and exploitation can be conducted.

5.5 Radiation Control with Repositionable Dynamic RIS and ABCs

In the existing literature, the RIS technology has been integrated into ambient backscatter communication system for performance improvement [157, 158, 159, 135]. In [157], the effect of the RIS on the source-to-reader and source-to-tag links of the ABC system is investigated with the BER performance indicator. Moreover, reference [158] studies advanced spatial multiplexing techniques of the RIS assisted ABC system by analytically showing that presence of the RIS can improve the spectral and energy efficiency. Experimental analysis of the RIS improved ABC system is performed in [159]. It is shown that pre-defined codebooks of the RIS can be selected according to the location of the ABC tag where its BER performance can be enhanced. The RIS-assisted MIMO symbiotic radio system is proposed in [135] where the RIS both enhance the primary transmission and embed the message acting like secondary transmission. In our work, the use multiple ABCs and the repositionable dynamic RIS in a coordinated manner is novelly proposed to control the electromagnetic radiation in 3D cognitive radio system.

In this section, the proposed ideas in Section 5.3 and Section 5.4 are integrated into one system in order to control the whole electromagnetic radiation that is emitted from secondary BS. It is aimed that the radiation power in the vicinity of primary use is minimized which is

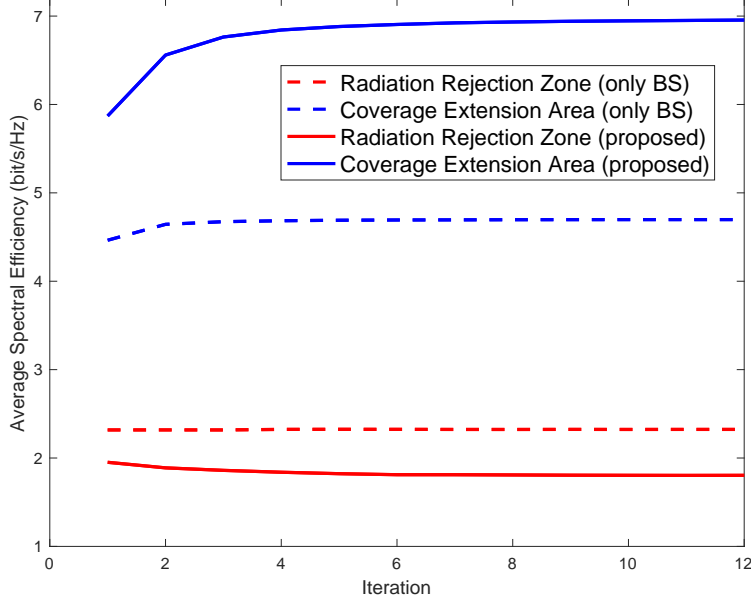


Figure 5.9: Convergence performance of the proposed method and its comparison with the case where RISs and ABCs are absent.

called as radiation rejection zone, and at the same time, the whole radiation from secondary BS is steered to area where power of secondary use needs to be maximized.

Putting together both dynamic repositionable RISs and multiple ABCs into one systems to control the whole electromagnetic radiation in the environment, the problem formulation (5.14) and (5.17) can be revisited as follows:

$$\begin{aligned}
 & \max_{\Theta_{\text{RIS}}, \Theta_{\text{ABC}}, \mathbf{W}, \mathbf{Z}} \mathbb{E}\{\mathbf{R}'\} & (P4) \\
 & \text{s.t.} & \\
 & & \|\mathbf{G}''\|^2 \leq I \\
 & & \|\mathbf{W}\|^2 \leq P \\
 & & \theta_{n_{\text{BS}_k}} \in \mathcal{F}_{\text{BS}}, \quad 1 \leq n_{\text{BS}_k} \leq N_{\text{BS}_k} \\
 & & \theta_{n_{\text{RIS}_k}} \in \mathcal{F}_{\text{RIS}}, \quad 1 \leq n_{\text{RIS}_k} \leq N_{\text{RIS}_k} \\
 & & (i, j)_k \in \mathbf{M} \\
 & & \|\Theta_{\text{ABC}_l}\|^2 \leq P_l, \quad 1 \leq l \leq L. \\
 & & \theta_{n_{\text{ABC}_k}} \in \mathcal{F}_A, \quad 1 \leq n_{\text{ABC}_k} \leq N_{\text{ABC}_k}
 \end{aligned} \tag{5.18}$$

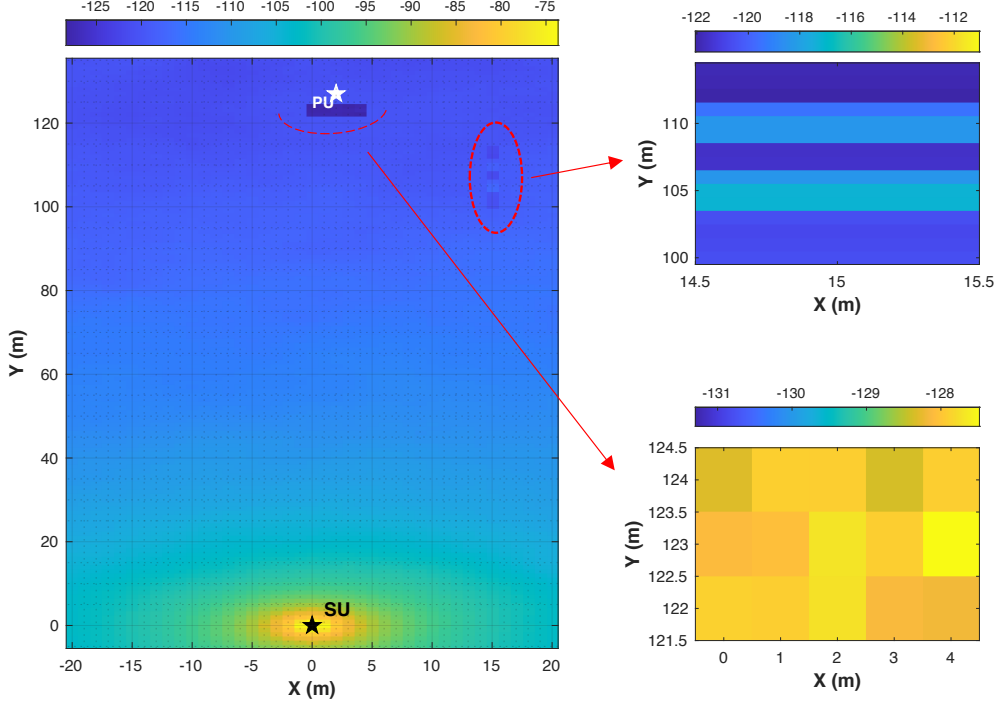


Figure 5.10: Demonstration of radiation control with only BS beamforming where the color map is scaled in dB.

where I is the predefined interference power constraint in the vicinity of primary use.

Problem (5.18) has both non-convex objective function and constraints under the sets $\mathcal{F}_{\text{BS}}, \mathcal{F}_{\text{RIS}}, \mathcal{F}_{\text{A}}$ similar to [160]. Monte Carlo method is used to eliminate the mathematical expectation in the objective function of (5.18). Then alternating optimization method similar to Algorithm 5.2 and Algorithm 5.3 is employed to find sub-optimum solutions for $\Theta_{\text{RIS}}, \mathbf{W}, \mathbf{Z}$.

It can be readily verified that the objective value of (5.9) and (5.14) monotonically increases with alternating optimization algorithm in each iteration where coverage has desired to be increased. In addition, due to the power constraints, the objective function has an upper bound. It is guaranteed to converge. Besides, the proposed algorithm can guarantee to yield a monotonically decreasing objective function value compared to the previous phase solution, i.e., $\mathbf{G}''(\Theta_{\text{ABC}})^{t+1} < \mathbf{G}''(\Theta_{\text{ABC}})^t$ for interference minimization in (5.17) where t denotes the iteration number. The convergence performance of the proposed alternating op-

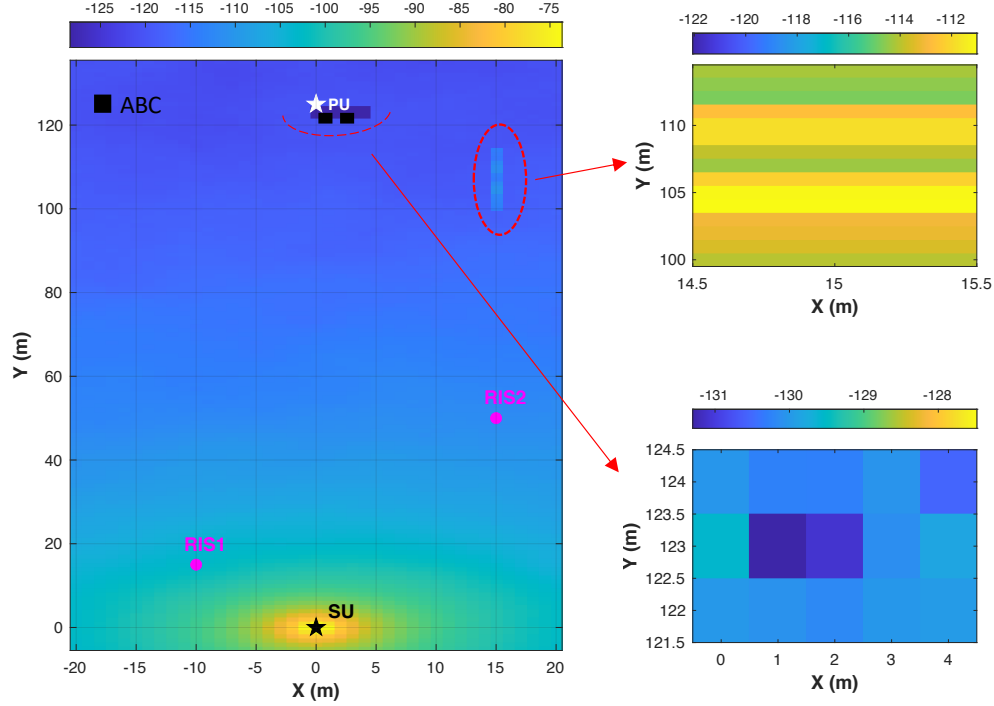


Figure 5.11: Demonstration of radiation control with repositionable dynamic RISs and multiple ABCs where the color map is scaled in dB.

timization algorithm is presented in Figure 5.9. Here, vertical axis demonstrates the average spectral efficiency overall MPs in the coverage extension area and radiation rejection zone due to secondary BS emission. It can be seen from Figure 5.9 that the proposed algorithm converges for about 6 iterations. It can also be implied that the proposed structure enhances the spectral efficiency of coverage extension area of secondary use. At the same time, it can be implied that the proposed structure decreases the electromagnetic radiation of secondary use on the vicinity of primary use.

The coexistence of the repositionable dynamic RISs and multiple ABCs are studied in Figure 5.10 and 5.11. The simulation parameters for BS, RIS and ABC are given in Table 5.1, as well. The dB scale color map shown in Figure 5.10 is obtained by optimizing the antennas of secondary BS. On the other hand, the position repositionable dynamic RIS and phase shifts of ABCs and RISs antennas are optimized in the Figure 5.11. It can be seen that the signal power of secondary BS is enhanced around 10 dB in the coverage extension area. At the

same time, the interference power in the vicinity of primary use can be rejected around 3 dB. The computational complexity of the proposed algorithms includes the multiplication of all possible selections for Θ_{RIS} , Θ_{ABC} , \mathbf{W} , \mathbf{Z} depending on b_{RIS} , b_{ABC} , b_{BS} and the coordinates of grid points in the map \mathbf{M} , which is relatively high and needs to be decreased to make proposed structure suitable for real test-bed.

5.6 Machine Learning to Form Spectrum Map

One critical criterion to form a smart radio environment is to classify the permissible area(s) allowing co-existing radio communication. In this section, we propose to elaborate machine learning technique to better accomplish the goal.

5.6.1 State of Art

One of the fundamental challenge of next wireless communications systems lies in the spectrum utilization with the increase in massive connectivity and various quality of service (QoS) requirements [161]. The spectrum availability (or utilization *vice versa*) indicated on the geographical map is known as *spectrum map*, which was initially realized by synthetic aperture radar [162] or compressive sensing [163]. Its application to cellular systems starts from cognitive radio resource allocation based on distributed sensing [164] in 3GPP R10. Cognitive radio network tomography further utilizes statistical inference to enable holistic understanding of spectrum activities [165]. Integrating both cognitive radio network tomography and spectrum map [166], the spectrum map can empower resource management for QoS guarantees [167] and opportunistic routing [168]. The amazing aspect of spectrum map is explained by Figure 5.1 to allow secondary systems geographically separated from primary systems, and thus achieve near ideal co-existing communication toward more efficient utilization of spectrum. ML has been introduced to cooperative [169], non-cooperative [170], mobile [171], and spatio-temporal [172] spectrum sensing mechanisms. With the enhanced ML techniques, the intelligent spectrum sensing will play an essential role in co-existing radio

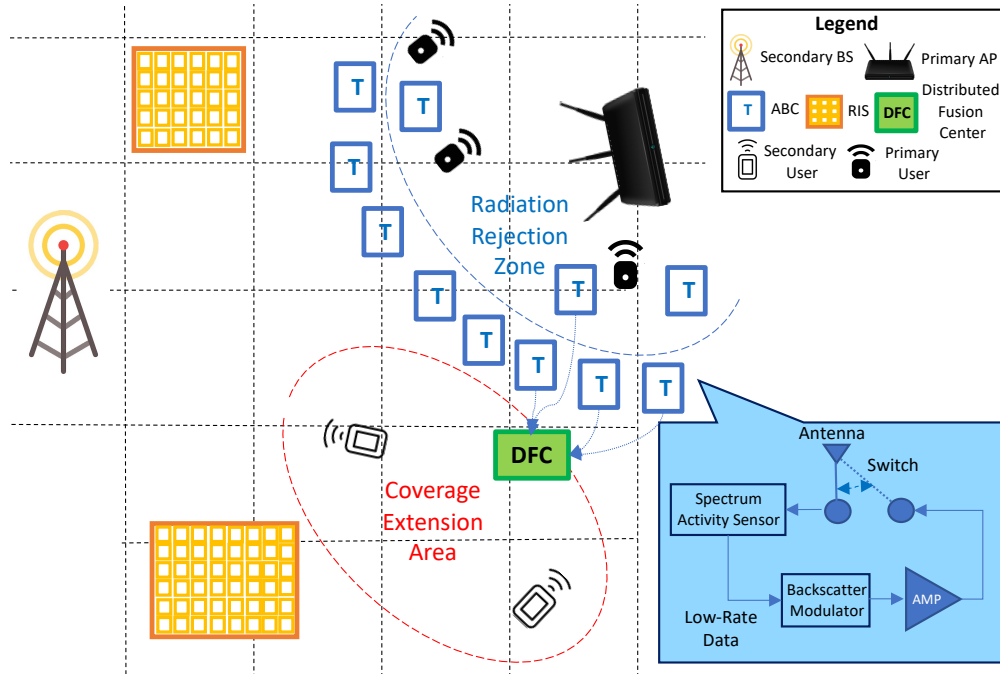


Figure 5.12: Spectrum activity sensor generates low-rate data that is transmitted via backscatter communication to DFC so that edge AI can forecasts spectrum activities to dynamically adjust RISs.

networks [173]. A recent effort applies SVM to classify historical spectrum decision data to create the two-dimensional transmission opportunity map for a transmitter [174]. Both [175] and [176] take advantage of a number of distributed devices to facilitate intelligent wireless communication, which inspires ML to construct spectrum map.

5.6.2 Spectrum Sensors Applying Backscatter Communications

Cooperative spectrum sensing has been proposed for a long time, which suffers the extra communication from sensors to the transmitter. The intuitive construction of spectrum map inevitably requires cooperative spectrum activity sensors but keeps the spatial spectrum efficiency as same. Synthetic aperture radar leveraging antenna array to construct spectrum map [162] can see through its coverage but not enough to establish the spectrum map for the entire region. Recalling the fact that each spectrum sensor only needs to transmit 1-bit information to construct the entire spectrum map [163], we again take advantage of ABC to form

a smart spectrum sensor network toward the entire spectrum map as shown in Figure 5.12. As the blue box, a spectrum sensor senses the radio strength at certain frequency band(s) and translates into a short data packet, which the spectrum information is decoded into 1 (or just few) bit to well serve the purpose of spectrum map construction for any frequency band. Such small data packet can leverage ABC (with optional amplification depending on the operating needs) to be transmitted to a DFC when the RF switch turns to the transmission mode. By this way, the spectrum sensors can operate in a maintenance-free manner since such ABCs may utilize energy harvesting, which resolves the *device management* dilemma of sensor networks.

We may view the transmitter in Figure 5.12 as the BS or AP in the RAN of the secondary system, which has an edge server to analyze the sensor data to (i) construct the spectrum map (ii) control the RISs accordingly and possibly move RIS dynamically. There are likely several DFC in the intended radio coverage region and DFC has battery-operating communication and computational capability. These DFCs can (i) send data to BS to learn in a centralized manner, or (ii) exchange in an distributed ad hoc manner among them and BS, with privacy-preserving functionality.

5.6.3 Support Vector Machine to Classify Spectrum Map

Fundamentally, the construction of spectrum map based on the spectrum activity sensor data may proceed: hypothesis testing or statistical classification, and two-dimensional estimation or regression. Due to potential complex geometric property, statistical classification is considered. Different ML techniques toward cooperative spectrum sensing are investigated in wireless IoT, HetNets, MIMO, D2D and NOMA networks [177, 178]. Generally, cooperative spectrum sensing is to determine the transmission opportunity at a single geographical location for point-to-point cognitive radio communication. On the contrary, spectrum map to realize proposed multiple RISs technology provides the information to transmit the radio signals through a wide geographical area to serve multiple secondary co-existing users, much

beyond a single point. After examining ML techniques [179, 180] and considering the fact that there lacks of stationary data to construct spectrum map that is designed for the need of dynamic radio channels including interference, SVM derived from statistical learning appears to meet our initial purpose with partially known models of communication systems. Also, SVM can even handle 1-bit sensor information to get satisfactory results, which is cumbersome for other ML techniques. Applying SVM to construct 2D or even 3D spectrum map has a fundamental difference from spectrum sensing for point-to-point communication, while adopting linearly separable SVM [181]. Even though spectrum sharing concept is studied for ABC networks in [182], how to obtain spectrum map and how to perform spectrum sensing via ABCs are not clear. Inspired by [183] where linear and nonlinear kernel SVM analysis for coverage boundary detection are performed, this study explores ML aided spectrum map construction based on limited sensor information obtained via backscatter communication which is shown as efficient and thus helps to establish smart radio environment.

Mathematically, the spectrum activity data from n th sensor forms the sensor data vector \mathbf{x}_n . Based on the sensing spectrum value (e.g., radio signal strength, etc. at the target frequency band), the n th sensor can be classified as label y_n indicating suitability for secondary communication ($y_n = +1$) or unsuitability ($y_n = -1$) at its location. For each geographical location of interest, the BS of the secondary system must *predict* its label (i.e. $+1$ or -1). In a geographical area of the secondary co-existing system, a hyperplane $\mathbf{a}^T \mathbf{x} + b = 0$ to separate into a region ($+1$) and another region (-1). The goal of learning is to find \mathbf{a}, b . For a 2-D area, this hyperplane is actually a line in a *linearly separable* SVM classification problem. Unfortunately, such a solution is obviously useless for spectrum map. To resolve this dilemma, the SVM classification of spectrum map can be modified into the Lagrange multiplier version as

$$\mathcal{L} = \sum_{n=1}^N \lambda_n - \frac{1}{2} \sum_{i=1}^N \sum_{j=1}^N \lambda_i \lambda_j y_i y_j \mathbf{x}_i^T \mathbf{x}_j. \quad (5.19)$$

The equivalent problem is to maximize \mathcal{L} over $\lambda_n \geq 0$, subject to $\sum_{n=1}^N \lambda_n y_n = 0$, which is known as the *dual problem*. Once we found the $\lambda_n, n = 1, \dots, N$, the dual version of this classifier for a new data point \mathbf{x}_{new} can be expressed as follows to classify H_1 and H_0 (i.e. permissible for co-existing secondary system to operate or not):

$$\sum_{n=1}^N \lambda_n y_n \mathbf{x}_n^T \mathbf{x}_{new} + b \begin{matrix} > \\ < \end{matrix} 0. \quad (5.20)$$

The maximization of \mathcal{L} will return almost all λ_n as zero. Those who are not zero correspond to the *support vectors* that define the margins. Furthermore, the problem can be extended into the soft-margin problem as follows:

$$\mathcal{J} = \frac{1}{N} \sum_{n=1}^N \max [1 - y_n(\mathbf{a}^T \mathbf{x}_n + b), 0] + \lambda \|\mathbf{a}\|^2, \quad (5.21)$$

where \mathcal{J} consists of two terms which are loss function and regularization. λ plays the role of weighting between margin size and whether it lies on the correct side of the margin or not. Since \mathcal{J} is convex in \mathbf{a} , the (stochastic) gradient decent method is suitable for finding the solution. As shown in Figure 5.1, simple curve is still not enough for the desired co-existing utilization of spatial spectrum under complex propagation environments. Consequently, the radial basis function kernel, $K(\mathbf{x}, \mathbf{x}') = \exp(-\frac{\|\mathbf{x}-\mathbf{x}'\|^2}{2\sigma^2})$, also known as Gaussian kernel, is introduced. Furthermore, transmission from all sensors all the time consumes a lot of bandwidth. Therefore, each spectrum sensor shall decode the spectrum information into 1 bit (suitable for co-existing communication or not) according to compressed sensing [163].

5.6.4 Numerical Results

There exists an advantage by 1-bit spectrum information: the spectrum sensors around the area requiring high radiation rejection, such as that for radio astronomy, measure low spectrum activity and the raw data can mislead the construction of spectrum availability

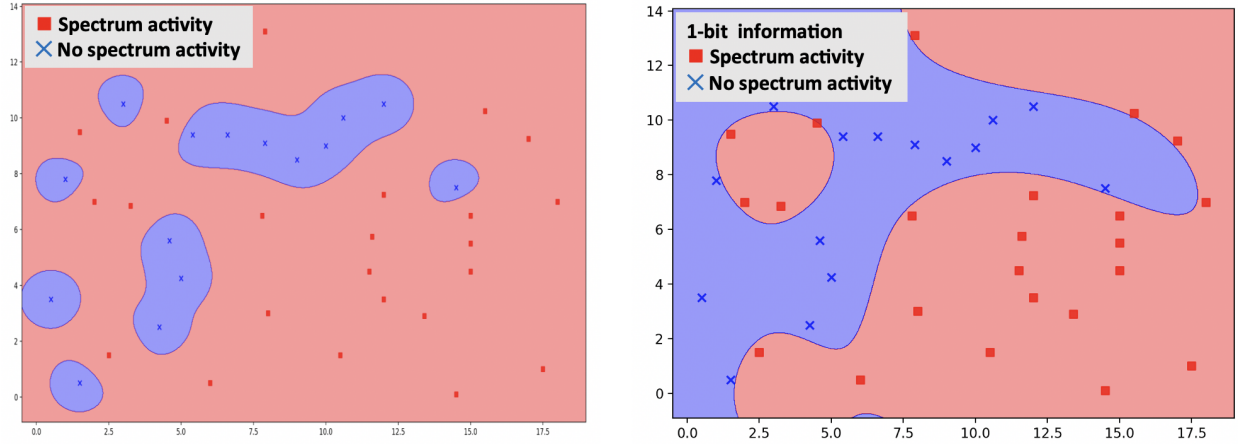


Figure 5.13: Reconstruction of spectrum. (Left) Reconstruction of spectrum based on 1-bit information of spectrum activity and conventional SVM using radical basis kernel, while red region indicates active operation of primary system. (Right) Successful construction of spectrum map to identify permission region (in blue) and active zone of primary system and the area requiring high radio rejection based on the refinement of SVM.

map. A straightforward solution is to preset their values indicating unsuitable for co-existing communication, then using Gaussian kernel in (5.19).

As Figure 5.13 (Left) showing the consequent construction of spectrum map, it successfully forms the spectrum map indicating permissible region (suitable for secondary co-existing communication, in blue); but is not possible for effective utilization while the original spatial spectrum allows a large connected region for RIS technology. It is not because the Gaussian kernel only considers squared Euclidean distance. Actually, Gaussian kernel equivalently considers higher order terms in inner product space to accommodate complex propagation channel dynamics. To resolve this challenge, further techniques are required. As SVM performance is sensitive to parameters, slack variables ζ_n are introduced for $\mathbf{x}_n, \mathbf{y}_n$, the soft penalization $c_0 \sum_{n=1}^N \zeta_n + \frac{1}{2} \lambda \|\mathbf{a}\|^2$. Appropriate adjustment of parameters demonstrates accurate construction of spectrum map as shown in Figure 5.13 (Right).

5.7 Future Research Direction and Challenges

Despite the many researches since the beginning of RIS and ABC studies, there are still promising open research problems, which need to be considered thoroughly. In the following part, some research directions and challenges related to our study are presented.

5.7.1 Application Centric Coexisting Smart Radio

It is foreseen that 6G wireless systems will host much more diverse applications compared to 5G networks including holography, AR/VR assisted meta-verse, joint radar-sensing and communication, non-terrestrial networks, ultra-high speed railway networks. These networks will be in the same environment which are constantly interfering with each other. Repositionable dynamic RIS and multiple coordinated ABC assisted smart radio environment will be the remedy for highly overloaded future network in order to operate them in the minimal interference conditions since our scheme provides 3D electromagnetic radiation control over the environment. As future works, specific networks needs to be studied regarding their waveforms, scheduling and used frequency bands to make the proposed smart radio environment concept suitable for standalone structures.

5.7.2 Real Time Test-bed

Real time test-bed with repositionable dynamic RIS and multiple ABCs in different propagating environments needs to be studied rigorously. The test-bed should be designed to answer following critical questions: How can RISs and ABCs get the real-time channel estimation information to adjust their reflective elements? How will commands for the control of RISs and ABCs be declared in the real time? The development of EM-based repositionable dynamic RIS and ABC models and exploration of hardware imperfections/effects should be studied to make the proposed system feasible for next generation wireless communication systems.

5.7.3 Realistic and Sophisticated RIS and ABC

Robust optimization of resource allocation schemes is required in spatial, temporal and spectral domains. It includes the optimal position of multiple repositionable dynamic RISs and cross-coordinated optimization of the overall network including ABCs. The phase and amplitude arrangement of ABCs regarding the channel conditions of protected area and secondary user needs computationally efficient optimization. RIS-empowered PHY slicing which can support different applications such as wireless charging, PHY security and data transfer having passive, active and transmissive sub-surfaces are introduced in [184]. Such a concept can be generalized by leveraging our ML-based spectrum mapping and multiple coordinated ABCs frameworks to make coexisting smart radio environment more sophisticated and mission critical.

5.7.4 Performance Limits of RIS and ABC Assisted Networks

Placement of these ambient backscatter nodes to fade the radiation from secondary coexisting systems can be a critical extension in case knowing the location of BS and RISs. Further robust placement without precise knowledge of BS and RIS, simply based on the required radiation (spatial-spectrum) rejection from the secondary system, serves the ultimate goal. Calculation and proof of essential performance limits of RIS and ABC assisted networks are needed.

5.7.5 Federated Learning to Manage Spectrum Map

Once DFC obtain data from spectrum sensors, the learning to classify can be facilitated in two possible architecture, (i) hierarchical architecture such that DFC send the data to the BS for centralized learning then constructing spectrum map; (ii) ad hoc architecture such that DFC and BS exchange data in an ad hoc manner for distributed learning and constructing spectrum map. One of the purposes for distributed architecture is to avoid longer distance transmission consuming a lot of spatial spectrum. For the purpose of spatial bandwidth

efficiency and privacy-preserving for data, a disruptive application of federated learning (FL) [185] is proposed for spectrum map construction. Instead of transmitting the data, stochastic gradient descent (SGD) parameters of SVM can be relayed either hierarchically or in ad hoc manner. This falls into the vertical FL [185]. Only exchange learning parameters rather than data of spectrum sensing data further minimizes spectrum use for co-existing systems while achieving privacy-preserving and cybersecurity against data interception. Pros and cons by FL, compared with traditional sensor data transmission, needs to be exploited using single- or multi-channel parallel transmission for further studies.

5.7.6 Total Energy Consumption and Cost of RIS and ABC

With the increasing number of ABC nodes, the collaborative mechanism among ABCs and repositionable dynamic RISs should be investigated to enhance collective performance, given the energy and implementation constraints of ABC nodes. The amount of additional energy consumption should be investigated due to the positioning of RISs to find the optimum location.

Chapter 6: Conclusion

Throughout the Ph.D. studies, multiple accessing, cognitive radio, waveform, multiple-antenna, radar-sensing concepts are investigated. In Chapter 2, the need for next-generation multiple accessing is explained. Conventional orthogonal multiple accessing and NOMA is introduced with their drawbacks. The novel waveform-domain NOMA concept is presented and compared with the conventional power-domain NOMA scheme. The numerical results demonstrate that the proposed waveform-domain NOMA scheme is capable of overcoming the problems of power-domain NOMA in power-balanced scenarios. Moreover, waveform-domain NOMA gives flexibility to the users regarding their demands such as reliability, energy efficiency, spectral efficiency, and latency. A promising future research direction is to investigate the optimal waveforms that can be paired in waveform-domain NOMA. Also, the optimal coding schemes that are convenient for the chosen waveforms may be studied. The promising results of the waveform-domain NOMA concept may potentially spur the interest of the wireless industry, and academia; and pave the way for being possible multiple access scheme of 6G and beyond.

In Chapter 3, the implementation and validation of RSMA in OFDM waveform under different channel conditions is investigated. Proposed OFDM-RSMA structure is compared with conventional OFDMA and OFDM-NOMA in SISO-BC model. In OFDM-RSMA, common stream decoded by every user are transmitted on top of private streams decoded by the intended user only. The effect of delay spread and Doppler spread are studied. weighted minimum mean-square error (MMSE) (WMMSE) based algorithms are developed to solve corresponding optimization problems for OFDM-RSMA and OFDM-NOMA techniques.

Chapter 4 aims to explain the concept of dual-functional radar and communication systems and the novel studies based on the waveform structure to provide dual functionality. Joint radar-sensing and communication based on waveform domain NOMA is expressed indicating variation of waveforms regarding applications of wireless networks can be extended. Since the coexistence of different waveforms serves the need of flexibility considering applications and use cases that future wireless systems offers, it is likely that researchers pay attention to improve practicability of the proposed NOMA concept in DFRC systems.

The study in Chapter 5 novelly introduces a smart radio environment that shapes the electromagnetic energy in the spatial domain using channel control mechanisms such as repositionable dynamic RISs and multiple coordinated ABCs which is analogous to pulse shaping in time and frequency domain. Having coordinated network with repositionable dynamic RIS and multiple ABCs allow us to shape the electromagnetic wave in spatial domain by creating radiation rejection and coverage extension zones. A centralized or distributed mechanism to construct the spectrum map based on ABC sensor is also introduced to instruct existing repositionable dynamic RISs for better coverage. Merging these promising technologies will pave the way for the smart radio environment creating high spectral efficient wireless systems.

References

- [1] T. Eichler and R. Ziegler, “Fundamentals of THz technology for 6G by Rohde & Schwarz: White paper.” [Online]. Available: <https://www.rohde-schwarz.com/us/solutions/test-and-measurement/wireless-communication/cellular-standards/6g/white-paper-fundamentals-of-thz-technology-for-6g-by-rohde-schwarz>
- [2] Samsung, “6G the next hyper-connected experience for all,” 2021. [Online]. Available: <https://news.samsung.com/global>
- [3] A. Bourdoux, A. N. Barreto, B. van Liempd, C. de Lima, D. Dardari, D. Belot, E.-S. Lohan, G. Seco-Granados, H. Sardeddeen, H. Wymeersch, J. Suutala, J. Saloranta, M. Guillaud, M. Isomursu, M. Valkama, M. R. K. Aziz, R. Berkvens, T. Sanguanpuak, T. Svensson, and Y. Miao, “6G White Paper on Localization and Sensing,” *arXiv preprint arXiv:2006.01779*, 2020.
- [4] L. Zheng *et al.*, “Radar and communication coexistence: An overview: A review of recent methods,” *IEEE Signal Process. Mag.*, vol. 36, no. 5, pp. 85–99, Sept. 2019.
- [5] M. M. Sahin and H. Arslan, “Multiple accessing, multi-numerology, hybrid waveforms,” in *Wireless Communication Signals: A laboratory-based approach*. Wiley, 2021, p. 147–200.
- [6] M. M. Şahin and H. Arslan, “Waveform-Domain NOMA: The Future of Multiple Access,” in *2020 IEEE International Conference on Communications Workshops (ICC Workshops)*, 2020, pp. 1–6.

- [7] M. M. Şahin and H. Arslan, “Application-based coexistence of different waveforms on non-orthogonal multiple access,” *IEEE Open J. Commun. Soc.*, vol. 2, pp. 67–79, 2021.
- [8] Y. Liu, S. Zhang, Z. Ding, R. Schober, N. Al-Dhahir, E. Hossain, and X. Shen, “Guest editorial special issue on next generation multiple access—part ii,” *IEEE J. Sel. Areas Commun.*, vol. 40, no. 5, pp. 1387–1391, 2022.
- [9] Y. Liu, S. Zhang, X. Mu, Z. Ding, R. Schober, N. Al-Dhahir, E. Hossain, and X. Shen, “Evolution of NOMA toward next generation multiple access (NGMA) for 6G,” *IEEE J. Sel. Areas Commun.*, vol. 40, no. 4, pp. 1037–1071, 2022.
- [10] G. E. Bottomley, *Channel equalization for wireless communications: From concepts to detailed mathematics*. IEEE Press, 2011.
- [11] A. B. Kihero, M. S. J. Solaija, and H. Arslan, “Inter-numerology interference for beyond 5G,” *IEEE Access*, vol. 7, pp. 146 512–146 523, 2019.
- [12] H. Arslan, “OFDM signal analysis and performance evaluation,” in *Wireless Communication Signals: A laboratory-based approach*. Wiley, 2021, p. 147–200.
- [13] M. Rebhi, K. Hassan, K. Raouf, and P. Chargé, “Sparse code multiple access: Potentials and challenges,” *IEEE Open J. Commun. Soc.*, vol. 2, pp. 1205–1238, 2021.
- [14] T. Cover, “Broadcast channels,” *IEEE Trans. Inf. Theory*, vol. 18, no. 1, pp. 2–14, 1972.
- [15] Q. Wang, R. Zhang, L.-L. Yang, and L. Hanzo, “Non-orthogonal multiple access: A unified perspective,” *IEEE Wireless Commun.*, vol. 25, no. 2, pp. 10–16, 2018.
- [16] Y. Chen *et al.*, “Toward the standardization of non-orthogonal multiple access for next generation wireless networks,” *IEEE Commun. Mag.*, vol. 56, no. 3, pp. 19–27, 2018.
- [17] H. Lee, S. Kim, and J.-H. Lim, “Multiuser superposition transmission (MUST) for LTE-A systems,” in *Proc. IEEE Int. Conf. Commun. (ICC), 2016*, 2016, pp. 1–6.

- [18] I. Budhiraja *et al.*, “A systematic review on NOMA variants for 5G and beyond,” *IEEE Access*, vol. 9, pp. 85 573–85 644, 2021.
- [19] M. Vaezi, H. V. Poor, and Z. Ding, *Multiple access techniques for 5G wireless networks and beyond*. Springer, 2019.
- [20] L. Dai *et al.*, “A survey of non-orthogonal multiple access for 5G,” *IEEE Commun. Surveys Tuts.*, vol. 20, no. 3, pp. 2294–2323, 2018.
- [21] S. M. R. Islam *et al.*, “Power-domain non-orthogonal multiple access (NOMA) in 5G systems: Potentials and challenges,” *IEEE Commun. Surveys Tuts.*, vol. 19, no. 2, pp. 721–742, 2017.
- [22] M. Vaezi, R. Schober, Z. Ding, and H. V. Poor, “Non-orthogonal multiple access: Common myths and critical questions,” *IEEE Wireless Communications*, vol. 26, no. 5, pp. 174–180, Oct. 2019.
- [23] M. Saideh, Y. Alsaba, I. Dayoub, and M. Berbineau, “Joint interference cancellation for multi-carrier modulation-based non-orthogonal multiple access,” *IEEE Commun. Lett.*, vol. 23, no. 11, pp. 2114–2117, Nov. 2019.
- [24] C. Yan, A. Harada, A. Benjebbour, Y. Lan, A. Li, and H. Jiang, “Receiver design for downlink non-orthogonal multiple access (NOMA),” in *2015 IEEE 81st Veh. Technol. Conf. (VTC Spring)*, May 2015, pp. 1–6.
- [25] M. S. Ali, H. Tabassum, and E. Hossain, “Dynamic user clustering and power allocation for uplink and downlink non-orthogonal multiple access (NOMA) systems,” *IEEE Access*, vol. 4, pp. 6325–6343, Aug. 2016.
- [26] H. Pan, L. Lu, and S. C. Liew, “Practical power-balanced non-orthogonal multiple access,” *IEEE J. Sel. Areas Commun.*, vol. 35, no. 10, pp. 2312–2327, Oct. 2017.

- [27] Z. Ding, Y. Liu, J. Choi, Q. Sun, M. Elkashlan, C. I, and H. V. Poor, "Application of non-orthogonal multiple access in LTE and 5G networks," *IEEE Commun. Mag.*, vol. 55, no. 2, pp. 185–191, Feb. 2017.
- [28] 3GPP, "Study on Downlink Multiuser Superposition Transmission (MUST) for LTE," 3rd Generation Partnership Project (3GPP), Technical Report (TR) 36.859, 01 2016, version 13.0.0.
- [29] Y. Yuan, Z. Yuan, and L. Tian, "5G non-orthogonal multiple access study in 3GPP," *IEEE Commun. Mag.*, vol. 58, no. 7, pp. 90–96, 2020.
- [30] 3GPP, "Study on Non-Orthogonal Multiple Access (NOMA) for NR," 3rd Generation Partnership Project (3GPP), Technical Report (TR) 38.812, 12 2018, version 13.0.0.
- [31] B. Makki, K. Chitti, A. Behravan, and M. Alouini, "A survey of NOMA: Current status and open research challenges," *IEEE Open J. Commun. Soc.*, vol. 1, pp. 179–189, 2020.
- [32] A. Mishra, Y. Mao, O. Dizdar, and B. Clerckx, "Rate-splitting multiple access for 6G - part i: Principles, applications and future works," *IEEE Commun. Lett.*, pp. 1–1, 2022.
- [33] A. Tusha, S. Doğan, and H. Arslan, "A hybrid downlink NOMA with OFDM and OFDM-IM for beyond 5G wireless networks," *IEEE Signal Process. Lett.*, vol. 27, pp. 491–495, 2020.
- [34] R1-162155: Sparse Code Multiple Access (SCMA) for 5G Radio Transmission, Huawei, HiSilicon, 3GPP TSG RAN WG1 Meeting #84 (2016).
- [35] K. Kusume, G. Bauch, and W. Utschick, "IDMA vs. CDMA: Analysis and comparison of two multiple access schemes," *IEEE Transactions on Wireless Communications*, vol. 11, no. 1, pp. 78–87, 2012.

- [36] S. Chen, B. Ren, Q. Gao, S. Kang, S. Sun, and K. Niu, "Pattern division multiple access—a novel nonorthogonal multiple access for fifth-generation radio networks," *IEEE Transactions on Vehicular Technology*, vol. 66, no. 4, pp. 3185–3196, 2017.
- [37] M. AL-Imari, M. A. Imran, R. Tafazolli, and D. Chen, "Performance evaluation of low density spreading multiple access," in *2012 8th International Wireless Communications and Mobile Computing Conference (IWCMC)*. Limassol, Cyprus, Aug. 27-31, 2012, pp. 383–388.
- [38] R1-166098: Discussion on the feasibility of advanced MU-detector, Huawei, HiSilicon, 3GPP TSG RAN WG1 Meeting #86 (2016).
- [39] A. Yazar and H. Arslan, "A waveform parameter assignment framework for 6g with the role of machine learning," *IEEE Open Journal of Vehicular Technology*, pp. 1–1, 2020.
- [40] A. F. Demir, M. Elkourdi, M. Ibrahim, and H. Arslan, "Waveform design for 5g and beyond," *arXiv preprint arXiv:1902.05999*, 2019.
- [41] A. Sahin, I. Guvenc, and H. Arslan, "A survey on multicarrier communications: Prototype filters, lattice structures, and implementation aspects," *IEEE Commun. Surveys Tuts.*, vol. 16, no. 3, pp. 1312–1338, 3rd Quart., 2014.
- [42] A. Maatouk, E. Çalışkan, M. Koca, M. Assaad, G. Gui, and H. Sari, "Frequency-domain NOMA with two sets of orthogonal signal waveforms," *IEEE Commun. Lett.*, vol. 22, no. 5, pp. 906–909, May 2018.
- [43] M. B. Çelebi and H. Arslan, "Theoretical analysis of the co-existence of LTE-A signals and design of an ML-SIC receiver," *IEEE Trans. Wireless Commun.*, vol. 14, no. 8, pp. 4626–4639, Aug. 2015.

- [44] Z. Ding, R. Schober, P. Fan, and H. Vincent Poor, "OTFS-NOMA: An efficient approach for exploiting heterogenous user mobility profiles," *IEEE Trans. Commun.*, vol. 67, no. 11, pp. 7950–7965, Nov. 2019.
- [45] E. Basar, M. Wen, R. Mesleh, M. Di Renzo, Y. Xiao, and H. Haas, "Index modulation techniques for next-generation wireless networks," *IEEE Access*, vol. 5, pp. 16 693–16 746, 2017.
- [46] X. Wei, H. Liu, Z. Geng, K. Zheng, R. Xu, Y. Liu, and P. Chen, "Software defined radio implementation of a non-orthogonal multiple access system towards 5G," *IEEE Access*, vol. 4, pp. 9604–9613, Dec. 2016.
- [47] W. E. Ryan and S. Lin, *Channel Codes - Classical and Modern*. Cambridge University Press, 2009.
- [48] M. Al-Imari, P. Xiao, M. A. Imran, and R. Tafazolli, "Uplink non-orthogonal multiple access for 5G wireless networks," in *Proc. 11th Int. Symp. on Wireless Commun. Syst.*, Aug. 2014, pp. 781–785.
- [49] E. Başar, Ü. Aygözü, E. Panayırçı, and H. V. Poor, "Orthogonal frequency division multiplexing with index modulation," *IEEE Trans. Signal Process.*, vol. 61, no. 22, pp. 5536–5549, Nov. 2013.
- [50] M. Wen, X. Cheng, M. Ma, B. Jiao, and H. V. Poor, "On the achievable rate of OFDM with index modulation," *IEEE Trans. Signal Process.*, vol. 64, no. 8, pp. 1919–1932, Apr. 2016.
- [51] G. Caire, G. Taricco, and E. Biglieri, "Bit-interleaved coded modulation," *IEEE Trans. Inf. Theory*, vol. 44, no. 3, pp. 927–946, May 1998.

- [52] A. Tusha, S. Doğan, and H. Arslan, “A hybrid downlink NOMA with OFDM and OFDM-IM for beyond 5G wireless networks,” *IEEE Signal Process. Lett.*, vol. 27, pp. 491–495, 2020.
- [53] S. Doğan, A. Tusha, and H. Arslan, “NOMA with index modulation for uplink URLLC through grant-free access,” *IEEE J. Sel. Topics Signal Process.*, vol. 13, no. 6, pp. 1249–1257, Oct. 2019.
- [54] B. C. M. M. Sahin, O. Dizdar and H. Arslan, “Multicarrier rate-splitting multiple access: Superiority of ofdm-rsma over ofdma and ofdm-noma,” *arXiv preprint arXiv:2303.14540*, 2023.
- [55] Z. E. Ankarali, B. Peköz, and H. Arslan, “Flexible radio access beyond 5G: A future projection on waveform, numerology, and frame design principles,” *IEEE Access*, vol. 5, pp. 18 295–18 309, 2017.
- [56] T. Wang, J. Proakis, E. Masry, and J. Zeidler, “Performance degradation of OFDM systems due to Doppler spreading,” *IEEE Trans. Wireless Commun.*, vol. 5, no. 6, pp. 1422–1432, 2006.
- [57] Y. Mao *et al.*, “Rate-splitting multiple access: Fundamentals, survey, and future research trends,” *IEEE Commun. Surveys Tuts.*, pp. 1–1, 2022.
- [58] Y. Mao, B. Clerckx, and V. O. Li, “Rate-splitting multiple access for downlink communication systems: Bridging, generalizing, and outperforming SDMA and NOMA,” *EURASIP J. Wireless Commun. Netw.*, vol. 2018, no. 1, 2018.
- [59] L. Li *et al.*, “Resource allocation for multicarrier rate-splitting multiple access system,” *IEEE Access*, vol. 8, pp. 174 222–174 232, 2020.
- [60] H. Chen *et al.*, “Rate-splitting for multicarrier multigroup multicast: Precoder design and error performance,” *IEEE Trans. Broadcast.*, vol. 67, no. 3, pp. 619–630, 2021.

- [61] O. Dizdar and B. Clerckx, “Rate-splitting multiple access for communications and jamming in multi-antenna multi-carrier cognitive radio systems,” *IEEE Trans. Inf. Forensics Security*, vol. 17, pp. 628–643, 2022.
- [62] F. Hlawatsch and G. Matz, *Wireless Communications Over Rapidly Time-Varying Channels*. Elsevier/Academic Press, 2011.
- [63] H. Joudeh and B. Clerckx, “Sum-rate maximization for linearly precoded downlink multiuser MISO systems with partial CSIT: A rate-splitting approach,” *IEEE Trans. Commun.*, vol. 64, no. 11, pp. 4847–4861, 2016.
- [64] O. Maraqa *et al.*, “A survey of rate-optimal power domain NOMA with enabling technologies of future wireless networks,” *IEEE Commun. Surveys Tuts.*, vol. 22, no. 4, pp. 2192–2235, 2020.
- [65] B. Clerckx, Y. Mao, R. Schober, and H. V. Poor, “Rate-splitting unifying SDMA, OMA, NOMA, and multicasting in MISO broadcast channel: A simple two-user rate analysis,” *IEEE Wireless Commun. Lett.*, vol. 9, no. 3, pp. 349–353, 2020.
- [66] D. Tse and P. Viswanath, *Fundamentals of Wireless Communication*. USA: Cambridge University Press, 2005.
- [67] M. M. Şahin and H. Arslan, “Multi-functional coexistence of radar-sensing and communication waveforms,” in *2020 IEEE 92nd Veh. Technol. Conf. (VTC2020-Fall)*, 2020, pp. 1–5.
- [68] M. M. Şahin, I. E. Gurol, E. Arslan, E. Basar, and H. Arslan, “Ofdm-im for joint communication and radar-sensing: A promising waveform for dual functionality,” *Frontiers in Communications and Networks*, vol. 2, 2021. [Online]. Available: <https://www.frontiersin.org/articles/10.3389/frcmn.2021.715944>

- [69] F. Liu, C. Masouros, A. P. Petropulu, H. Griffiths, and L. Hanzo, "Joint radar and communication design: Applications, state-of-the-art, and the road ahead," *IEEE Trans. Commun.*, pp. 1–1, 2020.
- [70] S. Mazahir, S. Ahmed, and M.-S. Alouini, "A survey on joint communication-radar systems," *Frontiers in Communications and Networks*, vol. 1, p. 9, 2021. [Online]. Available: <https://www.frontiersin.org/article/10.3389/frcmn.2020.619483>
- [71] M. Z. Chowdhury, M. Shahjalal, S. Ahmed, and Y. M. Jang, "6G wireless communication systems: Applications, requirements, technologies, challenges, and research directions," *IEEE Open J. Commun. Soc.*, vol. 1, pp. 957–975, 2020.
- [72] T. X. Han and C. da Silva, "IEEE p802.11 - WLAN sensing (SENS) study group (SG) - meeting update." [Online]. Available: https://www.ieee802.org/11/Reports/senstig_update.htm
- [73] M. L. Rahman *et al.*, "Enabling joint communication and radio sensing in mobile networks - a survey," *arXiv preprint arXiv:2006.07559*, 2020.
- [74] P. Kumari, S. A. Vorobyov, and R. W. Heath, "Adaptive virtual waveform design for millimeter-wave joint communication–radar," *IEEE Trans. Signal Process.*, vol. 68, pp. 715–730, 2020.
- [75] B. Paul, A. R. Chiriyath, and D. W. Bliss, "Survey of RF communications and sensing convergence research," *IEEE Access*, vol. 5, pp. 252–270, 2017.
- [76] N. C. Luong, X. Lu, D. T. Hoang, D. Niyato, and D. Kim, "Radio resource management in joint radar and communication: A comprehensive survey," *IEEE Commun. Surveys Tuts.*, vol. 23, pp. 780–814, 2021.

- [77] L. Zheng, M. Lops, Y. C. Eldar, and X. Wang, “Radar and communication coexistence: An overview: A review of recent methods,” *IEEE Signal Process. Mag.*, vol. 36, no. 5, pp. 85–99, 2019.
- [78] C. D. Ozkaptan, E. Ekici, O. Altintas, and C. Wang, “OFDM pilot-based radar for joint vehicular communication and radar systems,” in *2018 IEEE Vehicular Networking Conference (VNC)*, Dec. 2018, pp. 1–8.
- [79] M. A. Richards, *Fundamentals of radar signal processing*. McGraw Hill Education, 2014.
- [80] Y. Li and G. L. Stüber, *Orthogonal frequency division multiplexing for wireless communications*. Springer, 2011.
- [81] H. Arslan and G. E. Bottomley, “Channel estimation in narrowband wireless communication systems,” *Wireless Commun. and Mobile Comp.*, vol. 1, no. 2, p. 201–219, 2001.
- [82] M. K. Ozdemir and H. Arslan, “Channel estimation for wireless OFDM systems,” *IEEE Commun. Surveys Tuts.*, vol. 9, no. 2, pp. 18–48, 2007.
- [83] 3GPP, “NR; Physical channels and modulation,” 3rd Generation Partnership Project (3GPP), Technical Specification (TS) 38.211, 01 2018, version 15.0.0. [Online]. Available: <http://www.3gpp.org/DynaReport/38211.htm>
- [84] D. H. N. Nguyen and R. W. Heath, “Delay and doppler processing for multi-target detection with iee 802.11 ofdm signaling,” in *2017 IEEE International Conference on Acoustics, Speech and Signal Processing (ICASSP)*, 2017, pp. 3414–3418.
- [85] K. V. Mishra *et al.*, “Toward millimeter-wave joint radar communications: A signal processing perspective,” *IEEE Signal Process. Mag.*, vol. 36, no. 5, pp. 100–114, Sep. 2019.

- [86] Z. Feng *et al.*, “Joint radar and communication: A survey,” *China Commun.*, vol. 17, no. 1, pp. 1–27, Jan. 2020.
- [87] E. Basar, “OFDM with index modulation using coordinate interleaving,” *IEEE Wireless Commun. Lett.*, vol. 4, no. 4, pp. 381–384, Aug. 2015.
- [88] E. Arslan, A. T. Dogukan, and E. Basar, “Index modulation-based flexible non-orthogonal multiple access,” *IEEE Wireless Commun. Lett.*, pp. 1–1, Jul. 2020.
- [89] A. T. Dogukan and E. Basar, “Super-mode ofdm with index modulation,” *IEEE Transactions on Wireless Communications*, Jun. 2020.
- [90] E. Arslan, A. T. Dogukan, and E. Basar, “Sparse-encoded codebook index modulation,” *IEEE Trans. Veh. Technol.*, vol. 69, no. 8, pp. 9126–9130, May. 2020.
- [91] S. S. M. Hoque and A. Şahin, “Index-modulated circularly-shifted chirps for dual-function radar communication systems,” in *2020 IEEE Globecom Workshops (GC Wkshps*, 2020, pp. 1–6.
- [92] T. Huang *et al.*, “MAJoRCom: A dual-function radar communication system using index modulation,” *IEEE Trans. Signal Process.*, vol. 68, pp. 3423–3438, Sep. 2020.
- [93] P. Kumari, J. Choi, N. González-Prelcic, and R. W. Heath, “Ieee 802.11ad-based radar: An approach to joint vehicular communication-radar system,” *IEEE Transactions on Vehicular Technology*, vol. 67, no. 4, pp. 3012–3027, 2018.
- [94] N. Letzepis *et al.*, “Joint estimation of multipath parameters from OFDM signals in mobile channels,” in *2011 Australian Commun. Theo. Workshop*, Feb. 2011, pp. 106–111.
- [95] M. M. Şahin, H. Arslan, and K.-C. Chen, “Control of electromagnetic radiation on coexisting smart radio environment,” *IEEE Open Journal of the Communications Society*, vol. 3, pp. 557–573, 2022.

- [96] G. Liu, X. Hou, Y. Huang, H. Shao, Y. Zheng, F. Wang, and Q. Wang, “Coverage enhancement and fundamental performance of 5G: Analysis and field trial,” *IEEE Communications Magazine*, vol. 57, no. 6, pp. 126–131, 2019.
- [97] M. Giordani, M. Polese, M. Mezzavilla, S. Rangan, and M. Zorzi, “Toward 6G networks: Use cases and technologies,” *IEEE Communications Magazine*, vol. 58, no. 3, pp. 55–61, 2020.
- [98] Y. Chen, P. Zhu, G. He, X. Yan, H. Baligh, and J. Wu, “From connected people, connected things, to connected intelligence,” in *2020 2nd 6G Wireless Summit (6G SUMMIT)*, 2020, pp. 1–7.
- [99] I. F. Akyildiz, A. Kak, and S. Nie, “6G and beyond: The future of wireless communications systems,” *IEEE Access*, vol. 8, pp. 133 995–134 030, 2020.
- [100] K.-C. Chen, S.-C. Lin, J.-H. Hsiao, C.-H. Liu, A. F. Molisch, and G. P. Fettweis, “Wireless networked multirobot systems in smart factories,” *Proc. IEEE*, vol. 109, no. 4, pp. 468–494, 2021.
- [101] H. Arslan, S. D. Tusha, and A. Yazar, “6G vision: An ultra-flexible perspective,” *ITU J. Future Evolving Technol.*, vol. 1, no. 1, p. 121–140, 2020.
- [102] S. J. Nawaz, S. K. Sharma, S. Wyne, M. N. Patwary, and M. Asaduzzaman, “Quantum machine learning for 6G communication networks: State-of-the-art and vision for the future,” *IEEE Access*, vol. 7, pp. 46 317–46 350, 2019.
- [103] Z. Zhang, Y. Xiao, Z. Ma, M. Xiao, Z. Ding, X. Lei, G. K. Karagiannidis, and P. Fan, “6G wireless networks: Vision, requirements, architecture, and key technologies,” *IEEE Veh. Technol. Mag.*, vol. 14, no. 3, pp. 28–41, 2019.
- [104] N. Rajatheva *et al.*, “White paper on broadband connectivity in 6G,” *6G Research Visions*, vol. 10, p. 1, Apr. 2020.

- [105] J. Mitola and G. Maguire, “Cognitive radio: making software radios more personal,” *IEEE Pers. Commun.*, vol. 6, no. 4, pp. 13–18, 1999.
- [106] S.-Y. Lien, K.-C. Chen, Y.-C. Liang, and Y. Lin, “Cognitive radio resource management for future cellular networks,” *IEEE Wireless Commun.*, vol. 21, no. 1, pp. 70–79, 2014.
- [107] Y.-C. Liang, K.-C. Chen, G. Y. Li, and P. Mahonen, “Cognitive radio networking and communications: an overview,” *IEEE Trans. Veh. Technol.*, vol. 60, no. 7, pp. 3386–3407, 2011.
- [108] T. Yucek and H. Arslan, “A survey of spectrum sensing algorithms for cognitive radio applications,” *IEEE Commun. Surveys Tuts.*, vol. 11, no. 1, pp. 116–130, 2009.
- [109] A. Martin, S. Harbison, and K. Beach, *An Introduction to Radiation Protection*. CRC Press, 2019.
- [110] M. D. Renzo, M. Debbah, D.-T. Phan-Huy, A. Zappone, M.-S. Alouini, C. Yuen, V. Sciancalepore, G. C. Alexandropoulos, J. Hoydis, H. Gacanin, J. d. Rosny, A. Bounceu, G. Lerosey, and M. Fink, “Smart radio environments empowered by reconfigurable AI meta-surfaces: An idea whose time has come,” *EURASIP J. Wireless Commun. Netw.*, vol. 129, 2019.
- [111] M. Di Renzo, A. Zappone, M. Debbah, M.-S. Alouini, C. Yuen, J. de Rosny, and S. Tretyakov, “Smart radio environments empowered by reconfigurable intelligent surfaces: How it works, state of research, and the road ahead,” *IEEE J. Sel. Areas Commun.*, vol. 38, no. 11, pp. 2450–2525, 2020.

- [112] A. Welkie, L. Shangguan, J. Gummesson, W. Hu, and K. Jamieson, “Programmable radio environments for smart spaces,” in *Proceedings of the 16th ACM Workshop on Hot Topics in Networks*, ser. HotNets-XVI. New York, NY, USA: Association for Computing Machinery, 2017, p. 36–42. [Online]. Available: <https://doi.org/10.1145/3152434.3152456>
- [113] K.-K. Wong, K.-F. Tong, Z. Chu, and Y. Zhang, “A vision to smart radio environment: Surface wave communication superhighways,” *IEEE Wireless Commun.*, vol. 28, no. 1, pp. 112–119, 2021.
- [114] E. Basar, M. Di Renzo, J. De Rosny, M. Debbah, M. S. Alouini, and R. Zhang, “Wireless communications through reconfigurable intelligent surfaces,” *IEEE Access*, vol. 7, pp. 116 753–116 773, 2019.
- [115] Q. Wu and R. Zhang, “Towards smart and reconfigurable environment: Intelligent reflecting surface aided wireless network,” *IEEE Commun. Mag.*, vol. 58, no. 1, pp. 106–112, 2020.
- [116] N. Van Huynh, D. T. Hoang, X. Lu, D. Niyato, P. Wang, and D. I. Kim, “Ambient backscatter communications: A contemporary survey,” *IEEE Commun. Surveys Tuts.*, vol. 20, no. 4, pp. 2889–2922, 2018.
- [117] Y. Niu, Y. Li, D. Jin, L. Su, and A. V. Vasilakos, “A survey of millimeter wave communications (mmWave) for 5G: opportunities and challenges,” *Wireless Netw.*, vol. 21, no. 8, p. 2657–2676, 2015.
- [118] D. Lockie and D. Peck, “High-data-rate millimeter-wave radios,” *IEEE Microw. Mag.*, vol. 10, no. 5, pp. 75–83, 2009.
- [119] B. Mondal, T. A. Thomas, E. Visotsky, F. W. Vook, A. Ghosh, Y. h. Nam, Y. Li, J. Zhang, M. Zhang, Q. Luo, Y. Kakishima, and K. Kitao, “3D channel model in 3GPP,” *IEEE Commun. Mag.*, vol. 53, no. 3, pp. 16–23, 2015.

- [120] I. A. Hemadeh, K. Satyanarayana, M. El-Hajjar, and L. Hanzo, “Millimeter-wave communications: Physical channel models, design considerations, antenna constructions, and link-budget,” *IEEE Commun. Surveys Tuts.*, vol. 20, no. 2, pp. 870–913, 2018.
- [121] M. Alayasra and H. Arslan, “IRS-enabled beam-space channel,” *IEEE Transactions on Wireless Communications*, pp. 1–1, 2021.
- [122] O. Ozdogan, E. Bjornson, and E. G. Larsson, “Intelligent reflecting surfaces: Physics, propagation, and pathloss modeling,” *IEEE Wireless Commun. Lett.*, vol. 9, no. 5, pp. 581–585, 2020.
- [123] E. Björnson, O. Ozdogan, and E. G. Larsson, “Intelligent reflecting surface versus decode-and-forward: How large surfaces are needed to beat relaying?” *IEEE Wireless Communications Letters*, vol. 9, no. 2, pp. 244–248, 2020.
- [124] A. Taha, M. Alrabeiah, and A. Alkhateeb, “Enabling large intelligent surfaces with compressive sensing and deep learning,” *IEEE Access*, vol. 9, pp. 44 304–44 321, 2021.
- [125] Q.-U.-A. Nadeem, H. Alwazani, A. Kammoun, A. Chaaban, M. Debbah, and M.-S. Alouini, “Intelligent reflecting surface-assisted multi-user miso communication: Channel estimation and beamforming design,” *IEEE Open J. Commun. Soc.*, vol. 1, pp. 661–680, 2020.
- [126] B. Zheng and R. Zhang, “Intelligent reflecting surface-enhanced OFDM: Channel estimation and reflection optimization,” *IEEE Wireless Commun. Lett.*, vol. 9, no. 4, pp. 518–522, 2020.
- [127] A. Goldsmith, *Wireless Communications*. USA: Cambridge University Press, 2005.
- [128] E. Basar and I. Yildirim, “Reconfigurable intelligent surfaces for future wireless networks: A channel modeling perspective,” *IEEE Wireless Commun.*, pp. 1–7, 2021.

- [129] K. Haneda *et al.*, “5G 3GPP-like channel models for outdoor urban microcellular and macrocellular environments,” in *Proc. IEEE 83rd Veh. Technol. Conf. (VTC Spring)*, May 2016, pp. 1–7.
- [130] H. Guo, Y.-C. Liang, J. Chen, and E. G. Larsson, “Weighted sum-rate maximization for reconfigurable intelligent surface aided wireless networks,” *IEEE Transactions on Wireless Communications*, vol. 19, no. 5, pp. 3064–3076, 2020.
- [131] C. Pan, H. Ren, K. Wang, W. Xu, M. ElKashlan, A. Nallanathan, and L. Hanzo, “Multicell MIMO communications relying on intelligent reflecting surfaces,” *IEEE Trans. Wireless Commun.*, vol. 19, no. 8, pp. 5218–5233, 2020.
- [132] C. A. Balanis, *Antenna Theory: Analysis and Design*. Wiley-Interscience, 2016.
- [133] S. Ju, O. Kanhere, Y. Xing, and T. S. Rappaport, “A millimeter-wave channel simulator NYUSIM with spatial consistency and human blockage,” in *2019 IEEE Global Communications Conference (GLOBECOM)*, 2019, pp. 1–6.
- [134] S. Li, B. Duo, X. Yuan, Y.-C. Liang, and M. Di Renzo, “Reconfigurable intelligent surface assisted UAV communication: Joint trajectory design and passive beamforming,” *IEEE Wireless Commun. Lett.*, vol. 9, no. 5, pp. 716–720, 2020.
- [135] Q. Zhang, Y.-C. Liang, and H. V. Poor, “Reconfigurable intelligent surface assisted MIMO symbiotic radio networks,” *IEEE Transactions on Communications*, vol. 69, no. 7, pp. 4832–4846, 2021.
- [136] Y. Cao, T. Lv, and W. Ni, “Intelligent reflecting surface aided multi-user mmWave communications for coverage enhancement,” in *2020 IEEE 31st Annual International Symposium on Personal, Indoor and Mobile Radio Communications*, 2020, pp. 1–6.

- [137] R. Alghamdi, R. Alhadrami, D. Alhothali, H. Almorad, A. Faisal, S. Helal, R. Shalabi, R. Asfour, N. Hammad, A. Shams, N. Saeed, H. Dahrouj, T. Y. Al-Naffouri, and M.-S. Alouini, “Intelligent surfaces for 6G wireless networks: A survey of optimization and performance analysis techniques,” *IEEE Access*, vol. 8, pp. 202 795–202 818, 2020.
- [138] C. Huang, A. Zappone, G. C. Alexandropoulos, M. Debbah, and C. Yuen, “Reconfigurable intelligent surfaces for energy efficiency in wireless communication,” *IEEE Transactions on Wireless Communications*, vol. 18, no. 8, pp. 4157–4170, 2019.
- [139] Q. Zhang, W. Saad, and M. Bennis, “Reflections in the sky: Millimeter wave communication with UAV-carried intelligent reflectors,” in *2019 IEEE Global Communications Conference (GLOBECOM)*, 2019, pp. 1–6.
- [140] H. Chiang, K. Chen, W. Rave, M. K. Marandi, and G. Fettweis, “Multi-UAV mmWave beam tracking using Q-Learning and interference mitigation,” in *2020 IEEE International Conference on Communications Workshops (ICC Workshops)*, 2020, pp. 1–7.
- [141] S. Alfattani, W. Jaafar, Y. Hmamouche, H. Yanikomeroğlu, A. Yongaçoğlu, N. D. Dào, and P. Zhu, “Aerial platforms with reconfigurable smart surfaces for 5G and beyond,” *IEEE Communications Magazine*, vol. 59, no. 1, pp. 96–102, 2021.
- [142] L. Ge, P. Dong, H. Zhang, J. Wang, and X. You, “Joint beamforming and trajectory optimization for intelligent reflecting surfaces-assisted UAV communications,” *IEEE Access*, vol. 8, pp. 78 702–78 712, 2020.
- [143] K. W. Cho, M. H. Mazaheri, J. Gummesson, O. Abari, and K. Jamieson, “Mmwall: A reconfigurable metamaterial surface for MmWave networks,” in *Proceedings of the 22nd International Workshop on Mobile Computing Systems and Applications*, ser. HotMobile ’21. New York, NY, USA: Association for Computing Machinery, 2021, p. 119–125. [Online]. Available: <https://doi.org/10.1145/3446382.3448665>

- [144] M. H. Yılmaz, E. Güvenkaya, G. Mumcu, and H. Arslan, “Millimeter-wave wireless channel control using spatially adaptive antenna arrays,” *IEEE Communications Letters*, vol. 21, no. 3, pp. 680–683, 2017.
- [145] J. Mendoza, M. Karabacak, H. Arslan, and G. Mumcu, “A spatially adaptive antenna array for Mm-Wave wireless channel control with microfluidics based reconfiguration,” *IEEE Access*, vol. 8, pp. 182 898–182 907, 2020.
- [146] E. Basar, I. Yildirim, and F. Kilinc, “Indoor and outdoor physical channel modeling and efficient positioning for reconfigurable intelligent surfaces in mmWave bands,” *IEEE Transactions on Communications*, pp. 1–1, 2021.
- [147] J. Li, “LOS probability modeling for 5G indoor scenario,” in *2016 International Symposium on Antennas and Propagation (ISAP)*, 2016, pp. 204–205.
- [148] A. Bereketli and O. B. Akan, “Communication coverage in wireless passive sensor networks,” *IEEE Communications Letters*, vol. 13, no. 2, pp. 133–135, 2009.
- [149] V. Liu, A. Parks, V. Talla, S. Gollakota, D. Wetherall, and J. R. Smith, “Ambient backscatter: Wireless communication out of thin air,” *SIGCOMM Comput. Commun. Rev.*, vol. 43, no. 4, p. 39–50, Aug. 2013. [Online]. Available: <https://doi.org/10.1145/2534169.2486015>
- [150] N. Van Huynh, D. T. Hoang, X. Lu, D. Niyato, P. Wang, and D. I. Kim, “Ambient backscatter communications: A contemporary survey,” *IEEE Communications Surveys & Tutorials*, vol. 20, no. 4, pp. 2889–2922, 2018.
- [151] W. Liu, Y. Liang, Y. Li, and B. Vucetic, “Backscatter multiplicative multiple-access systems: Fundamental limits and practical design,” *IEEE Transactions on Wireless Communications*, vol. 17, no. 9, pp. 5713–5728, 2018.

- [152] H. Guo, Y. Liang, R. Long, and Q. Zhang, “Cooperative ambient backscatter system: A symbiotic radio paradigm for passive IoT,” *IEEE Wireless Communications Letters*, vol. 8, no. 4, pp. 1191–1194, 2019.
- [153] H. Guo, R. Long, and Y. C. Liang, “Cognitive backscatter network: A spectrum sharing paradigm for passive IoT,” *IEEE Wireless Communications Letters*, vol. 8, no. 5, pp. 1423–1426, 2019.
- [154] M. A. ElMossallamy, M. Pan, R. Jäntti, K. G. Seddik, G. Y. Li, and Z. Han, “Noncoherent backscatter communications over ambient OFDM signals,” *IEEE Transactions on Communications*, vol. 67, no. 5, pp. 3597–3611, 2019.
- [155] Y.-C. Liang, Q. Zhang, E. G. Larsson, and G. Y. Li, “Symbiotic radio: Cognitive backscattering communications for future wireless networks,” *IEEE Trans. Cogn. Commun. Netw.*, vol. 6, no. 4, pp. 1242–1255, 2020.
- [156] S. S. Rao, *Introduction to Optimization*. John Wiley & Sons, Ltd, 2019. [Online]. Available: <https://onlinelibrary.wiley.com/doi/abs/10.1002/9781119454816.ch1>
- [157] Y. Chen, “Performance of ambient backscatter systems using reconfigurable intelligent surface,” *IEEE Communications Letters*, vol. 25, no. 8, pp. 2536–2539, 2021.
- [158] A. Bhowal, S. Aïssa, and R. S. Kshetrimayum, “RIS-assisted advanced spatial modulation techniques for ambient backscattering communications,” *IEEE Trans. Green Commun. Netw.*, vol. 5, no. 4, pp. 1684–1696.
- [159] R. Fara, D.-T. Phan-Huy, P. Ratajczak, A. Ourir, M. Di Renzo, and J. De Rosny, “Reconfigurable Intelligent Surface-Assisted Ambient Backscatter Communications – Experimental Assessment,” in *2021 IEEE International Conference on Communications Workshops (ICC Workshops)*, 2021, pp. 1–7.

- [160] J. Hu, Y.-C. Liang, and Y. Pei, "Reconfigurable intelligent surface enhanced multi-user MISO symbiotic radio system," *IEEE Trans. Commun.*, vol. 69, no. 4, pp. 2359–2371, 2021.
- [161] P. Cheng, Z. Chen, M. Ding, Y. Li, B. Vucetic, and D. Niyato, "Spectrum intelligent radio: Technology, development, and future trends," *IEEE Commun. Mag.*, vol. 58, no. 1, pp. 12–18, 2020.
- [162] T.-W. Chiang and K.-C. Chen, "Synthetic aperture radar construction of spectrum map for cognitive radio networking," in *Proceedings of the 6th International Wireless Communications and Mobile Computing Conference*, ser. IWCMC '10. New York, NY, USA: Association for Computing Machinery, 2010, p. 631–635. [Online]. Available: <https://doi.org/10.1145/1815396.1815542>
- [163] S.-Y. Shih and K.-C. Chen, "Compressed sensing construction of spectrum map for routing in cognitive radio networks," in *2011 IEEE 73rd Vehicular Technology Conference (VTC Spring)*, 2011, pp. 1–5.
- [164] S.-y. Lien, K.-c. Chen, Y.-c. Liang, and Y. Lin, "Cognitive radio resource management for future cellular networks," *IEEE Wireless Communications*, vol. 21, no. 1, pp. 70–79, 2014.
- [165] C.-K. Yu, K.-C. Chen, and S.-M. Cheng, "Cognitive radio network tomography," *IEEE Trans. Veh. Technol.*, vol. 59, no. 4, pp. 1980–1997, 2010.
- [166] C.-K. Yu and K.-C. Chen, "Spectrum map retrieval using cognitive radio network tomography," in *2011 IEEE GLOBECOM Workshops (GC Wkshps)*, 2011, pp. 986–991.
- [167] S.-Y. Lien, S.-Y. Shih, and K.-C. Chen, "Spectrum map empowered resource management for qos guarantees in multi-tier cellular networks," in *2011 IEEE Global Telecommunications Conference - GLOBECOM 2011*, 2011, pp. 1–6.

- [168] S.-C. Lin and K.-C. Chen, "Spectrum-map-empowered opportunistic routing for cognitive radio ad hoc networks," *IEEE Trans. Veh. Technol.*, vol. 63, no. 6, pp. 2848–2861, 2014.
- [169] W. Lee, M. Kim, and D.-H. Cho, "Deep cooperative sensing: Cooperative spectrum sensing based on convolutional neural networks," *IEEE Trans. Veh. Technol.*, vol. 68, no. 3, pp. 3005–3009, 2019.
- [170] B. M. Pati, M. Kaneko, and A. Taparugssanagorn, "A deep convolutional neural network based transfer learning method for non-cooperative spectrum sensing," *IEEE Access*, vol. 8, pp. 164 529–164 545, 2020.
- [171] Y. Xu, P. Cheng, Z. Chen, Y. Li, and B. Vucetic, "Mobile collaborative spectrum sensing for heterogeneous networks: A bayesian machine learning approach," *IEEE Trans. Signal Process.*, vol. 66, no. 21, pp. 5634–5647, 2018.
- [172] O. P. Awe, A. Deligiannis, and S. Lambotharan, "Spatio-temporal spectrum sensing in cognitive radio networks using beamformer-aided SVM algorithms," *IEEE Access*, vol. 6, pp. 25 377–25 388, 2018.
- [173] Z. Qin and G. Y. Li, "Pathway to intelligent radio," *IEEE Wireless Commun.*, vol. 27, no. 1, pp. 9–15, 2020.
- [174] X.-L. Huang, Y. Gao, X.-W. Tang, and S.-B. Wang, "Spectrum mapping in large-scale cognitive radio networks with historical spectrum decision results learning," *IEEE Access*, vol. 6, pp. 21 350–21 358, 2018.
- [175] H. Joshi, S. Santra, S. J. Darak, M. K. Hanawal, and S. V. S. Santosh, "Multiplay multiarmed bandit algorithm based sensing of noncontiguous wideband spectrum for AIoT networks," *IEEE Trans. Ind. Informat.*, vol. 18, no. 5, pp. 3337–3348, 2022.

- [176] L. Li and A. Ghasemi, "IoT-enabled machine learning for an algorithmic spectrum decision process," *IEEE Internet Things J.*, vol. 6, no. 2, pp. 1911–1919, 2019.
- [177] F. Hussain, S. A. Hassan, R. Hussain, and E. Hossain, "Machine learning for resource management in cellular and IoT networks: Potentials, current solutions, and open challenges," *IEEE Communications Surveys & Tutorials*, vol. 22, no. 2, pp. 1251–1275, 2020.
- [178] K. M. Thilina, K. W. Choi, N. Saquib, and E. Hossain, "Machine learning techniques for cooperative spectrum sensing in cognitive radio networks," *IEEE J. Sel. Areas Commun.*, vol. 31, no. 11, pp. 2209–2221, 2013.
- [179] C. Jiang, H. Zhang, Y. Ren, Z. Han, K.-C. Chen, and L. Hanzo, "Machine learning paradigms for next-generation wireless networks," *IEEE Wireless Communications*, vol. 24, no. 2, pp. 98–105, 2017.
- [180] J. Wang, C. Jiang, H. Zhang, Y. Ren, K.-C. Chen, and L. Hanzo, "Thirty years of machine learning: The road to pareto-optimal wireless networks," *IEEE Commun. Surveys Tuts.*, vol. 22, pp. 1472–1514, 2020.
- [181] Y. Qi, Y. Wang, and C. Lai, "An improved SVM-based spatial spectrum sensing scheme via beamspace at low SNRs," *IEEE Access*, vol. 7, pp. 184 759–184 768, 2019.
- [182] Q. Wang, H. Sun, R. Q. Hu, and A. Bhuyan, "When machine learning meets spectrum sharing security: Methodologies and challenges," *IEEE Open J. Commun. Soc.*, vol. 3, pp. 176–208, 2022.
- [183] G. Ding, Q. Wu, Y.-D. Yao, J. Wang, and Y. Chen, "Kernel-based learning for statistical signal processing in cognitive radio networks: Theoretical foundations, example applications, and future directions," *IEEE Signal Process. Mag.*, vol. 30, no. 4, pp. 126–136, 2013.

- [184] E. Basar and H. V. Poor, “Present and future of reconfigurable intelligent surface-empowered communications [perspectives],” *IEEE Signal Process. Mag.*, vol. 38, no. 6, pp. 146–152, 2021.
- [185] Q. Yang, Y. Liu, T. Chen, and Y. Tong, “Federated machine learning: Concept and applications,” *ACM Trans. Intell. Syst. Technol.*, vol. 10, no. 2, 2019.

Appendix A: Copyright Permissions

The permission below is for the reproduction of material in Chapter 2.



Waveform-Domain NOMA: The Future of Multiple Access
Conference Proceedings: 2020 IEEE International Conference on Communications Workshops (ICC Workshops)
Author: Mehmet Mert Şahin
Publisher: IEEE
Date: June 2020
Copyright © 2020, IEEE

Thesis / Dissertation Reuse

The IEEE does not require individuals working on a thesis to obtain a formal reuse license, however, you may print out this statement to be used as a permission grant:

Requirements to be followed when using any portion (e.g., figure, graph, table, or textual material) of an IEEE copyrighted paper in a thesis:

- 1) In the case of textual material (e.g., using short quotes or referring to the work within these papers) users must give full credit to the original source (author, paper, publication) followed by the IEEE copyright line © 2011 IEEE.
- 2) In the case of illustrations or tabular material, we require that the copyright line © [Year of original publication] IEEE appear prominently with each reprinted figure and/or table.
- 3) If a substantial portion of the original paper is to be used, and if you are not the senior author, also obtain the senior author's approval.

Requirements to be followed when using an entire IEEE copyrighted paper in a thesis:

- 1) The following IEEE copyright/ credit notice should be placed prominently in the references: © [year of original publication] IEEE. Reprinted, with permission, from [author names, paper title, IEEE publication title, and month/year of publication]
- 2) Only the accepted version of an IEEE copyrighted paper can be used when posting the paper or your thesis on-line.
- 3) In placing the thesis on the author's university website, please display the following message in a prominent place on the website: In reference to IEEE copyrighted material which is used with permission in this thesis, the IEEE does not endorse any of [university/educational entity's name goes here]'s products or services. Internal or personal use of this material is permitted. If interested in reprinting/republishing IEEE copyrighted material for advertising or promotional purposes or for creating new collective works for resale or redistribution, please go to http://www.ieee.org/publications_standards/publications/rights/rights_link.html to learn how to obtain a License from RightsLink.

If applicable, University Microfilms and/or ProQuest Library, or the Archives of Canada may supply single copies of the dissertation.

BACK CLOSE WINDOW

The permission below is for the reproduction of material in Chapter 2.

JOHN WILEY AND SONS ORDER DETAILS

Mar 27, 2023

This Agreement between Mehmet Mert Sahin ("You") and John Wiley and Sons ("John Wiley and Sons") consists of your order details and the terms and conditions provided by John Wiley and Sons and Copyright Clearance Center.

Order Number	501803365
Order date	Mar 27, 2023
Licensed Content Publisher	John Wiley and Sons
Licensed Content Publication	Wiley Books
Licensed Content Title	Wireless Communication Signals: A Laboratory-based Approach
Licensed Content Author	Huseyin Arslan
Licensed Content Date	May 1, 2021
Licensed Content Pages	1
Type of use	Dissertation/Thesis
Requestor type	University/Academic
Format	Electronic
Portion	Figure/table
Number of figures/tables	5
Will you be translating?	No
Title	PhD Dissertation Defense
Institution name	University of South Florida
Expected presentation date	Mar 2023
Portions	Figure 9.22 and Figure 9.24 Mr. Mehmet Mert Sahin 4202 E Fowler Ave

Requestor Location	Tampa, FL 33620-9951 United States Attn: Mr. Mehmet Mert Sahin
Publisher Tax ID	EU826007151
Billing Type	Invoice Mr. Mehmet Mert Sahin 4202 E Fowler Ave

Billing Address	Tampa, FL 33620-9951 United States Attn: Mehmet Mert Sahin
-----------------	--

Total	0.00 USD
-------	----------

Terms and Conditions

TERMS AND CONDITIONS

This copyrighted material is owned by or exclusively licensed to John Wiley & Sons, Inc. or one of its group companies (each a "Wiley Company") or handled on behalf of a society with which a Wiley Company has exclusive publishing rights in relation to a particular work (collectively "WILEY"). By clicking "accept" in connection with completing this licensing transaction, you agree that the following terms and conditions apply to this transaction (along with the billing and payment terms and conditions established by the Copyright Clearance Center Inc., ("CCC's Billing and Payment terms and conditions"), at the time that you opened your RightsLink account (these are available at any time at <http://myaccount.copyright.com>).

The permission below is for the reproduction of material in Chapter 2 and 4.

Creative Commons Attribution License (CCBY)

Application-Based Coexistence of Different Waveforms on Non-Orthogonal Multiple Access

Sahin, Mehmet Mert ; Arslan, Huseyin

IEEE Open Journal of the Communications Society

By clicking the checkbox at the bottom of this page you, as the author or representative of the author, confirm that your work is licensed to IEEE under the Creative Commons Attribution 4.0(CCBY 4.0). As explained by the Creative Commons web site, this license states that IEEE is free to share, copy, distribute and transmit your work under the following conditions:

- **Attribution** - Users must attribute the work in the manner specified by the author or licensor (but not in any way that suggests that they endorse the users or their use of the work).

With the understanding that:

- **Waiver** - Any of the above conditions can be waived if users get permission from the copyright holder.
- **Public Domain** - Where the work or any of its elements is in the public domain under applicable law, that status is in no way affected by the license.
- **Other Rights** - In no way are any of the following rights affected by the license:
 - A user's fair dealing or fair use rights, or other applicable copyright exceptions and limitations;
 - The author's moral rights;
 - Rights other persons may have either in the work itself or in how the work is used, such as publicity or privacy rights.

For any reuse or distribution, users must make clear to others the license terms of this work.

Upon clicking on the checkbox below, you will not only confirm that your submission is under the CCBY license but you will also be taken to IEEE's Terms of Use, which will require your signature.

I confirm the submitted work is licensed to IEEE under the Creative Commons Attribution 4.0 United States (CCBY 4.0)

TERMS AND CONDITIONS OF AN AUTHOR'S USE OF THE CREATIVE COMMONS ATTRIBUTION LICENSE (CCBY)

1. Creative Commons Licensing

To grow the commons of free knowledge and free culture, all users are required to grant broad permissions to the general public to re-distribute and re-use their contributions freely. Therefore, for any text, figures, or other work in any medium you hold the copyright to, by submitting it, you agree to license it under the Creative Commons Attribution 4.0 Unported License.

2. Attribution

As an author, you agree to be attributed in any of the following fashions: a) through a hyperlink (where possible) or URL to the article or articles you contributed to, b) through a hyperlink (where possible) or URL to an alternative, stable online copy which is freely accessible, which conforms with the license, and which provides credit to the authors in a manner equivalent to the credit given on this website, or c) through a list of all authors.

The permission below is for the reproduction of material in Chapter 3.

arXiv Permissions and Reuse

Home

About >

Help >

Submit an Article >

Find and Read Articles >

Search for articles

Viewing submissions

Email subscriptions for new papers

arXiv Identifier

Configuring your browser

RSS Feeds

Licenses

Permissions and Reuse

What is MathJax?

Accounts >

Bulk Access to Metadata and Full Text >

Brand >

Labs >

Policies >

Categories

arXiv Usage Stats

All arXiv abstract pages indicate an [assigned license](#) underneath the "Download:" options.

The link may appear as just the text (license) , such as at [arXiv:2201.14176](#). Articles between 1991 and 2003 have an [assumed license](#). These are functionally equivalent to the arXiv non-exclusive license.

If the license applied by the submitter is one of the Creative Commons licenses, then a "CC" logo will appear, such as at [arXiv:2201.04182](#).

I want to include a paper of mine from arXiv in my thesis, do I need specific permission?

If you are the copyright holder of the work, you do not need arXiv's permission to reuse the full text.

I want to include a paper of mine from arXiv in an institutional repository, do I need permission?

You do not need arXiv's permission to deposit arXiv's version of *your* work into an institutional repository. For all other institutional repository cases, [see our help page on institutional repositories](#).

Can I harvest the full text of works?

Please see our [bulk data](#) help page, and the [API Terms of Use](#) for specific options. Note that the license for the full text is not a part of the current search API schema. The license is, however, provided within arXiv's output from the [OAI-PMH](#) in either `arXiv` or `arXivRaw` formats.

Table of contents

Reuse Requests

Can I reuse figures from an arXiv paper?

Do I need arXiv's permission to repost the full text?

[How can I determine what license the version was assigned?](#)

I want to include a paper of mine from arXiv in my thesis, do I need specific permission?

I want to include a paper of mine from arXiv in an institutional repository, do I need permission?

Can I harvest the full text of works?

The permission below is for the reproduction of material in Chapter 4.



Multi-functional Coexistence of Radar-Sensing and Communication Waveforms
Conference Proceedings: 2020 IEEE 92nd Vehicular Technology Conference (VTC2020-Fall)
Author: Mehmet Mert Şahin
Publisher: IEEE
Date: November 2020
Copyright © 2020, IEEE

Thesis / Dissertation Reuse

The IEEE does not require individuals working on a thesis to obtain a formal reuse license, however, you may print out this statement to be used as a permission grant:

Requirements to be followed when using any portion (e.g., figure, graph, table, or textual material) of an IEEE copyrighted paper in a thesis:

- 1) In the case of textual material (e.g., using short quotes or referring to the work within these papers) users must give full credit to the original source (author, paper, publication) followed by the IEEE copyright line © 2011 IEEE.
- 2) In the case of illustrations or tabular material, we require that the copyright line © [Year of original publication] IEEE appear prominently with each reprinted figure and/or table.
- 3) If a substantial portion of the original paper is to be used, and if you are not the senior author, also obtain the senior author's approval.

Requirements to be followed when using an entire IEEE copyrighted paper in a thesis:

- 1) The following IEEE copyright/ credit notice should be placed prominently in the references: © [year of original publication] IEEE. Reprinted, with permission, from [author names, paper title, IEEE publication title, and month/year of publication]
- 2) Only the accepted version of an IEEE copyrighted paper can be used when posting the paper or your thesis on-line.
- 3) In placing the thesis on the author's university website, please display the following message in a prominent place on the website: In reference to IEEE copyrighted material which is used with permission in this thesis, the IEEE does not endorse any of [university/educational entity's name goes here]'s products or services. Internal or personal use of this material is permitted. If interested in reprinting/republishing IEEE copyrighted material for advertising or promotional purposes or for creating new collective works for resale or redistribution, please go to http://www.ieee.org/publications_standards/publications/rights/rights_link.html to learn how to obtain a License from RightsLink.

If applicable, University Microfilms and/or ProQuest Library, or the Archives of Canada may supply single copies of the dissertation.

BACK CLOSE WINDOW

© 2023 Copyright - All Rights Reserved | Copyright Clearance Center, Inc. | Privacy statement | Data Security and Privacy | For California Residents | Terms and Conditions Comments? We would like to hear from you. E-mail us at customer-care@copyright.com

The permission below is for the reproduction of material in Chapter 4.

frontiers About All Journals All articles (Submit your research) Search Login

Frontiers checks all submitted manuscripts for plagiarism and duplication, and publishes only original content. Those manuscripts where plagiarism or duplication is shown to have occurred will not be considered for publication in a Frontiers journal. It is required that all submissions consist of content that has not been published previously. In accordance with [COPE guidelines](#), we expect that "original wording taken directly from publications by other researchers should appear in quotation marks with the appropriate citations." This condition also applies to an author's own work.

Theses and dissertations

Frontiers allows the inclusion of content which first appeared in an author's thesis so long as this is the only form in which it has appeared, is in line with the author's university policy, and can be accessed online. If the thesis is not archived online, it is considered original, unpublished data and is subject to the unpublished data restrictions of some article types. Inclusion of material from theses or dissertations should be noted in the Acknowledgements section of the manuscript and cited accordingly in the reference list. For some examples, please check the 'References' section of our [author guidelines](#).

Conferences, proceedings, and abstracts

Manuscripts that first appeared as conference papers must be expanded upon if they are to be considered as original work. Authors are required to add a substantial amount of original content in the form of new raw material (experiments, data) or new treatment of old data sets which lead to original discussion and/or conclusions, providing value that significantly exceeds the original conference version. As a rule of thumb, at least 30% of the content must be original. Authors submitting such work are required to:

- seek permission for reuse of the published conference paper if the author does not hold the copyright
- cite the conference in the acknowledgements section, or the references section if applicable.

Blogs

Although permissible, extended manuscript content which previously appeared online in non-academic media, such as blogs, should be declared at the time of submission in the acknowledgements section of the manuscript.

Policies and Publication Ethics

- Frontiers' policies
- Editorial policies

The permission below is for the reproduction of material in Chapter 5.

Creative Commons Attribution License (CCBY)

Control of Electromagnetic Radiation on Coexisting Smart Radio Environment

Sahin, Mehmet Mert ; Arslan, Huseyin; Chen, Kwang-Cheng

IEEE Open Journal of the Communications Society

By clicking the checkbox at the bottom of this page you, as the author or representative of the author, confirm that your work is licensed to IEEE under the Creative Commons Attribution 4.0(CCBY 4.0). As explained by the Creative Commons web site, this license states that IEEE is free to share, copy, distribute and transmit your work under the following conditions:

- Attribution - Users must attribute the work in the manner specified by the author or licensor (but not in any way that suggests that they endorse the users or their use of the work).

With the understanding that:

- **Waiver** - Any of the above conditions can be waived if users get permission from the copyright holder.
- **Public Domain** - Where the work or any of its elements is in the public domain under applicable law, that status is in no way affected by the license.
- **Other Rights** - In no way are any of the following rights affected by the license:
 - A user's fair dealing or fair use rights, or other applicable copyright exceptions and limitations;
 - The author's moral rights;
 - Rights other persons may have either in the work itself or in how the work is used, such as publicity or privacy rights.

For any reuse or distribution, users must make clear to others the license terms of this work.

Upon clicking on the checkbox below, you will not only confirm that your submission is under the CCBY license but you will also be taken to IEEE's Terms of Use, which will require your signature.

I confirm the submitted work is licensed to IEEE under the Creative Commons Attribution 4.0 United States (CCBY 4.0)

TERMS AND CONDITIONS OF AN AUTHOR'S USE OF THE CREATIVE COMMONS ATTRIBUTION LICENSE (CCBY)

1. Creative Commons Licensing

To grow the commons of free knowledge and free culture, all users are required to grant broad permissions to the general public to re-distribute and re-use their contributions freely. Therefore, for any text, figures, or other work in any medium you hold the copyright to, by submitting it, you agree to license it under the Creative Commons Attribution 4.0 Unported License.

2. Attribution

As an author, you agree to be attributed in any of the following fashions: a) through a hyperlink (where possible) or URL to the article or articles you contributed to, b) through a hyperlink (where possible) or URL to an alternative, stable online copy which is freely accessible, which conforms with the license, and which provides credit to the authors in a manner equivalent to the credit given on this website, or c) through a list of all authors.

About the Author

Mehmet Mert Şahin received the B.S. degree from Bilkent University, Ankara, Turkey, in 2019. He worked at ASELSAN Inc. as a wireless communication design engineer in 2019. For internship studies in 2022, he was with Mavenir Inc. He is currently working toward the Ph.D. degree at University of South Florida, Tampa, FL, USA. His research interest include waveform design for future wireless networks, multiple accessing, interference management, joint radar-sensing and communication.